

Exploring nonlinearities in multimode optical fibers for lasers and computing

Présentée le 17 août 2021

Faculté des sciences et techniques de l'ingénieur
Laboratoire de dispositifs photoniques appliqués
Programme doctoral en photonique

pour l'obtention du grade de Docteur ès Sciences

par

Ugur TEGIN

Acceptée sur proposition du jury

Prof. O. Martin, président du jury
Prof. C. Moser, Prof. D. Psaltis, directeurs de thèse
Prof. G. Barbastathis, rapporteur
Prof. D. Brunner, rapporteur
Prof. L. Thévenaz, rapporteur

Acknowledgements

I would like to thank my supervisors Prof. Christophe Moser and Prof. Demetri Psaltis for their support and guidance during my studies. Thanks to their encouragement and trust, with the provided liberty, I could find a chance to conduct my research in a broad field from laser to machine learning with utmost freedom.

I would like to thank my parents Abdullah and Keziban for their continuous support and care. Since my childhood, their encouragements lead me to research and explore. I would like to thank my brothers Umut and Abitter for their support. I would also like to thank my lovely wife, Ayşen Nur for her love, support and patience during this adventure. Without her support, all of this would not have been possible.

I would like to thank my former office mates, Damien Loterie and Paul Deltort for the great time we shared and their priceless advice. I would like to thank Dr. Navid Borhani, Niyazi Ulaş Dinç, Mustafa Yıldırım, İlker Oğuz and Leo Jih-Liang Hsieh for their friendship, enthusiasm and the fruitful discussions we had. I would like to thank to the recent and former members of the Laboratory of Applied Photonics Devices and Laboratory of Optics, whom I had the chance to work with, for their patience, assistance, and company. Lastly, I want to thank to Sabrina Martone and Silke Jan for their administrative support and guidance.

Lausanne, April 3rd 2021

Uğur

Abstract

Multimode optical fibers are the backbone of telecommunication and medical imaging. When light with high intensity travels through a multimode fiber, photons and matter start to interact and propagation becomes nonlinear. The nonlinear propagation of light results in variations in the spatial and temporal distribution of the light. Therefore, at the end of the fiber spatial distribution of the light and/or its wavelength changes.

In this thesis, nonlinear interactions in multimode fiber are explored and controlled for laser, computing and machine learning applications. Novel approaches for scalable energy-efficient optical computing, learning, and controlling nonlinear dynamics with machine learning tools, ultrashort pulse generation with superior beam qualities, high peak power and stability are demonstrated.

Firstly, high-power ultrashort pulse generation in multimode laser cavities is explored. By studying pulse dynamics, significant improvements are achieved and near-single mode output beam profiles are demonstrated. Later, a novel all-fiber laser design is presented to achieve stable ultrashort pulses with a compact and low-cost laser cavity. In the second half of this thesis, machine learning tools are utilized to acquire the relation between the nonlinear frequency generation and the initial excitation of the multimode fibers to create tunable frequency sources. Advanced artificial neural network designs are implemented to learn nonlinear light propagation in multimode fibers to replace time consuming conventional simulations. Finally, the nonlinear interactions shaping the propagating beam distribution are employed to process information to perform optical computing with multimode fibers.

Multimode fibers are an ideal testbed to investigate complex nonlinear dynamics in nature. We believe the demonstrated applications and the achieved results are just a subset of the capabilities of the optical fiber. These approaches can be used as a steppingstone to demonstrate advanced applications with light.

Keywords

Nonlinear fiber optics, mode-locked lasers, optical computing, multimode fibers, machine learning

Zusammenfassung

Multimodale optische Fasern sind das Rückgrat der Telekommunikation und der medizinischen Bildgebung. Wenn Licht mit hoher Intensität durch eine Multimodale Faser propagiert, Photonen und Materie beginnen zu interagieren, was zu einer nichtlinearen Ausbreitung führt. Die nichtlineare Lichtausbreitung führt denn zu Variationen in der räumlichen und zeitlichen Verteilung des Lichtes. Daher ändert sich am Ende der Faserform das Licht und / oder seine Wellenlänge.

In dieser Arbeit, nichtlineare Wechselwirkungen in Multimodale Fasern für Laser-, Computer- und maschinelle Lernanwendungen werden untersucht und gesteuert. Neue Anwendungen für skalierbare energieeffiziente optische Datenverarbeitung, Lernen und Steuern nichtlinearer Dynamik mittels maschinellen Lernens, ultrakurze Impulserzeugung mit überlegenen Strahlqualitäten, hoher Spitzenleistung und Stabilität werden demonstriert.

Zunächst wird die Hochleistungs-Ultrakurzpulserzeugung in Multimode-Laserkavitäten untersucht. Durch das Studium der Pulsdynamik werden signifikante Verbesserungen erzielt und Ausgangsstrahlprofile in der Nähe von Einzelmoden demonstriert. Später wird ein neuartiges All-Faser-Laserdesign vorgestellt, um stabile ultrakurze Pulse mit einer kompakten und kostengünstigen Laserkavität zu erzielen. In der zweiten Hälfte dieser Arbeit werden Werkzeuge des maschinellen Lernens verwendet, um die Beziehung zwischen der nichtlinearen Frequenzerzeugung und der anfänglichen Anregung der Multimode-Fasern zu erfassen, um abstimbare Frequenzquellen zu erzeugen. Fortschrittliche Designs künstlicher neuronaler Netze werden implementiert, um die nichtlineare Lichtausbreitung in Multimode-Fasern zu erlernen, um rechenintensive konventionelle Simulationen zu ersetzen. Schließlich werden die nichtlinearen Wechselwirkungen, die die Ausbreitungsstrahlverteilung formen, verwendet, um Informationen zu verarbeiten, um optische Berechnungen mit Multimode-Fasern durchzuführen.

Multimodale Fasern sind ein idealer Prüfstand, um komplexe nichtlineare Dynamiken in der Natur zu untersuchen. Wir glauben, dass die demonstrierten Anwendungen und die erzielten Ergebnisse nur eine Teilmenge der Fähigkeiten der optischen Faser sind. Diese Ansätze können als Sprungbrett verwendet werden, um fortgeschrittene Anwendungen mit Licht zu demonstrieren.

Schlüsselwörter

Nichtlineare Faseroptik, modengekoppelte Laser, optisches Rechnen, Multimodale Fasern, maschinelles Lernen

Contents

Acknowledgements	v
Abstract	vi
Keywords	vi
Zusammenfassung	vii
Schlüsselwörter	vii
Chapter 1 Introduction	11
Chapter 2 Spatiotemporal self-similar fiber laser	19
2.1 Intoduction	19
2.2 Results	21
2.3 Conclusion	25
Chapter 3 Single mode output by controlling the spatiotemporal nonlinearities in mode-locked femtosecond multimode fiber lasers	26
3.1 Introduction	27
3.2 Method	28
3.2.1 Multimode oscillator simulations	28
3.2.2 Single-pass beam cleaning simulations	29
3.2.3 Experiments	29
3.3 Numerical Studies	30
3.4 Experimental Studies	32
3.5 Discussion	33
Chapter 4 All-fiber spatiotemporally mode-locked laser with multimode fiber-based filtering	36
4.1 Introduction	36
4.2 Numerical results	38
4.3 Experimental results and discussion	39
4.4 Conclusion	41
Chapter 5 Controlling spatiotemporal nonlinearities in multimode fibers with deep neural networks	42
5.1 Intoduction	43
5.2 Numerical Studies	44
5.3 Results	46
5.3.1 Experimental setup and dataset collection	46

5.3.2	Machine learning and controlling nonlinearities	48
5.4	Discussion.....	49
Chapter 6	Predicting spatiotemporal nonlinear dynamics in multimode fibre optics with a recurrent neural network	51
6.1	Spatiotemporal nonlinearities and simulations	52
6.2	Results	54
6.2.1	Temporal results	54
6.2.2	Spatial results.....	55
6.3	Discussion.....	56
6.4	Future directions	57
Chapter 7	Scalable Optical Learning Operator	58
7.1	Introduction	58
7.2	Results	61
7.2.1	Experimental results	61
7.2.2	Physical model	65
7.2.3	Numerical studies	66
7.3	Discussion.....	67
7.4	Outlook and Conclusion	69
7.5	Method.....	70
7.5.1	Experimental setup	70
7.5.2	Numerical Simulations	70
Chapter 8	Conclusion	72
8.1	Summary of the results	72
8.2	Outlook and conclusion.....	73
Appendix A	75
References	85
Curriculum Vitae	92

Chapter 1 Introduction

Low-loss silica glass optical fibers are first presented by Charles K. Kao and George A. Hockham in 1966 [1]. This discovery led to the development of highly pure silica waveguides and implementation of them in telecommunication applications for high bandwidth data transferring [2], [3]. Later, by doping the optical fibers with rare-earth elements (Ytterbium, Erbium, Thulium, Holmium, etc.), optical fiber-based signal amplifiers and lasers are introduced. With high thermal dissipation, relatively high nonlinearity with tight confinement of light, high single-pass amplification ratios and alignment-free design support, optical fibers attracted attention from nonlinear optics to lasers communities [3], [4].

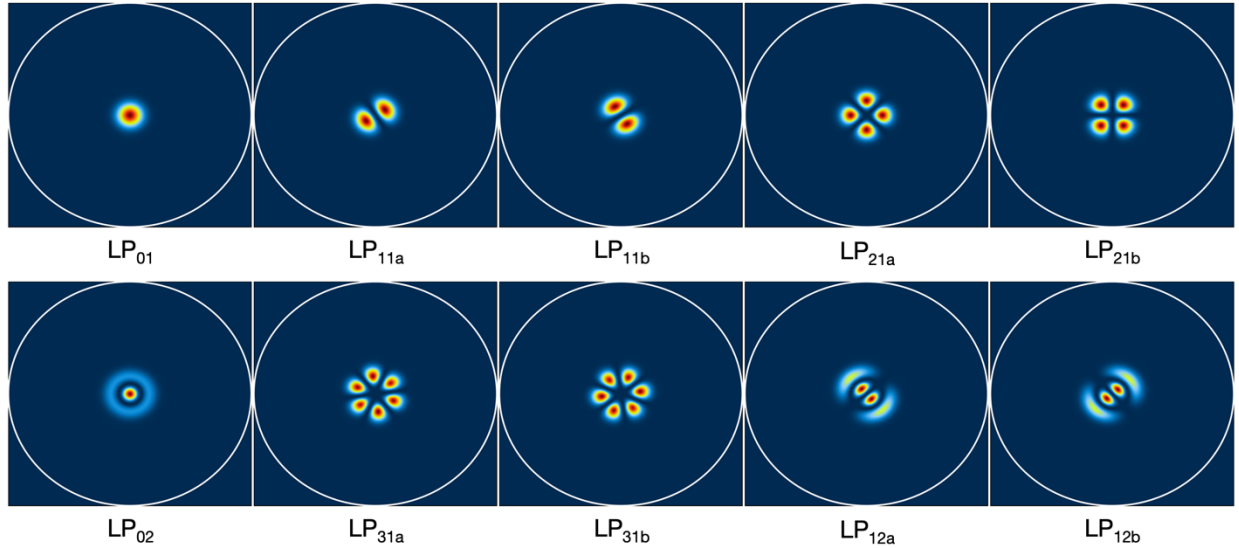


Figure 1.1: Normalized intensity distributions of the first 10 LP modes of GRIN MMF with 50 μm core diameter and 0.20 NA for 1030 nm central wavelength. Fiber core is illustrated with circles.

As a waveguide, optical fiber supports particular and finite spatial distribution of light (spatial fiber modes) to guide the coupled light (see Figure 1.1 for examples). The optical wavelength of the guided light, the refractive index of the optical fiber and its physical dimensions such as core (or cladding) diameter define the finite quantity and the spatial distribution of the guided core (or cladding) modes [4]. As a result, to estimate the number of guided core modes, a dimensionless parameter (V number) is often used which is,

$$V = \frac{2\pi}{\lambda} r NA \quad (1.1)$$

where λ is the wavelength of the light, r is the core radius of the optical fiber and NA is the numerical aperture of the fiber which can be calculated as $\sqrt{n_{core}^2 - n_{cladding}^2}$. Depending on the

shape of the refractive index profile of the fiber (see Figure 1.2), the number of the supported spatial modes can be approximated as $M \approx V^2/2$ for the step-index fibers and as $M \approx V^2/4$ for the graded-index fibers with a parabolic refractive index distribution.

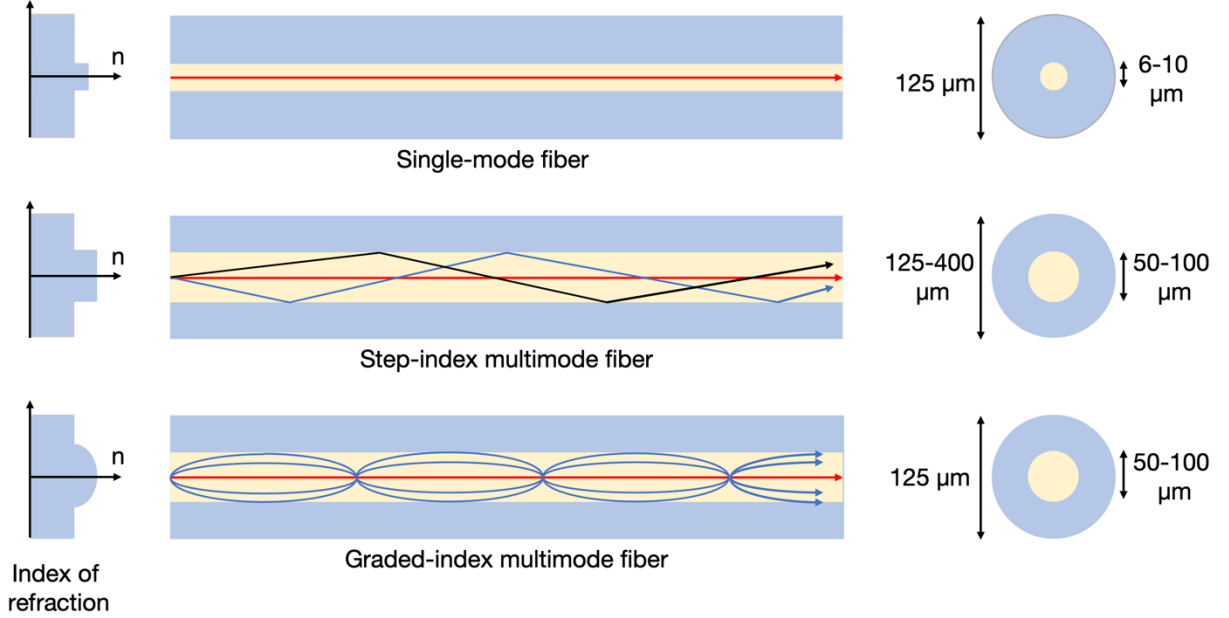


Figure 1.2: Single core fiber types.

Single core fibers can be categorized according to their supported number of modes and their refractive index profiles as illustrated in Figure 1.2. The relatively small core size supports only one spatial mode and such optical fibers are referred to as single-mode fibers. When the core size of the single-mode fiber increased, the optical fiber starts to support more than one spatial mode (see Figure 1.1). Such large core fibers are classified as multimode fibers (MMFs). With the multiple spatial channel support, the MMF technologies are heavily used in telecommunication systems. The step-index MMFs cause relatively high propagation differences (such as dispersion) between the supported modes and these propagation differences result in the spread in time for the propagated light traveling in different modes and called modal dispersion. For long-distance (>km) transmission, the high modal dispersion of an MMF limits the information transmission process. As an alternative to step-index MMFs, graded-index multimode fibers (GRIN MMFs) offer relatively low modal dispersion as a result of the near-parabolic-shaped refractive index profile of the fiber core. Over the last decades, GRIN MMFs are tuned to support large bandwidths with low modal dispersion and low loss for telecommunication purposes [5], [6].

Due to the tight confinement of the guided light, single-mode optical fibers offer high beam quality ($M^2 = 1$ where M^2 is the beam quality factor) and commonly preferred for various applications. This confinement causes relatively high optical nonlinearity due to increasing light-matter interaction with more power per area. Such interactions result in a nonlinear response from the waveguide to propagating guided light since the total polarization ($P(\mathbf{r}, t)$) induced by electric dipoles is

changing nonlinearly with respect to the electric field ($E(\mathbf{r}, t)$) as expressed with the following expression.

$$P(\mathbf{r}, t) = \epsilon_0 (\chi^{(1)} \cdot E + \chi^{(2)} : EE + \chi^{(3)} : EEE + \dots) \quad (1.2)$$

where $\chi^{(i)}$ is the i th order of the susceptibility and ϵ_0 is the permittivity of the vacuum [4]. The aforementioned nonlinear relation causes the Kerr effect which results in a nonlinear change in refractive index $\Delta n = n_2 I$ and stimulated inelastic scattering known as Raman and Brillouin scatterings [4].

Starting from Maxwell's equations, the wave equation for the field propagating inside the optical fiber ($E(\mathbf{r}, t)$) can be expressed as Equation 1.3.

$$\nabla^2 E + \frac{1}{c^2} \frac{\partial^2 E}{\partial t^2} = \mu_0 \frac{\partial^2 P_L}{\partial t^2} + \mu_0 \frac{\partial^2 P_{NL}}{\partial t^2} \quad (1.3)$$

When simplified in scalar notation, Equation 1.3 yields the propagation equation for the slowly varying envelop of a light field ($A(z, T)$). This simplified equation is called as the generalized time-dependent nonlinear Schrödinger equation (NLSE) and described as the following expression.

$$\begin{aligned} \frac{\partial A(z, T)}{\partial z} + \frac{\alpha}{2} A(z, T) + \left(\sum_{n \geq 2} \beta_n \frac{i^{n-1}}{n!} \frac{\partial^n}{\partial T^n} \right) A(z, T) \\ = i\gamma \left(1 + \frac{1}{\omega_0} \frac{\partial}{\partial T} \right) ((1 - f_R) A(z, T) |A(z, T)|^2) \\ + f_R A(z, t) \int_0^\infty h_R(\tau) |A(z, T - \tau)|^2 d\tau \end{aligned} \quad (1.4)$$

where α is gain (loss) term, γ is the nonlinear coefficient, β_n are dispersion coefficients calculated by a Taylor series expansion of propagation constant $\beta(\omega)$ around the center frequency of the field, h_R is the delayed Raman response function and f_R is the fractional contribution of the Raman effect [7], [8]. From self-phase modulation to stimulated Raman and Brillouin scattering, various optical nonlinear phenomena are detailly investigated with single-mode fibers for numerous applications including fiber optical parametric oscillators to Raman lasers [4], [9]. Later these efforts concentrated on single-mode photonic crystal fibers which allow tailoring of nonlinearity and dispersion parameters for specific applications. With tailoring high-order dispersion parameters and increasing nonlinear interactions by decreasing propagation area, octave-scanning coherent supercontinuum generation became feasible [10], [11] which makes optical frequency combs essential for metrology applications feasible [12], [13] by enabling carrier-envelope-offset frequency measurements.

The first mode-locked fiber laser is presented in 1986 by using neodymium-doped fiber as the laser gain [14]. Later, erbium-doped fiber lasers and amplifiers became a mature technology for telecommunication purposes. Following this development, ytterbium-doped fibers with broad spec-

tral bandwidth and high doping are introduced. Starting with soliton (sech^2) pulses, different pulse shapes and propagation regimes introduced to increase pulse energy and decrease the pulse duration in optical fiber oscillators [15]–[20] (see Figure 1.3). The single-mode nature of these fibers provide superior beam quality to ultrashort pulses but due to tight confinement, these fibers also introduce relatively high nonlinearity which prevents high power pulse generation without needing an external amplifier for fiber lasers. To overcome this issue photonic crystal fibers with active element doped cores are introduced [21]–[24]. With large core size and single-mode beam support, these large-pitch fibers make >40 W average powers feasible to achieve directly from a fiber oscillator [24]. However, many advantages of optical fibers such as bending and splicing become challenging with the large-pitch fibers.

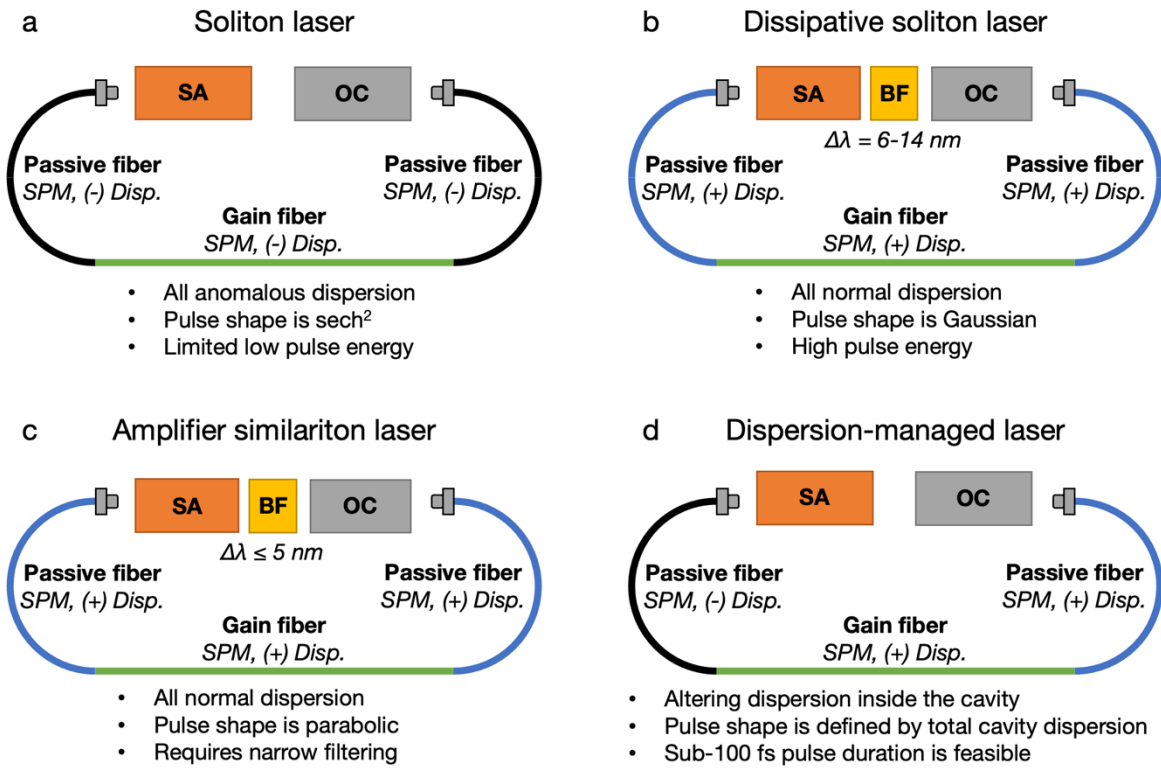


Figure 1.3: Main types of mode-locked fiber lasers and generated pulses.

In recent years, spatiotemporal nonlinearities in GRIN MMFs have become subject to strong attention for nonlinear fiber optics studies. Similar to single-mode fibers, for the slowly varying envelop of a multimode light field ($A(x, y, z, T)$) propagating in GRIN MMF, NLSE with 4D, 3 spatial coordinates + 1 time coordinates,

$$\frac{\partial A(x, y, z, T)}{\partial z} = \frac{i}{2k_0} \left(\frac{\partial^2 A(x, y, z, T)}{\partial x^2} + \frac{\partial^2 A(x, y, z, T)}{\partial y^2} \right) - i \frac{\beta_2}{2} \frac{\partial^2 A(x, y, z, T)}{\partial T^2}$$

$$-i \frac{k_0 \Delta}{R^2} (x^2 + y^2) A(x, y, z, T) + i\gamma |A(x, y, z, T)|^2 A(x, y, z, T) \quad (1.5)$$

where $k_0 = \omega_0 n_0 / c$, ω_0 is center frequency, n_0 is refractive index, R is the fiber core radius and Δ is the relative index difference between the center of the core and the cladding of the fiber. As a simplified model to reach manageable computation times, few coupled time-dependant NLSE for each mode can be studied to understand nonlinear light propagation in GRIN MMFs [25], [26].

$$\begin{aligned} \frac{\partial A_p(z, T)}{\partial z} = & i\delta\beta_0^p A_p(z, T) - \delta\beta_1^p \frac{\partial A_p(z, T)}{\partial T} - i \frac{\beta_2}{2} \frac{\partial^2 A_p(z, T)}{\partial T^2} \\ & + i\gamma \sum_{l,m,n} \eta_{p,l,m,n} A_l(z, T) A_m(z, T) A_n(z, T)^* \end{aligned} \quad (1.6)$$

Here $\delta\beta_0^p$ ($\delta\beta_1^p$) is the difference between first (second) Taylor expansion coefficient of the propagation constant for the corresponding and the fundamental mode, β_2 is the second order dispersion, γ is the nonlinear coefficient and $\eta_{p,l,m,n}$ is the nonlinear coupling coefficient defined by the overlap integral between the modes (F_i) as shown in the following expression.

$$\eta_{p,l,m,n} = \frac{\iint dx dy F_p F_l F_m F_n}{\left[\iint dx dy F_p \iint dx dy F_l \iint dx dy F_m \iint dx dy F_n \right]^2} \quad (1.7)$$

Numerically and experimentally, different nonlinear phenomena and applications reported in recent years with GRIN MMFs. As a frequency conversion technique cascaded Raman scattering generation over 15 Stokes peaks is reported with GRIN MMFs [27]. Later, spatiotemporal instability with nanosecond to femtosecond pulses is demonstrated to achieve frequency conversion with larger frequency shifts (90-120 THz) [28]–[30]. By investigating the anomalous dispersion regime, dispersive wave generation in GRIN MMFs reported with similarly large frequency differences to generate ultrashort pulses at visible and mid-IR wavelengths [31], [32]. Based on Kerr nonlinearity and the propagation with self-periodic imaging, nonlinear self-beam cleaning is reported with passive and Yb-doped GRIN MMFs [33]–[35]. By simultaneously generating spatiotemporal instability, stimulated Raman scattering and harmonic generation with high peak power pulses with low repetition rate, supercontinuum generation in GRIN MMFs reported [36], [37]. Later, cascaded Raman scattering-based supercontinuum generation with around 4W average power is reported with passive GRIN MMFs with different core sizes [38]. The wavelength and power-dependent propagation changes in GRIN MMFs are also utilized as a wavelength filter and saturable absorber elements for mode-locked single-mode fiber lasers [39]–[41].

As an alternative to mode-locked fiber lasers with photonic crystal large-pitch fibers mode-locked lasers, the GRIN MMF-based spatiotemporal mode-locking method is demonstrated to achieve high power mode-locked pulses without needing external amplifiers [42]. The implementation of GRIN MMF segments with large mode support to multimode fiber cavity with few modes provides a self-stable coherent superposition of transverse and longitudinal modes to achieve mode-locked

pulses in 4D. With increasing fiber core size in the oscillator, spatiotemporally mode-locked lasers provide relatively low nonlinearity and high-power pulse generation becomes feasible. The first demonstration of the spatiotemporally mode-locked fiber laser is reported with an all-normal dispersion cavity which supports dissipative soliton (Gaussian-shaped) pulse type [42]. Later with a similar cavity design, demonstrations of the bound state solitons (soliton molecules) and harmonic mode-locking were reported in spatiotemporal mode-locked fiber lasers [43], [44]. Despite using gain fibers with three modes, the aforementioned studies reported low output beam quality. Such a drawback prevents the use of spatiotemporally mode-locked lasers for high power laser-related applications.

With the advances in graphics processing unit (GPU) technologies and compatible parallelized algorithms, machine learning tools have attracted great interest from various communities including physical sciences. Particularly, artificial neural networks with their capacity to grasp complex relations and patterns in a high number of data utilized to understand, analyze and predict nonlinear dynamics. Depending on the complexity of the targetted system and type of the available data, the most commonly used supervised learning (learning with labeled examples) implementations are feed-forward, convolutional and recurrent neural network architectures [45]. Feed-forward neural networks are relatively simple and consist of fully connected nodes without feedback. On the other hand, convolutional neural networks (CNNs) contain convolutional layers with designated image processing tools such as convolution kernel sizes to study visual data types and are commonly used in computer vision [46]. Last but not least recurrent neural networks (RNNs) are well suited for sequential data types such as temporally changing dynamics with the advanced long-short term memory unit blocks in neural network architectures [47]. In photonics, by using the aforementioned deep neural network (DNN) architectures, pulse characterization and shaping [48]–[51], mode-locking of lasers [52], imaging through MMFs [53], [54] and prediction of nonlinear phenomena in single-mode fibers [55], [56] were demonstrated in recent years.

Information processing is an intrinsic part of optics such as free-space propagation of light can be described as a convolution with a fixed kernel and one can easily obtain the 2D Fourier transform of light distribution in space while focusing it with a simple lens in a particular configuration [57], [58]. Based on the aforementioned Fourier transformation property, the first optical correlator is demonstrated in 1964 [59]. Starting with the Hopfield model in 1985, various optical solutions are proposed to address challenges in machine learning, particularly neural networks [60], [61]. With the large operation count, relatively high inference speed and low energy consumption, optical computing solutions focused on machine learning applications promise an alternative direction in the computing paradigm. The main challenges of optical computing are optimizing the optical system to increase the performance similar to the training process of the digital neural networks and implementing optical nonlinear activation functions. Recently the neuromorphic computing schemes such as reservoir computing [62], [63] and extreme learning machines [64], machine learning tools that operate with fixed weights, attracted huge attention from the physical computing community [65]. Largely based on the random transformation of information through diffus-

ing media, different optical computing schemes are adapted to the reservoir computing concept with scattering media and MMFs [66]–[71].

The main theme of this thesis is to learn and control spatiotemporal nonlinear interactions in multimode fibers for applications including lasers, machine learning and optical computing. This study enables us to generate tunable nonlinear frequency generation, optical computing with low energy consumption and high power and compact laser sources. The first part of this thesis (chapter 2, 3 and 4), focuses on mode-locked multimode laser studies and in the second part of this thesis (chapter 5, 6 and 7) single-pass optical nonlinear interactions are studied and utilized with machine learning tools and applications.

Spatiotemporally mode-locked fiber lasers offer high power pulse generation but suffer from low beam quality. This drawback limits this recent laser type with fundamental studies and creates a significant disadvantage for applications. In chapter 2, we aim to solve this problem by generating different pulse types in a multimode mode-locked laser cavity where the spatial distribution of the pulses alters as well. We select amplifier similariton (parabolic shaped) pulse generation [17] as our goal since this particular pulse-type offers relatively short intracavity pulse durations (high intracavity peak power) to encourage nonlinear Kerr beam cleaning [33] with mode-locking. With this pulse type, we experimentally achieved 2.4 nJ pulses with 192 fs compressed pulse duration and near- Gaussian beam quality ($M^2 < 1.4$).

Encouraged by the beam quality improvements with a new pulse type as we report in chapter 2, in chapter 3, we aim to achieve a perfect Gaussian (single-mode) beam profile with high pulse energy by designing a dispersion-managed laser cavity to tailor spatiotemporal intracavity pulse propagation. The dispersion-managed cavity design [18] allows us to control temporal pulse duration inside the cavity and tune the shortest pulse duration with maximum peak power before the GRIN MMF section to achieve nonlinear Kerr beam cleaning [33]. Our numerical and experimental studies verify the nonlinear beam cleaning in the mode-locked multimode laser. With this method, we report 24 nJ pulses with sub-100 fs compressed pulse duration and single-mode ($M^2 < 1.13$) beam profile.

In chapter 4, we report an all-fiber spatiotemporally mode-locked laser design. All-fiber lasers offer a compact and stable solution to applications needing ultrashort pulses. All-fiber multimode lasers with Yb-gain are a challenge due to the mode-locked regime requiring bandpass filters with relatively large bandwidths. In this study, we implement a multimode interference-based filtering approach in a multimode laser cavity and obtained mode-locked pulses with 12 mW average power, 6.24 ps duration at 1036 nm central wavelength. With its inherent alignment-free construction, the presented method offers a compact, stable and low-cost laser solution.

In chapter 5, we study to learn and control nonlinear frequency generation in GRIN MMF with a deep neural network. We first numerically study the effect of the multimode fiber excitation condition on nonlinear pulse propagation. Encouraged by the significant changes in the simulation results, we performed experimental studies to generate datasets to link nonlinearly broadened

spectra with shaped beam patterns to excite the GRIN MMF. The recorded nonlinear relation between these parameters is grasped by digital neural network architectures. The trained neural networks are later employed to generate tailored nonlinearly broadened spectra within the nonlinear phenomena supported by the interested pulse peak power ranges.

In chapter 6, we utilize an RNN type machine learning architecture [55] to learn and predict nonlinear dynamics in GRIN MMFs. The aforementioned numerical pulse propagation algorithms for MMFs (Equation 1.2 and 1.3) require computationally heavy and time-consuming calculations. Numerically generated nonlinear propagation of ultrashort pulses is utilized to train the RNN architecture for temporal and spatial pulse evolution predictions. We demonstrated that a simple RNN structure can grasp the nonlinear spatiotemporal propagation of femtosecond pulses. With this method, we achieved 40 times less time-consuming pulse propagation simulations with trained RNN when compared with the equivalent beam propagation simulations based on Equation 1.5.

In chapter 7, we utilize nonlinear coupling between the modes of a GRIN MMF for optical computing applications. Similar to reservoir computing [62], [63] and extreme learning machine [64] approaches, we investigate the possibility of nonlinear information processing via transmitting information-carrying high peak power pulses through GRIN MMF. With this optical method, we report machine learning applications with accuracies comparable to digital implementations. The demonstrated optical computing framework based on spatiotemporal nonlinear effects is versatile and implemented for a range of learning tasks from classifying images and speech recognition to predicting age from face images.

Chapter 2 Spatiotemporal self-similar fiber laser

This chapter is the postprint version of the following article published in *Optica*.

Spatiotemporal self-similar fiber laser

Uğur Teğın^{1,2}, Eirini Kakkava¹, Babak Rahmani², Demetri Psaltis¹, Christophe Moser²

¹*Optics Laboratory, École Polytechnique Fédérale de Lausanne, Lausanne, 1015, Switzerland*

²*Laboratory of Applied Photonics Devices, École Polytechnique Fédérale de Lausanne, Lausanne, 1015, Switzerland*

Optica Vol.16 Issue:11 (2019)

<https://doi.org/10.1364/OPTICA.6.001412>

In this study, we demonstrate, to the best of our knowledge, the first spatiotemporally mode-locked fiber laser with self-similar pulse evolution. The multimode fiber oscillator generates parabolic amplifier similaritons at 1030 nm with 90 mW average power, 2.3 ps duration, and 37.9 MHz repetition rate. Remarkably, we observe experimentally a near-Gaussian beam quality ($M^2 < 1.4$) at the output of the highly multimode fiber. The output pulses are compressed to 192 fs via an external grating compressor. Numerical simulations are performed to investigate the cavity dynamics which confirm experimental observations of self-similar pulse propagation. The reported results open a new direction to investigate new types of pulse besides beam shaping and nonlinear dynamics in spatiotemporal mode-locked fiber lasers.

2.1 Introduction

For single-mode fiber lasers, ytterbium-based laser systems are generally preferred to achieve high power pulses with relatively broadband spectra. Over the years, dispersion engineering techniques have been demonstrated to obtain various ultrashort pulse types in ytterbium-based fiber cavities such as soliton [72], dispersion-managed soliton [18] and dispersion-managed self-similar pulses [73]. These pulse types require dispersion mapping inside the cavity. For ytterbium-based fiber lasers this can be achieved with the bulk grating compressor or dispersion shifted photonic crystal fibers. In 2006, Chong et al. demonstrated the first dissipative soliton pulse formation with an all-normal-dispersion cavity [19]. For ytterbium-based laser systems, all-normal dispersion cavities provide a simple platform to build all-fiber dissipative soliton lasers [41], [74]. The generation

of mode-locked dissipative soliton pulses is attributed to spectral intracavity filtering by using 8-12 nm bandpass filters. Interestingly, when the intra-cavity bandpass filter becomes narrow (≤ 4 nm), the temporal pulse shape changes from Gaussian to parabolic [17]. Renninger et al. reported this phenomenon in all-normal-dispersion cavity design, with strong spectral filtering, a self-similar pulse can be generated in the gain segment of the laser cavity. These self-similar pulses are referred to as amplifier similariton pulses. Initially, such self-similar pulses based on strong filtering and amplifier scheme were studied and proposed in fiber amplifiers [16], [75] as an alternative to chirped pulse amplification [76]. Moreover, these pulses are a class of solution to the nonlinear Schrödinger equation including a gain term and transform nonlinear phase to a form of linear frequency chirp [16]. The amplifier similaritons pulses and their generation mechanism and intracavity propagation behavior are different than dispersion-managed similaritons which do not require strong spectral filtering and feature parabolic spectral shape. Compared to dissipative soliton and dispersion-managed similariton pulses amplifier similaritons experience large spectral breathing (the ratio of spectral bandwidth before and after the spectral filter is >5). This distinctive behavior generates mode-locked pulses with a broader spectrum and hence potentially shorter pulse duration. Because the chirp of the output pulse depends solely on the gain segment, the amplifier similariton pulses also feature less chirp than given by the total cavity dispersion [17]. Recently, Ma et al. demonstrated an ytterbium-based all-normal self-similar mode-locked fiber laser tunable from 1030 nm to 1100 nm by suppressing amplified spontaneous emission by heating the gain fiber [77]. So, far these studies were done in single-mode laser cavities.

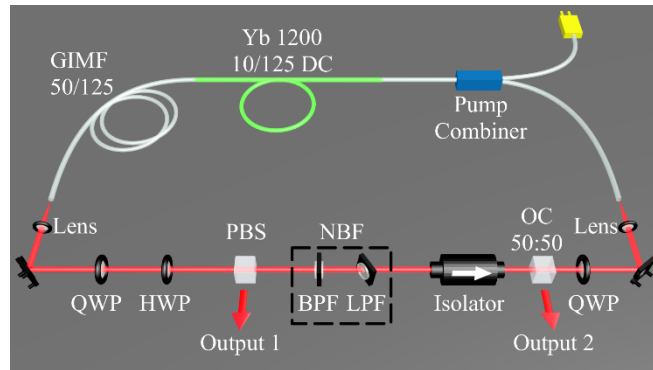


Figure 2.1: Schematic of the spatiotemporal self-similar fiber laser: QWP, quarter-wave plate; HWP, half-wave plate; PBS, polarizing beam splitter; NBF, narrow bandpass filter; BPF, bandpass filter; LPF, long-pass filter; OC, output coupler; GIMF, graded-index multimode fiber.

In recent years, graded index multimode fibers (GIMFs) have become subject to extensive study due to their unique nonlinear properties and potential higher power handling capacities. With low modal dispersion and periodic self-imaging, spatiotemporal pulse propagation of high power pulses in GIMF generates interesting nonlinear effects such as spatiotemporal instability [28], [30], dispersive wave generation [31], graded-index solitons [78], [79], self-beam cleaning [33], nonlinear pulse compression [80] and supercontinuum generation [36], [38]. In addition to the aforementioned studies, spatiotemporal mode-locking was demonstrated with graded-index multimode fibers in multi-mode fiber laser cavities by Wright et al. [42]. Later, observations of the bound state solitons (soliton molecules) and harmonic mode-locking reported in spatiotemporal mode-

locked fiber lasers [43], [44]. All of these studies presented laser cavities featuring dissipative soliton pulses with Gaussian temporal profile and low output beam quality. However, to the best of our knowledge, there are no reports on the generation of different temporal pulse types than dissipative solitons in spatiotemporal mode-locked lasers.

2.2 Results

Here, we present the first spatiotemporal self-similar fiber laser capable of generating amplifier similariton pulses with a parabolic temporal shape. Interestingly, the train of the mode-locked pulse coming out of the 250 mode GIMF has a stable good beam quality of M^2 -value <1.4 . The presented laser is an all-normal-dispersion cavity containing a GIMF with 50 μm core diameter, a step-index multimode gain and passive fiber segment both with a 10 μm core diameter. Mode-locking is achieved by nonlinear polarization evolution (NPE) [81]. A narrow band-pass spectral filter with 3.8 nm bandwidth is constructed with a cascade of a bandpass filter with 10 nm bandwidth and a tilted longpass filter. First, numerical simulations are performed to investigate the possibility of amplifier similariton formation in the multimode laser cavity. Encouraged by the numerical simulations, experimental studies were performed with numerically obtained cavity parameters such as fiber length of each cavity segment. We experimentally achieved self-starting mode-locking for which the laser generates amplifier similaritons at 1030 nm with 90 mW average power, 2.4 nJ pulse energy and 38 MHz repetition rate. The experimental results indicate that the pulse experiences 6-fold increase in its spectral width inside the laser cavity. The chirped output pulse duration is measured as 2.3 ps which is remarkably short when compared with the group-velocity dispersion of the laser cavity. Both features point to an amplifier similariton behavior. The chirped output pulses are externally compressed to 240 fs by a grating pair as measured by a second-order autocorrelation. By reconstructing the pulse profile using the phase and intensity from cross-correlation and spectrum only (PICASO) method [82], we obtained a 172 fs pulse duration with a parabolic temporal shape. The schematic of the fiber laser is illustrated in Figure 2.1. The numerical simulations are performed based on this cavity design to investigate the possibility of self-similar pulse formation. We have performed a simulation of spatiotemporal mode-locking with the model proposed by Wright et al. [42]. A multimode nonlinear Schrödinger equation is solved for the GIMF segment by considering the first 6 LP modes with cylindrical symmetry (more details of simulations can be found in <https://doi.org/10.6084/m9.figshare.9973421.v1>) [6]. A Gaussian intracavity bandpass filter is assumed with 4 nm spectral bandwidth. A stable mode-lock regime is achieved after 30 round-trips as illustrated in Figure 2.2. In the gain fiber, a substantial spectral broadening is observed and after the GIMF segment, the spectral bandwidth of the pulse reaches 25 nm. This broad spectrum is reduced to 4 nm with a bandpass filter. Thus, the pulse experiences more than 6 times spectral broadening in one round-trip (Figure 2.2 b). The temporal profile of the pulse is presented in Figure 2.2 c and at the output 1 (before filter) and output 2 (after the filter), a pulse duration of 3.3 ps and 1.2 ps are achieved respectively. As it is presented in Figure 2.2 d, at the end of the gain segment of the cavity parabolic pulse shape, is obtained which validates the amplifier-similariton pulse formation. Numerically obtained beam profile at output 1

is demonstrated in Figure 2.2 e. Output 1 and output 2 are the NPE output and the 50:50 output couplers, respectively. For numerical simulations, 2.51 nJ pulse energy is observed at the output 1.

The experiments were then performed with the numerically designed cavity. A pump combiner with 10 μm core diameter is integrated to the cavity to couple the 976 nm high power fiber-coupled diode laser for pumping the 1.5 m highly doped ytterbium fiber (nLight Yb-1200-10/125) gain segment. The fiber sections with 10 μm core diameter support 3 modes at 1 μm . This passive fiber section with 10 μm core diameter is 1.8 m long. In order to excite the higher order modes of the 250 mode GIMF (Thorlabs GIF50C), the gain fiber is spliced to the 2 m GIMF with a small off-set (5 μm). Mode-locking was achieved by adjusting the intracavity wave plates. At approximately 1.5 W pump power, self-starting mode-locking with a repetition rate of 38 MHz is observed. Experimentally obtained optical spectra and beam profiles from the output couplers before and after the bandpass filter are presented in Figure 2.3. A drastic improvement is observed in output beam profile when the laser operation changed from continuous-wave to mode-locked (see Figure 2.3 b and Figure 2.3 d). The spectral width of the amplifier similariton pulses reach to 24 nm after the GIMF

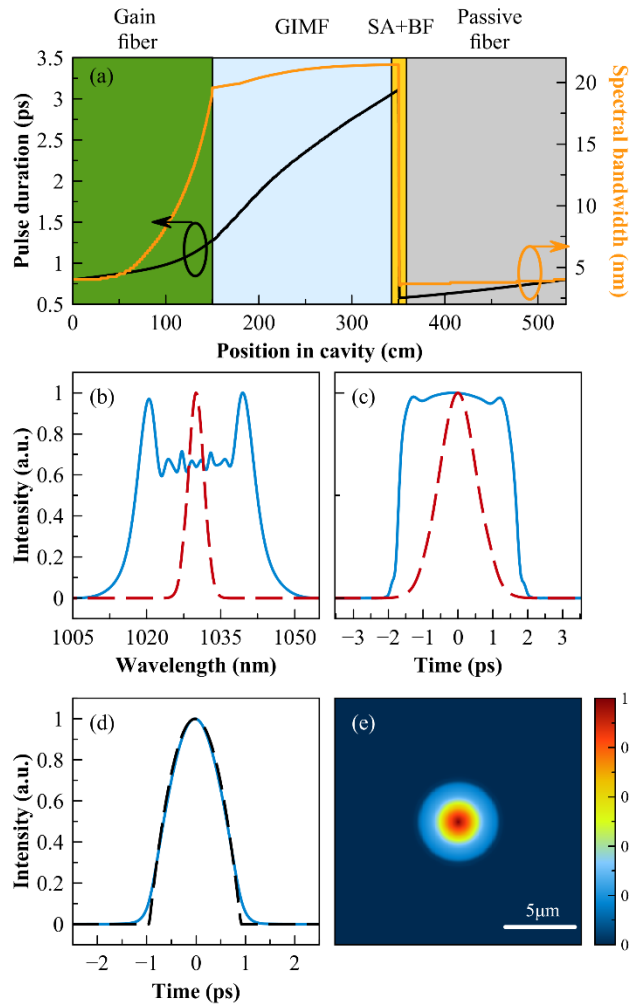


Figure 2.2: (a) Simulated pulse duration and spectral bandwidth variation over the cavity: SA, saturable absorber; BF, band- pass filter. (b) Simulated laser spectra and (c) temporal profile obtained at output 1

(solid) and output 2 (dashed). (d) Pulse shape at the end of gain fiber (solid) and theoretical fit with chirp-free parabolic pulse shape (dashed). (e) Numerically obtained beam profile at output 1.

and the spectral profile is reshaped to 3.8 nm with the narrow bandpass filter. This result is consistent with the pulse breathing ratio of >5 found after one round-trip in a single-mode amplifier similariton laser [17]. The measured output power of the laser is 90 mW and 10 mW at the output 1 and output 2, respectively. After the narrow bandpass intracavity spectral filter, the pulses experience spatial filtering due to the aperture of the isolator (see Figure 2.3 a-inset). We observe that spatial filtering is necessary to achieve spatiotemporal mode-locking similarly to dissipative soliton pulses in multimode fiber lasers [42], [43]. Beam profiles are measured by a 4f-system with 1.5 magnification. As shown in Figure 2.3 b, the beam at the output port 1, which is immediately after the 250 mode GIMF, has a near symmetric shape. M^2 -measurements are performed to determine the quality of this beam and presented in Figure 2.4 a. We experimentally observed a nice beam quality with $M^2 < 1.4$ for the main output (output 1) port of the cavity. For a single pass propagation configuration Krupa et al. presented a drastic improvement in beam profile for a pulse with approximately 1 kW peak power at the end of a 12 m GIMF with 50 μm core diameter [33]. Compared to their observation, after the gain segment of the cavity, peak power of mode-locked pulses is around 6 kW and they undergo 2 m spatiotemporal propagation inside a GIMF with the same core size. We believe by

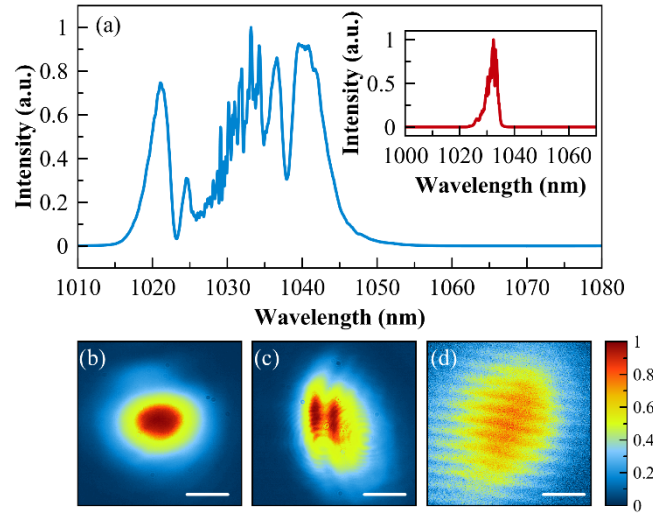


Figure 2.3: (a) Measured spectrum from output 1 and output 2 (inset). Measured beam profiles case from output 1 (b) and output 2 (c) for mode-locked operation. (d) Measured spatial beam profile from output 1 for continuous-wave operation case. Scale bars indicated in beam profiles are 520 μm .

accumulating every roundtrip in a mode-locked cavity, a similar beam cleaning effect is most likely responsible for the clean beam profile we observed. We perform numerical studies to investigate the evolution of the beam profile inside the GIMF. Single-pass propagation simulations considering 10 LP modes with various initial conditions are simulated and energy transfer to lower order modes from higher order modes observed. On the other hand, numerical simulations to study the effect of pulse shape to mode-locked beam quality of the multimode fiber laser are performed as well. We observe a significant difference in

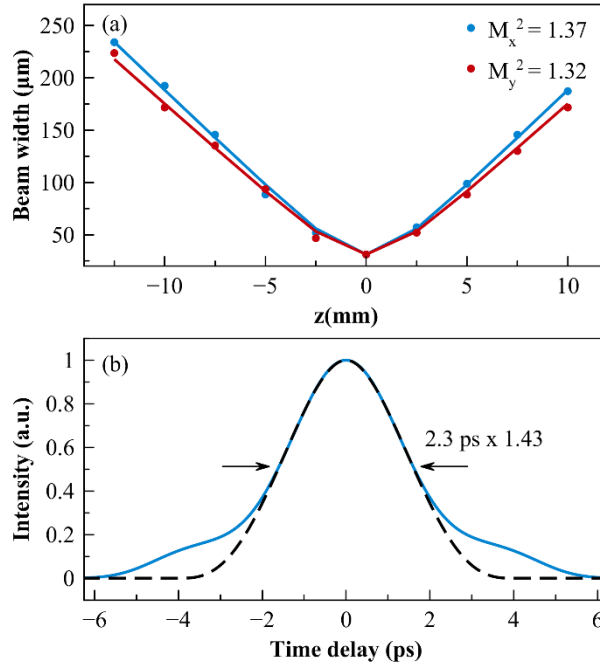


Figure 2.4: (a) M^2 -measurement of the beam from output 1. (b) Autocorrelation trace of the chirped pulse measured from output 1 (solid) and theoretical fit with chirp-free parabolic pulse shape (dashed).

beam profiles in the simulated dissipative soliton pulses and amplifier similariton pulses. In our studies for various excitation conditions, the amplifier similariton pulses feature more confined spatial energy distribution than the Gaussian pulses. For both studies, more details of the simulations can be found in <https://doi.org/10.6084/m9.figshare.9973421.v1>. When coupled-mode analysis is considered for a multimode fiber, the effect of the shape of evolving envelope in the fiber modes on the complex electric field is distinct. When compared with the Gaussian pulse shape, parabolic pulse shape causes more confined energy distribution in space. Thus we believe the better beam quality observed in our experiments is due to the generation of amplifier similaritons in the mode-locked MMF laser.

For the pulses from output 1, no secondary pulse formation or periodic oscillation of the pulse train was observed. The duration of the chirped output pulses is 2.3 ps with a 1.43 deconvolution factor as shown in Figure 2.4 b. The chirped pulse duration is remarkably small for an all-normal-dispersion cavity with total cavity dispersion 0.13ps^2 and it validates the self-similar behavior of the pulses inside the laser cavity. These pulses are dechirped (compressed) using an external grating compressor with a 300 line/mm diffraction grating pair to 192 fs (Figure 2.5 a). We utilize the PICASO algorithm to retrieve the temporal profile from the spectrum and autocorrelation data. As presented in Figure 2.5 b, the resulting pulse features 172 fs pulses duration with a parabolic temporal profile.

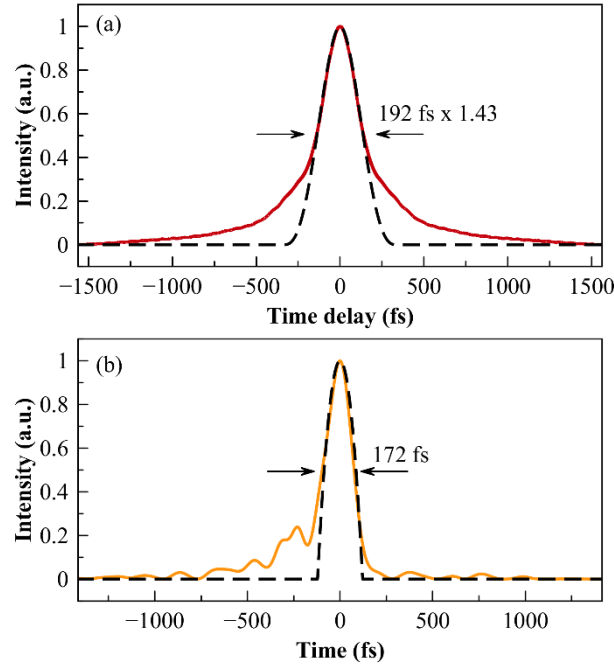


Figure 2.5: (a) Autocorrelation trace of the compressed pulse measured from output 1 and theoretical fit with chirp-free parabolic pulse shape (dashed). (b) PICASO retrieved dechirped pulse shape and parabolic pulse shape fit (dashed).

We test the power handling capacity of the spatiotemporal self-similar fiber laser, by gradually increasing the pump power. Up to 195 mW average power from output port 1, a mode-locked operation with a single pulse on a cavity round-trip, was maintained. This average power was achieved with 2.1 W pump power level. Pulses were yielding 5.1 nJ pulse energy. A broader spectrum (>35 nm) is obtained but the temporal pulse shape is degraded and the compressed pulse duration is increased (>300 fs).

2.3 Conclusion

In conclusion, we numerically and experimentally demonstrate an all-normal-dispersion ytterbium-based spatiotemporal mode-locked fiber laser supporting self-similar pulse evolution, for the first time in the literature. The laser dynamics are numerically and experimentally validated. We obtained intracavity large spectral breathing (>6) and low chirp of the output pulses. Our observations verified the spatiotemporal self-similar pulse formation and the parabolic pulse generation. The oscillator generates amplifier similariton pulses at 1030 nm with 90 mW average power, 2.4 nJ energy, 2.3 ps duration and 38 MHz repetition rate. Pulses are dechirped to 192 fs via an external grating compressor. Contrary to the beam profile obtained in dissipative multimode mode-locked cavities, we measured a near-Gaussian beam profile of the amplifier similariton pulses with M^2 -value <1.4 . The combination of good beam quality, sub-200 fs self-similar pulse from a multimode cavity is a promising platform to generate high power ultrashort pulses. We believe the reported observations are of great interest for nonlinear pulse propagation, pulse and beam shaping in spatiotemporal mode-locked fiber lasers. The presented technique can find applications in wavelength and pulse shape tunable laser sources.

Chapter 3 Single mode output by controlling the spatiotemporal nonlinearities in mode-locked femtosecond multi-mode fiber lasers

This chapter is the postprint version of the following article published in *Advanced Photonics*.

Single mode output by controlling the spatiotemporal nonlinearities in mode-locked femtosecond multi-mode fiber lasers

Uğur Teğın^{1,2}, Babak Rahmani², Eirini Kakkava¹, Demetri Psaltis¹, Christophe Moser²

¹*Optics Laboratory, École Polytechnique Fédérale de Lausanne, Lausanne, 1015, Switzerland*

²*Laboratory of Applied Photonics Devices, École Polytechnique Fédérale de Lausanne, Lausanne, 1015, Switzerland*

Advanced Photonics, 2(5), 056005 (2020)

<https://doi.org/10.1117/1.AP.2.5.056005>

The performance of fiber mode-locked lasers is limited due to the high nonlinearity induced by the spatial confinement of the single-mode fiber core. To massively increase the pulse energy of the femtosecond pulses, amplification is performed outside the oscillator. Recently, spatiotemporal mode-locking has been proposed as a new path to fiber lasers. However, the beam quality was highly multimode and the calculated threshold pulse energy (>100 nJ) for nonlinear beam self-cleaning was challenging to realize. Here we present an approach to reach high energy per pulse directly in the mode-locked multimode fiber oscillator with a near single-mode output beam. Our approach relies on spatial beam self-cleaning via the nonlinear Kerr effect and we demonstrate a multimode fiber oscillator with $M^2 < 1.13$ beam profile, up to 24 nJ energy and sub-100 fs compressed duration. Nonlinear beam self-cleaning is verified both numerically and experimentally for the first time in a mode-locked multimode laser cavity. The reported approach is further power scalable with larger core sized fibers up to a certain level of modal dispersion and could benefit applications that require high power ultrashort lasers with commercially available optical fibers.

3.1 Introduction

Fiber laser dynamics have been studied extensively in the past decades to generate femtosecond pulses with high energies and peak powers [20]. Numerous laser designs are developed to understand nonlinear wave propagation under partial feedback conditions. By tuning complex cavity dynamics in single-mode fiber cavities, self-organization of longitudinal cavity modes with various temporal profiles and central wavelengths have been realized such as soliton [15], similariton [17], [73] and dissipative soliton [19], [83]. Due to the high spatial confinement in the small single mode fiber core, nonlinear effects appear at moderate peak power in solid cores and the accumulation of excessive nonlinear phase leads to pulse breakup, which then limits the achievable pulse energies.

To overcome this limitation, custom-made sophisticated fibers, having large single mode areas in a photonic crystal fiber (PCF), were proposed to reach the μJ pulse energy level [23], [24]. The fiber used in these demonstrations with its mode field diameter of 70 μm needed to be kept straight to avoid bending losses and ensure stability. They share the same limitations as solid-state lasers in the sense that they are rigid and cannot be spliced with conventional techniques. As a result, such lasers do not share the features of fiber lasers that render them advantageous in practice.

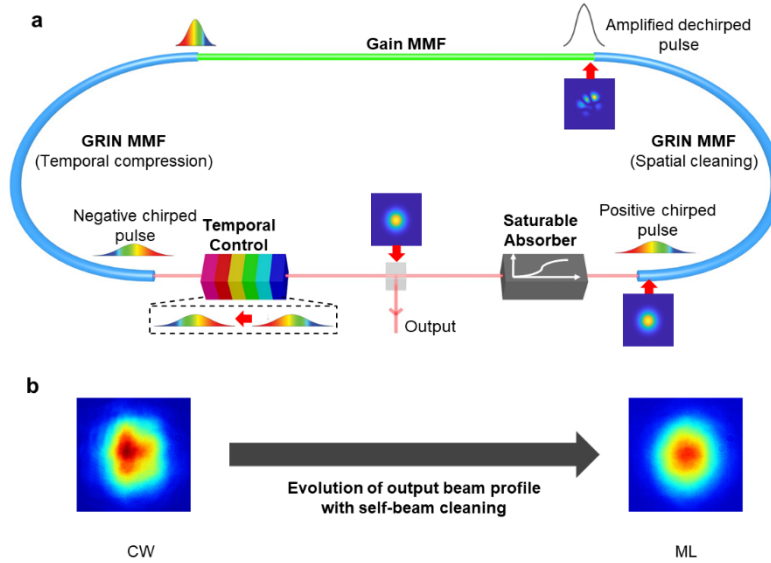


Figure 3.1: Conceptual outline of the multimode fiber cavity and schematic of spatiotemporal mode-locking with beam self-cleaning. a Conceptual outline of dispersion-managed cavity design with indicated temporal dynamics. Laser pumping scheme is not presented. b Schematic of mode-locking mechanism and experimentally measured output beam profile evolution. CW, continuous wave; ML, mode-locked

Recently, spatiotemporal mode-locking has been demonstrated in commercially available MMF cavities with GRIN MMFs by harnessing their low modal dispersion and inherent periodic self-focusing to produce a coherent superposition of transverse and longitudinal modes in an all-normal dispersion regime [42]–[44], [84]. These studies presented cavities with dissipative soliton pulse operation with low output beam quality despite utilizing gain fibers with 3 modes. In a recent study, improvement in the output beam profile of a spatiotemporal mode-locked fiber laser

was reported by changing the generated pulse type from dissipative soliton to amplifier similariton. The reported pulses leading to pulse energies of 2.4 nJ with output beam M^2 value <1.4 [84]. Although better beam profile was reported compared to previous results, single-mode beam profile ($M^2 \sim 1$) could not be achieved due to the limitations of amplifier similariton pulse type such as the degradation of pulse quality and peak power with increasing pulse energy.

In this paper we demonstrate an approach to generate >20 nJ, sub-100 fs pulses with near Gaussian output beam shape by controlling the spatiotemporal cavity dynamics of multimode fiber lasers. This pulse energy represents a tenfold improvement over previously reported MMF oscillators with Gaussian beam shape. Moreover, our method is limited only by the damage threshold of the fiber and splices can be increased to the μ J energy level. The key element in the novel design that enables the increased pulse energy is the Kerr-induced beam self-cleaning in a GRIN MMF [33] that occurs when a high-intensity pulse propagates in the fiber.

The optical wave propagation inside the cavity is designed to synergistically achieve nonlinear beam cleaning and spatiotemporal mode-locking. With our approach, spatiotemporally mode-locked fiber lasers overcome the power limitations of mode-locked single-mode fiber lasers without sacrificing the output beam quality. Moreover, the presented approach is not limited to the demonstrated power levels and theoretically scalable with standard large core multimode fibers up to a certain level of modal dispersion.

We experimentally demonstrate that the highly multimode beam profile observed at the output of a continuous wave multimode fiber cavity is transformed to a stable Gaussian beam profile when the oscillator is spatiotemporally mode-locked. Our numerical studies verified that there is an energy exchange from higher-order modes to lower order modes in the propagating GRIN MMF section of the laser cavity for the experimentally achieved power level. Inside the spatiotemporal mode-locked cavity, Kerr-induced beam self-cleaning creates a minimum loss condition to the emerging mode-locked pulses. The reported multimode fiber laser generates sub-100 fs pulses with high pulse energy (>20 nJ) and good beam quality of M^2 value is less than 1.13.

3.2 Method

3.2.1 Multimode oscillator simulations

Numerical simulations for mode-locked pulse formation are conducted for the model used by Tegin et al. [84]. For GRIN MMF sections of the cavity, a multimode non-linear Schrödinger equation [6] is solved by considering the five linearly polarized (LP) modes (more details of simulations can be found in <https://doi.org/10.1117/1.AP.2.5.056005.s01>). Simplifications such as simulating few-mode fiber sections as single-mode to decrease the computation time and defining coupling ratios before and after the GRIN MMF sections to mimic the effect of splice points are performed. Simulations are initiated with quantum noise fields. The integration step for GRIN MMF sections is defined as the ratio of the self-imaging period of the fiber with 4. For the simulation result shown in Figure 3.1, the gain fiber is modeled with Lorentzian gain shape with 50 nm bandwidth, 30 dB

small-signal gain and 3.2 nJ saturation energy. The coupling condition between the few-mode gain fiber and GRIN MMF is simulated as [20%, 30%, 20%, 20%, 10%]. The intracavity spatial filtering is applied to considered modes by allowing their transmission with [50%, 50%, 50%, 50%, 0%]. The coupling for the field propagating from the GRIN MMF to a few-mode fiber is calculated as a summation of modes with the transmission coefficients [100%, 100%, 100%, 0%, 0%].

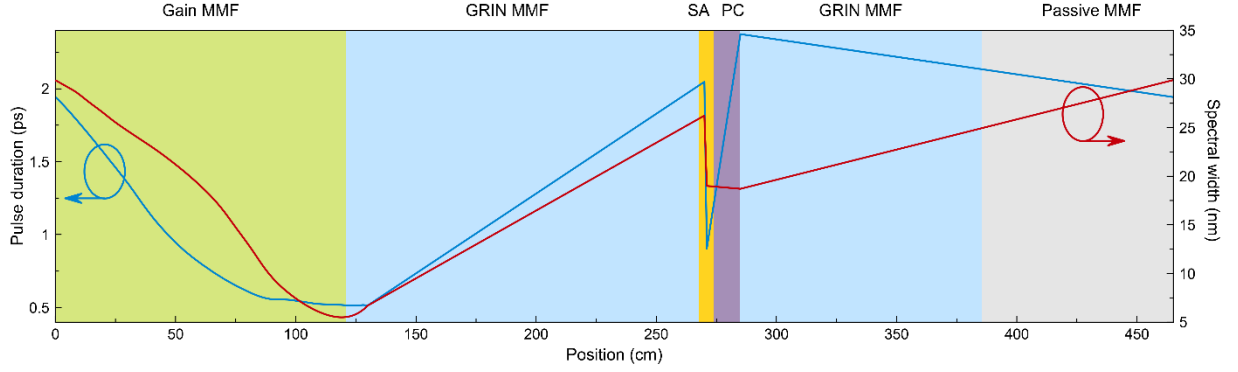


Figure 3.2: Pulse evolution in the laser simulations. Pulse duration and spectral bandwidth variation over the cavity: SA, saturable absorber; PC, pulse compressor.

3.2.2 Single-pass beam cleaning simulations

The simulations regarding beam cleaning are performed by numerically solving a multimode non-linear Schrödinger equation with high numerical accuracy and small integration step. To achieve this goal, the integration step is defined as the ratio of the self-imaging period of GRIN MMF with 20 and the fourth-order Runge-Kutta in the Interaction Picture method is used for accuracy [85].

3.2.3 Experiments

A 20 W, 976 nm pump diode (II-VI Photonics BMU20-976S-01-R) is spliced to the oscillator cavity with a pump combiner (Lightel MPC (2+1) x1) compatible with a 1.3 m MMF gain section (nLight Yb-1200 10/125). To excite the higher-order modes of the GRIN MMF (Thorlabs GIF50E), the gain fiber is spliced to the 1.4 m GRIN MMF with a small offset (5 μm) and coiled with 30 cm diameter to encourage multimode pulse propagation. After the first GRIN MMF section, light is collimated and travels through wave plates, polarizing beam splitter, isolator, grating pair (600line/mm) and spatial filter (randomly placed pinhole). Spatial filtering in spatiotemporal mode-locking is one of the key elements. Its purpose is to restrict the modal content of the intracavity beam. In our experiments with multimode laser cavities, we observed that, in the absence of modal filtering, the mode-locking experiences oscillations in long term operations. In the presented cavity, the effect of the randomly placed pinhole produces experimental mode-locking stability and for different positioning of the pinhole, the spatial beam profiles remained the same. With wave plates and a polarizing beam splitter, NPE is implemented as an artificial saturable absorber. The additional half-wave plate is placed between the polarization-dependent isolator and the grating pair to control the first-order reflection efficiency of the gratings. The free-space ends of the GRIN MMFs are angle-cleaved to eliminate parasitic back reflections. Another GRIN MMF section with 1 m length

establishes the ring cavity loop. Self-starting mode-locking was achieved by adjusting the intracavity wave plates (see Supplementary Video 3 https://www.spiedigitallibrary.org/journals/supplementalcontent/10.1117/1.AP.2.5.056005/AP_2_5_056005_ds003.mov). Spectrum measurements are performed with an optical spectrum analyzer (Ando AQ6317B) and spectrometer (Ocean Optics HR4000-CG-UV-NIR). Beam profile measurements are performed with CMOS cameras (Edmund Optics EO-32121M and Thorlabs DCC1545M). Temporal pulse measurements are performed with an autocorrelator (Femtochrome FR-103). Radio frequency spectrum is measured with HP 3585A spectrum analyzer and >60 dB sideband suppression is reported (see Figure S10 in <https://doi.org/10.1117/1.AP.2.5.056005.s01>).

3.3 Numerical Studies

Our approach is inspired by dispersion-managed mode-locking in single mode lasers which is a method that was initially proposed to overcome the power limitation of soliton mode-locked lasers [86], [87]. Inside a dispersion-managed cavity, the pulse stretches and compresses significantly every round trip while having a near zero net-cavity group-velocity dispersion (GVD). This approach leads to the generation of ultrashort pulses (sub-100 fs) with broad-spectrum and high energy per pulse [18], [88].

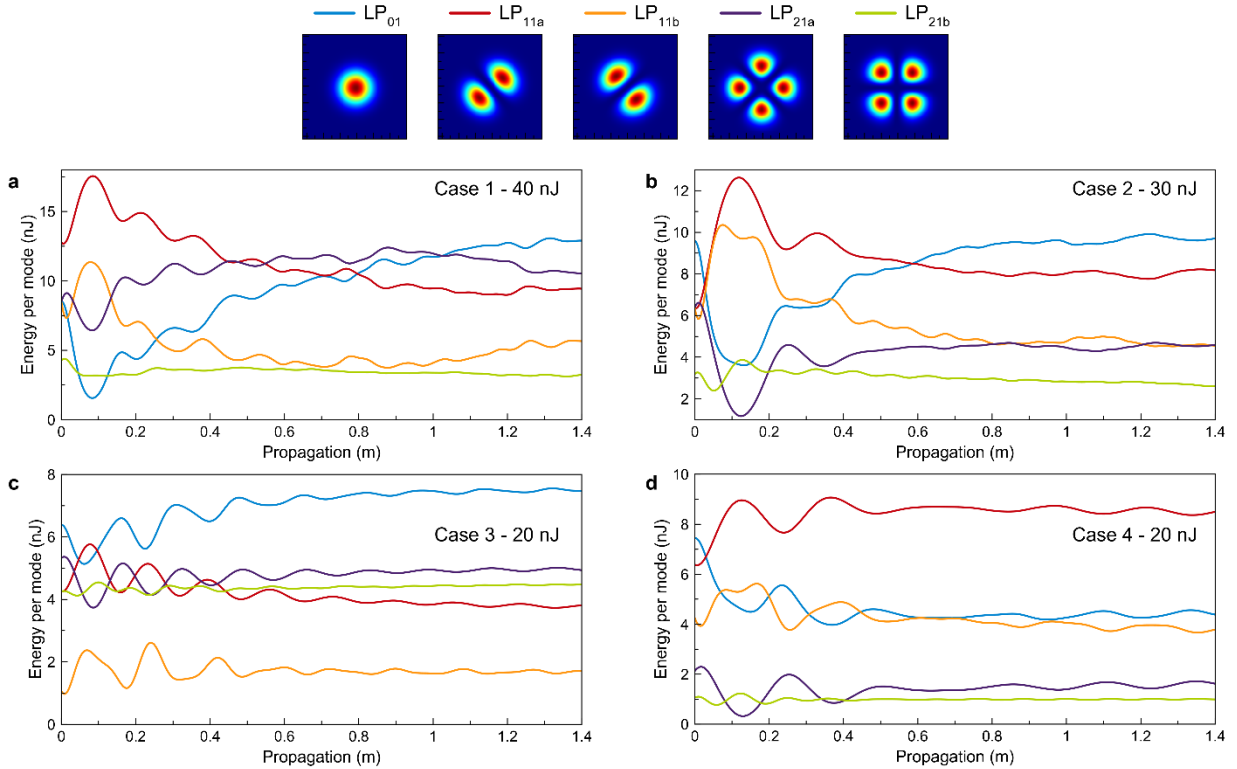


Figure 3.3: Numerical investigation of Kerr-induced beam self-cleaning inside GRIN MMF. Propagation of 450 fs pulse with a 40 nJ pulse energy and [20%, 30%, 20%, 20%, 10%] initial coupling condition, b 30 nJ pulse energy and [30%, 20%, 20%, 20%, 10%] initial coupling condition, c 20 nJ pulse energy and [30%, 20%, 5%, 25%, 20%] initial coupling condition and d 20 nJ pulse energy and [35%, 30%, 20%, 10%, 5%] initial coupling condition.

In our study, the dispersion-managing approach is adapted to a multimode fiber cavity with a similar motivation, to generate intracavity short pulses with high peak powers sufficient to trigger strong spatiotemporal interactions to effect spatial beam clean-up. The proposed cavity is illustrated in Figure 3.1 a. Silica fibers feature positive GVD for the emission wavelengths of the Yb-fiber and stretch the propagating pulse with positive chirp. In our design, a grating pair is placed as a dispersion-balancing section to provide negative GVD values and change the sign of the chirp on the pulse. Such a temporal change causes compression of the propagating pulses in the following fiber sections (GRIN MMF and gain MMF).

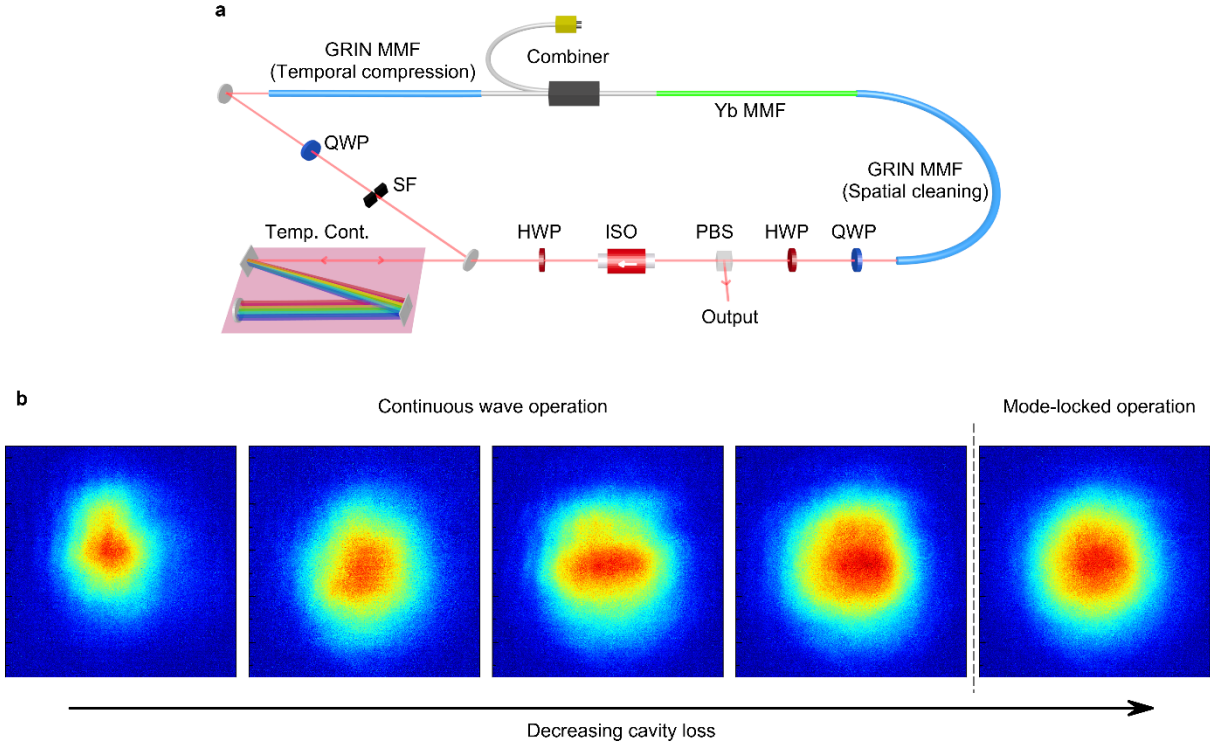


Figure 3.4: Schematic of the laser cavity and beam profile measurements. a QWP, quarter-wave plate; HWP, half-wave plate; PBS, polarizing beam splitter; ISO, isolator; SF, spatial filter. b Evolution of near-field output beam profile for decreasing cavity loss from continuous wave to mode-locked operation for 8 nJ output pulse energy.

We used the multimode nonlinear Schrödinger equation to numerically simulate the multimode laser to analyze pulse propagation dynamics and determine cavity parameters. A stable mode-lock regime after a few round-trips around net cavity GVD $\beta_{(2)\text{net}} = 0.013 \text{ ps}^2$ is achieved and dispersion-managed soliton pulse formation is numerically obtained with various powers and cavity excitation conditions. An example of the evolution of the intracavity pulse in one round trip is illustrated in Figure 3.2 as a function of position inside the multimode cavity. By engineering the cavity dynamics, the shortest pulse duration is achieved at the end of the gain fiber section where the amplification is maximum such that the highest intracavity peak power is obtained in the GRIN MMF section. This unique design can allow pulses to reach the Kerr-induced beam cleaning threshold inside the cavity. In our simulations, the pulse experiences more than 6 times spectral broadening in one round-trip. The temporal profile and spectrum of the output pulse measured at

the nonlinear polarization evolution (NPE) port, are presented in Figure S1a and Figure S1b <https://doi.org/10.1117/1.AP.2.5.056005.s01>. For the simulated cavity, mode-locked pulses with 5.1 nJ energy and 2.12 ps duration Gaussian-like temporal shape are generated from quantum noise. The numerically obtained output beam profile with the considered modes is presented in Supplementary Figure S1c <https://doi.org/10.1117/1.AP.2.5.056005.s01>. For further details and simulations with different multimode fiber excitation conditions, see Methods and <https://doi.org/10.1117/1.AP.2.5.056005.s01>.

To investigate the possibility of the Kerr-induced beam self-cleaning in the cavity, single-pass numerical simulations were performed with high numerical accuracy. The energy exchange behavior between the modes is presented in Figure 3.3. The mode-locking simulations demonstrated in Figure 3.2 suggest ~450 fs pulse duration after the gain section and we numerically investigate the effect of intracavity pulse energy to energy exchange between the modes of GRIN MMF with different initial excitation scenarios. For the excitation case applied in mode-locking simulations between the simulated modes, when the pulse energy reaches to 20 nJ, energy fluctuations between the simulated modes starts to decrease. For a 30 nJ pulse the fundamental mode starts to increase its energy content and for 40 nJ pulse it becomes dominant at the end of the GRIN MMF section of the cavity (see Figure 3.3 a). For different excitation cases, the required pulse energy to achieve similar modal interaction is observed to be lower as it is shown in Figure 3.3 b and Figure 3.3 c. For some cases, we observed that instead of the fundamental mode, an alternative low order mode such as LP_{11b} is observed as a leading mode at the end of GRIN MMF for 20 nJ pulse energy (see Figure 3.3 d). Contrary to single-pass propagation, inside a laser cavity, a small improvement in beam shape can accumulate and a steady-state beam cleaning can be achieved after multiple roundtrips. The aforementioned numerical studies indicate that the pulse energy required for intracavity Kerr-induced beam cleaning is within reach of the designed dispersion-managed multimode cavity.

3.4 Experimental Studies

Guided by the simulation results, the experimental cavity, presented in Figure 3.4 a, is constructed and studied. Here, the utilized fibers are intentionally selected to be identical with the fibers used in the spatiotemporally mode-locked laser literature (GRIN MMF with 50 μm core diameter and Yb MMF with 10 μm core diameter) [42]–[44], [84]. The GRIN MMF supports 240 modes and Yb MMF supports 3 modes around 1 μm central wavelength. Since the previously reported results in the literature feature highly multimode output beam profiles, instead of the Yb MMF, the GRIN MMF is the dominant waveguide inside the cavity. The additional, offset splice and the bending of the GRIN MMF cause multimode propagation to the beam every roundtrip. The offset splice is set to 5 μm difference to core to core between the fibers. The offset splice is set to 5 μm between the two cores of the fibers. In the literature, Sidelnikov et al. studied the optimized initial conditions for single-pass beam cleaning phenomenon. Their results suggest that precisely a 5 μm offset favors nonlinear beam cleaning [89]. The intracavity grating compressor is tuned to provide -0.0987 ps² GVD to compensate 0.1116 ps² GVD of the fiber sections of the cavity each round trip. Single-

pulse mode-locking is easily achieved by adjusting cavity polarization by the wave plates with a repetition rate of 36 MHz. A major improvement from a highly multimode beam profile to a Gaussian-like symmetric beam profile is observed at the laser output when the operation regime changed from continuous-wave to mode-locked [see Supplementary Video 1 https://www.spiedigitallibrary.org/journals/supplementalcontent/10.1117//1.AP.2.5.056005/AP_2_5_056005_ds001.mov]. The Figure 3.4 b presents the multimode nature of the laser cavity for the adjusted cavity loss and the detailed evolution is presented in Supplementary Video 2 https://www.spiedigitallibrary.org/journals/supplementalcontent/10.1117//1.AP.2.5.056005/AP_2_5_056005_ds002.mov. The measured Gaussian-like beam profile remains similar when pulse energy is increased up to 24 nJ by gradually increasing the pump power level. Above 24 nJ output pulse energy, secondary pulse formation is observed inside the cavity as a power limiting factor for the single-pulse operation regime.

We performed a detailed characterization of the laser when the pump power is set to 3.5 W where the laser generates 20 nJ pulses. As expected for a dispersion-managed cavity, pulse spectra with large bandwidth (~40 nm) are measured for this power level [see Figure 3.5 a]. The pulse duration of the chirped pulses is measured with second-order intensity autocorrelation as 3.88 ps with the Gaussian deconvolution factor of 1.414 as shown in Figure 3.5 b. These chirped pulses are later dechirped (compressed) by an external grating compressor with a diffraction grating pair to 97 fs (see Figure 3.5 c). To determine the temporal profile of the pulses from the measured spectrum and autocorrelation data, the PICASO algorithm is employed [82]. The resulting pulse shape features 95.8 fs pulse duration with a Gaussian profile and presented in Figure 3.5 c – Inset. No secondary pulse formation or periodic oscillation of the pulse train is observed (see Supplementary Information II). As presented in Figure 3.5 d, the beam has a symmetric shape and to determine its quality, M^2 measurements are performed. For 20 nJ output pulse energy, average M^2 is measured as 1.13 ($M_x^2 = 1.08$ and $M_y^2 = 1.17$).

3.5 Discussion

To investigate the effect of intracavity pulse energy to output beam profile in detail, we performed M^2 measurements to pulses with different energy by adjusting pump power. For the spatiotemporally mode-locked beam profile, the changes in the output beam quality are challenging to differentiate from the near-field beam profiles but M^2 measurements provide more significant information. In our measurements, we observed that M^2 value is decreasing with increasing pulse energy. For 4 nJ pulses, we measured $M^2 = 1.85$ and it decreased to 1.48 for 7.2 nJ. When the M^2 value (<1.13) for the presented high pulse energy is also considered, this measurement is the experimental proof of the intracavity Kerr-induced beam cleaning in our design. Here we would like to emphasize that the observed M^2 value change from 1.85 to 1.13 is a significant improvement compared to the single-pass beam self-cleaning of ultrashort pulses in the literature where M^2 value improvement is reported only from 2.3 to 1.8 in the initial studies [35]. Recently, by selecting picosecond pulses at 1.5 μm as pump pulses more efficient beam cleaning results are demonstrated in systems with less modal support [90].

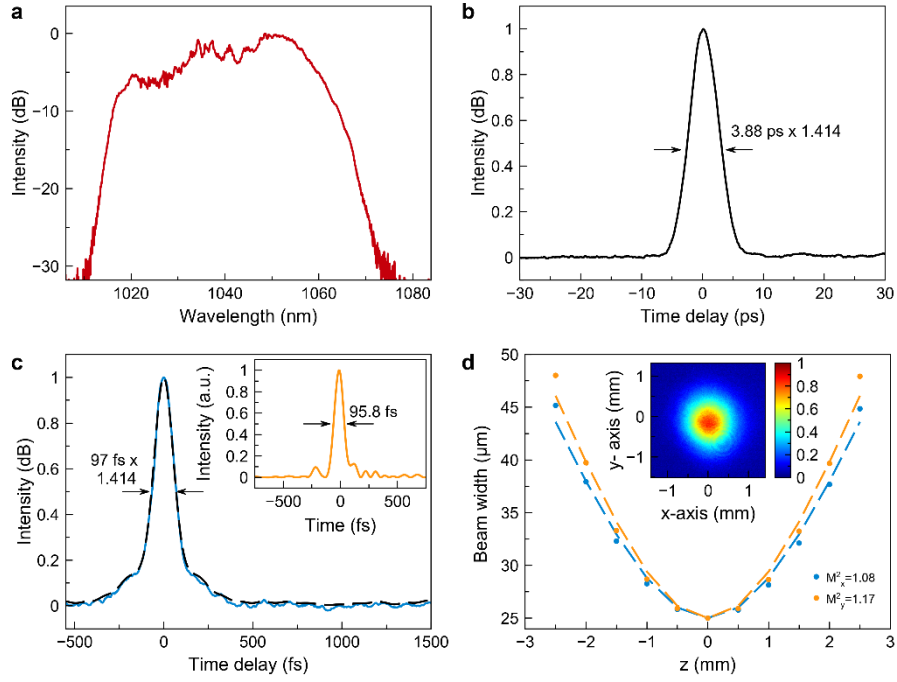


Figure 3.5: Experimental measurements. a Measured mode-locked spectrum. b Intensity autocorrelation trace of the chirped pulse. c Intensity autocorrelation trace of the dechirped pulse, PICASO- reconstructed autocorrelation intensity (dashed) and PICASO-retrieved dechirped pulse shape (inset). d Measured beam profile for mode-locked operation and M^2 measurement of the beam profile.

To understand the beam cleaning mechanism, the effect of the cavity alignment condition on the mode-locked beam profile is investigated. Differences in the free-space orientation of the laser are achieved by changing the cavity alignment and the position of the intracavity spatial filter. We observed that the presented beam-profile remains similar for different alignment configuration although the mode-locked spectrum and pulse energy changes. A comparison of the predicted beam profile by the simulation reveals that experimentally we obtain a much better beam shape (Figure 3.5 d). One of the reasons for this is the limited number of modes in the simulation and the low pulse energy that was simulated. In the single-pass simulations reported in Figure 3.3, we found that with the higher pulse energy beam cleaning improves which is consistent with the experimental result. Also, given the fact that the laser pulse oscillates inside the cavity, a slight improvement in the beam profile due to the Kerr effect during each round trip, enhanced beam self-cleaning is expected.

The differences between the supported number of modes by the multimode fibers used in the spatiotemporally mode-locked laser causes mode dependent loss to the propagating field. For spatiotemporal mode-locking with the presented engineered cavity approach, Kerr-induced beam cleaning can cause a minimum loss condition inside the multimode fiber cavity, similar to the Kerr-lens realization of solid-state lasers. Based on our results, one can explain the measured output beam profile evolution in the laser output with the minimum loss principle [91]. An alternative explanation based on the NPE saturable absorber might also be partly responsible for the beam cleaning experimentally obtained. The NPE mode-locking requires nonlinearly induced polarization

changes to generate saturable absorber behavior. The low order modes of the laser cavity exhibit the highest nonlinear rotation angle, thus modelocking would favor low order modes which might be another reason for the near single-mode output beam profile achieved in the experiment. However, the majority of the previously reported multimode fiber lasers have also employed nonlinear polarization evolution mode-locking technique and they did not observe a high-quality beam profile [42]–[44], [91]. Furthermore, we would like to highlight that, modification/shaping of the beam in free-space propagation has a very small impact to the output field since the light travels through around 4 m coiled multimode fiber with different mode number and splice position. Another important parameter in the demonstrated cavity is the accumulated modal dispersion. Due to the production complexity of gain doped GRIN MMF, we restricted our study of spatiotemporal mode-locking studies to commercially available step-index gain MMFs originally designed for amplifier systems. When compared with the step-index MMFs, the modal dispersion of GRIN MMF segment in the cavity is negligible. For further power scaling by increasing the gain fiber diameter, modal dispersion will be a limiting factor and will be investigated in future work. The aforementioned mechanisms and dynamics need to be further investigated in future work. As an interesting future direction, the real-time dynamics of the spatial, temporal and spectral formation of pulse generation can be investigated numerically and experimentally with DFT based approaches to understand mechanism of spatiotemporal mode-locking in the presence of Kerr-induced beam self-cleaning.

In conclusion, we reported a multimode fiber laser design with intracavity Kerr-induced self-beam cleaning to realize high energy, ultrashort pulses with good beam quality. By engineering nonlinear intracavity propagation of the mode-locked pulses, we numerically and experimentally demonstrated a multimode cavity design with Kerr-induced beam self-cleaning. The presented cavity dynamics show that engineered intracavity temporal pulse properties enable a route to generate high beam quality when mode-locking is achieved. For various alignment orientations and pulse energy, drastic improvement of the output beam profile is experimentally reported when mode-locking is achieved. The presented oscillator generates sub-100 fs pulses with >20 nJ pulse energy while exhibiting good beam quality of M^2 value is less than 1.13. The combination of good beam quality, high pulse energy and sub-100 fs pulse duration from a fiber laser consists of commercially available, standardized components is a promising platform for various laser-related fields. The presented technique can be easily adapted to fibers with a larger core size to increase pulse energy while preserving single-pulse operation with sub-100 fs durations.

Chapter 4 All-fiber spatiotemporally mode-locked laser with multimode fiber-based filtering

This chapter is the postprint version of the following article published in *Optics Express*.

All-fiber spatiotemporally mode-locked laser with multimode fiber-based filtering

Uğur Teğın^{1,2}, Babak Rahmani², Eirini Kakkava¹, Demetri Psaltis¹, Christophe Moser²

¹*Optics Laboratory, École Polytechnique Fédérale de Lausanne, Lausanne, 1015, Switzerland*

²*Laboratory of Applied Photonics Devices, École Polytechnique Fédérale de Lausanne, Lausanne, 1015, Switzerland*

Optics Express, Vol. 28 Issue: 16 (2020)

<https://doi.org/10.1364/OE.399668>

We demonstrate the first all-fiber multimode spatiotemporally mode-locked laser. The oscillator generates dissipative soliton pulses at 1036 nm with 12 mW average power, 6.24 ps duration and 24.3 MHz repetition rate. The reported pulse energy (0.5 nJ) represents ~4 times improvement over the previously reported single-mode all-normal dispersion mode-locked lasers with multimode interference-based filtering. Numerical simulations are performed to investigate the cavity and spatiotemporal mode-locking dynamics. The all-fiber oscillator we present shows promise for practical use since it can be fabricated simply.

4.1 Introduction

Ytterbium-based fiber laser systems are used in optical metrology, material processing and medical applications due to their high and broadband gain [20]. Unlike the other conventionally used gain elements (Er, Tm and Ho), the emission wavelength of an Ytterbium-doped silica fiber falls in a spectral range that exhibits positive group velocity dispersion ($\beta_2 > 0$), thus mode-locking is relatively challenging at 1 μ m wavelength. By using dispersion-management with gratings or photonic crystal fibers, soliton [72], dispersion-managed soliton [18] and similariton [73] pulse types were reported with Ytterbium-based single-mode fiber lasers. Later, all-normal dispersion mode-locking

with spectral filtering of chirped pulses was discovered and depending on the filtering effect, either dissipative soliton [19] or amplifier similariton [17] pulses can be produced. Over the last decade, all-normal-dispersion fiber lasers have been studied mainly by employing dissipative soliton pulse dynamics [83]. These pulses are energy scalable and dissipative solitons with up to μJ pulse energies were demonstrated with custom made very-large mode area single-mode fibers [24].

All-fiber laser designs are a subject of high interest due to their compact and alignment-free operation. To achieve dissipative soliton pulses in an all-fiber configuration various inline fiber-based filtering solutions with $>6\text{ nm}$ bandwidth have been reported in the literature [40], [74], [92], [93]. Among them, multimode interference (MMI) based bandpass filtering is a convenient solution. Such a filter consists of a section of GRIN MMF between single or few-mode fibers. Interference effects between the modes introduces frequency-dependent sinusoidal transmission which can be used as a spectral filter [39]. Recently, dissipative soliton pulse formation with 0.13 nJ energy was presented in an all-fiber configuration with the multimode interference-based bandpass filtering in a single-mode Ytterbium-based all-normal dispersion laser [41].

In the last few years, spatiotemporal mode-locking is demonstrated by harnessing the unique properties of GRIN MMFs such as low modal dispersion and periodic self-imaging by Wright et al. and dissipative soliton pulses [42]. With the mode-locking approach in a multimode laser cavity, coherent superposition of transverse and longitudinal modes is demonstrated. By introducing spatial interactions to mode-locking mechanism complex multimode nonlinear wave propagation studies became feasible under partial feedback conditions. Later, observation of bound-state solitons and harmonic mode-locking were reported with similar cavity orientations [43], [44] and all-fiber cavity with SESAM mode-locking [94]. Recently, self-similar pulse propagation is reported in spatiotemporally mode-locked multi-mode fiber laser and observed output beam quality improvements with the temporal change [84]. By tailoring spatiotemporal nonlinear pulse propagation, intracavity Kerr-induced self-beam cleaning is achieved in a multimode laser cavity with sub-100 fs pulse duration, $>20\text{ nJ}$ pulse energy and M^2 value less than 1.13 [95].

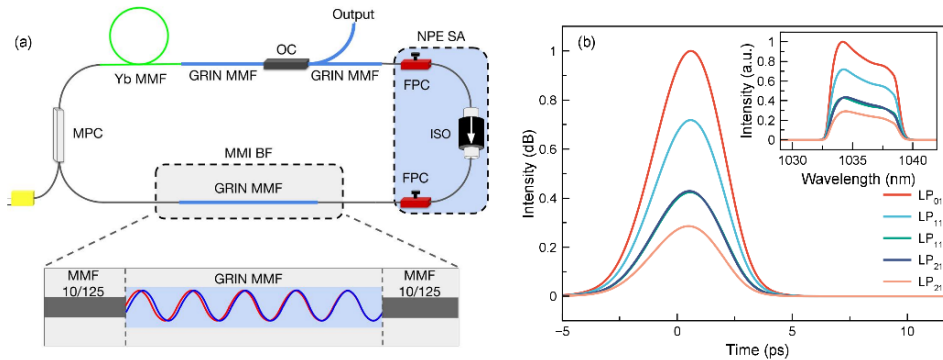


Figure 4.1: (a) Schematic of the all-fiber spatiotemporally mode-locked laser with multimode fiber-based filtering: ISO, isolator; FPC, fiber polarization controller; OC, output coupler; MMI BF, multimode interference-based bandpass filter; MPC, multipump combiner. (b) Simulated mode-resolved temporal profile. Inset: Simulated mode-resolved spectral profile.

The novelty in the current paper is the use of multimode fiber interference-based filtering to construct an all-fiber spatiotemporally mode-locked laser. With this alignment-free, compact cavity design, spatiotemporally mode-locked dissipative soliton pulse generation is demonstrated. Numerical simulations are performed to reveal cavity and spatiotemporal mode-locking dynamics and led to experimental studies. The experimentally demonstrated multimode laser is self-starting and generates pulses with 0.5 nJ energy, 12 mW average power, 6.24 ps duration and 24.3 MHz repetition rate at 1036 nm. With spatiotemporal mode-locking, the achieved pulse energy represents ~ 4 times improvement over the previously reported single-mode mode-locked all-normal dispersion lasers with multimode interference-based filtering.

4.2 Numerical results

The schematic of the all-fiber spatiotemporally mode-locked oscillator is presented in Figure 4.1 a. The cavity consists of a step-index Ytterbium-based MMF segment with 10 μm core diameter, GRIN MMF segments with 50 μm core diameter and step-index passive MMF segments with 10 μm core diameter. The fiber sections with 10 μm core diameter support 3 modes and the GRIN MMF sections with 50 μm core diameter support ~ 240 modes at and around 1030 nm wavelength. Numerical simulations are performed to define lengths of the fiber segments, the bandwidth for multimode interference-based bandpass filtering and the possibility of spatiotemporal mode-locking in the presented cavity design.

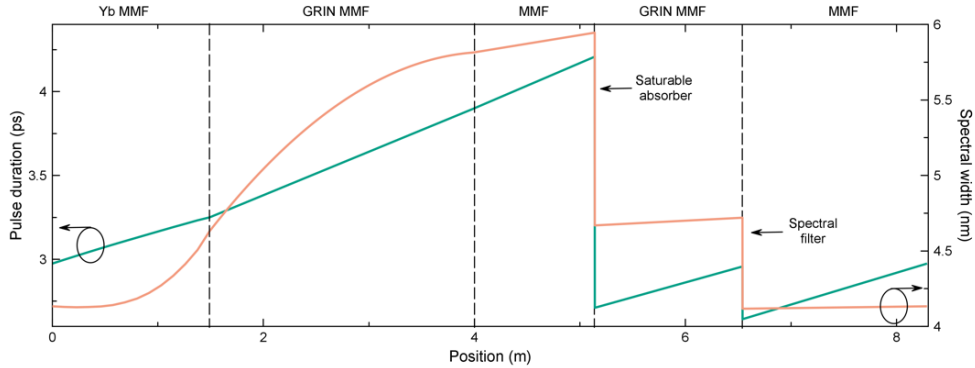


Figure 4.2: Simulated pulse duration and spectral bandwidth variation over the cavity.

Simulations are conducted with the numerical model used by Teġin et al. [84], [95]. The GRIN MMF segments are modeled with linearly polarized modes and the nonlinear multimode Schrödinger equation is simulated for these segments [6]. To decrease the computation time, GRIN MMF segments are considered with five modes (LP_{01} , LP_{11a} , LP_{11b} , LP_{21a} and LP_{21b}), step-index MMF segments with few-modes are considered as single-mode. Only a small portion of the modes (5 out of 250) are included in the simulation due to computational limitations however we will show that this simplified model captures essential features of the behavior of the pulse propagation inside the laser. The step size of simulation was chosen as $\sim 140 \mu\text{m}$ (quarter of the self-imaging period, $560 \mu\text{m}$) for the GRIN MMF and 0.5 cm for few-mode fiber segments with a time resolution of 80 fs with 24 ps time window width. The splice points were modeled by coupling coefficients of the modes before and after the GRIN MMF segments. The initial field in simulations is

defined as a quantum noise and stable mode-locking regimes are found to be not critically dependent on the details of the coupling coefficients. The gain is modeled as Lorentzian shape with 30 dB small-signal gain and 40 nm gain bandwidth. The saturable absorber is modeled by a sinusoidal transfer function with 1 kW saturation power and 60% modulation depth.

The numerically achieved spatiotemporally mode-locked pulse shape and spectrum at the 30% output coupler are presented in Figure 4.1 b. We set the excitation coefficients of the single mode section to the 5 mode GRIN MMF segments equal to [0.35, 0.25, 0.15, 0.15, 0.1] and the gain saturation energy as 1.10 nJ. It is known that in order to achieve dissipative soliton pulses in all-normal dispersion cavities bandpass filtering of chirped pulses with >6 nm bandwidth is required [19]. To ensure dissipative soliton mode-locking, we select the length of the GRIN MMF segment used for MMI filtering to be 25 cm which yields an 8 nm bandwidth bandpass filter [39]. In our simulations, dissipative soliton pulses with 0.46 nJ pulse energies and 5 nm spectral bandwidths were achieved. The output pulse duration was 3.6 ps at the output port. To understand the pulse propagation in detail, propagation of the pulse in one roundtrip is calculated and presented in Figure 4.2. Due to the relatively high nonlinearity, the spectral broadening is observed in gain MMF segment which later reaches a steady-state value inside the GRIN MMF. As expected from dissipative soliton pulses in an all-normal dispersion cavity, the spectral broadening ratio in one roundtrip is small [96]. The output beam profile with the numerically calculated mode-locked field is presented in Figure 4.3. Although most of the energy remains in the lower order modes, the numerically obtained output beam exhibits multimode features.

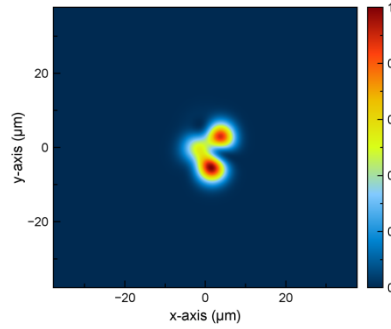


Figure 4.3: Numerically obtained output beam profile.

4.3 Experimental results and discussion

Encouraged by the simulations, experiments were performed with the numerically designed cavity parameters. The gain section of the oscillator is 1.5 m Yb MMF (nLight Yb-1200-10/125) pumped with a 976 nm pump diode coupled to the cavity with a pump combiner with matching passive fiber ports. The gain section is followed by a GRIN MMF based coupler with a 30% output coupling ratio. The modelocking mechanism is achieved by nonlinear polarization evolution (NPE) with a polarization-sensitive inline isolator with 10 μm core diameter fiber and fiber polarization controllers. After the isolator and before the MPC, a 25 cm GRIN MMF with 50 μm core diameter is placed to achieve MMI bandpass filtering with 8 nm bandwidth. The experimental oscillator is shown in Figure 4.4 a.

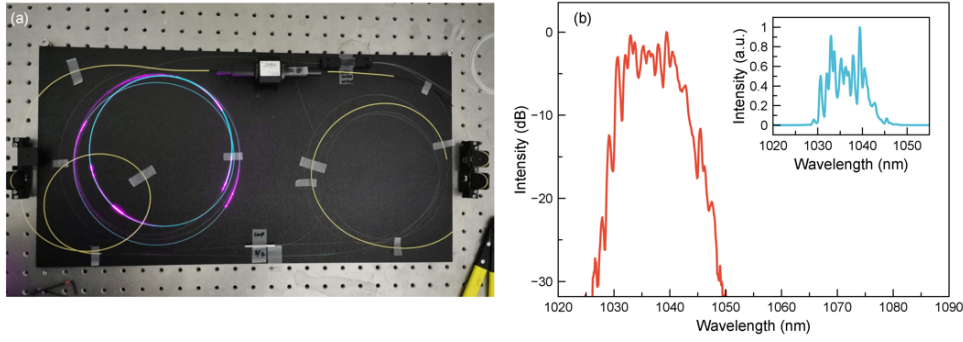


Figure 4.4: (a) Experimental setup of the all-fiber spatiotemporally mode-locked laser with multimode fiber-based filtering. (b) Measured mode-locked spectrum in logarithmic scale. Inset: Measured mode-locked spectrum in linear scale.

Spatiotemporal mode-locking is achieved easily by adjusting the intracavity polarization with the fiber polarization controllers for 2.75 W pump power. The recorded spectra from the output coupler are presented in Figure 4.4 b with spectral 10 nm spectral width at 1036 nm central wavelength. The presented spectrum is measured with a 0.5 nm resolution and features a jagged profile. Similar behavior is reported for spatiotemporally mode-locked lasers and lasers with MMI segments. The reason for the jagged spectrum can be related to the aforementioned operation type and filtering. The self-starting mode-locking operation of a single-pulse train with 24.29 MHz is presented in Figure 4.5 a. The output power of the laser is measured as 12 mW which corresponds to ~ 0.5 nJ pulse energy. The temporal characterizations are performed with second-order nonlinear autocorrelation. The laser produces chirped pulses with 6.24 ps pulse duration (see Figure 4.5 b).

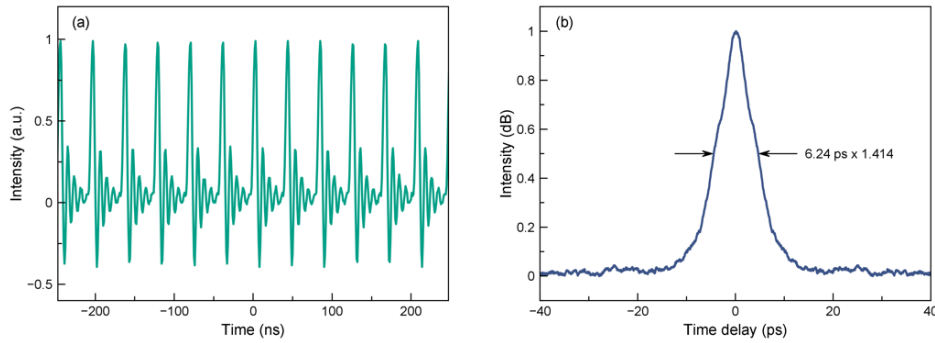


Figure 4.5: (a) Measured single-pulse train of the spatiotemporally mode-locked laser. (b) Autocorrelation trace of the chirped pulse obtained from 50 cm GRIN MMF of output coupler.

It is important to consider the effect of the fiber length and diameter of the output coupler to laser output properties. The pulses propagate through 50 cm GRIN MMF with 50 μ m core diameter after leaving the oscillator. This output fiber causes highly multimode propagation with 0.5 nJ pulses and as presented in Figure 4.6 a, the near field measurement of the output beam profile is speckled. In addition to its spatial effect, such a multimode propagation can cause temporal changes as well. Numerical simulations suggest an output pulse duration ~ 4 ps but experimental measurements indicated around 6 ps pulse duration which is larger. This 2 ps difference can be

the result of the highly multimode propagation caused by the output coupler in addition to the differences caused by the simplified numerical model. The oscillator is also characterized in the frequency domain with a radio frequency for stability purposes. The fundamental repetition rate of the laser is verified with a radio frequency (RF) analyzer (HP 3585A) as 24.29 MHz. With 1 kHz span and 10 Hz resolution bandwidth, a sideband suppression ratio around 70 dB is measured (Figure 4.6 b). The fiber laser has outstanding stability both in the short and long term. The laser continues the mode-locking operation uninterrupted for months, without a sign of degradation.

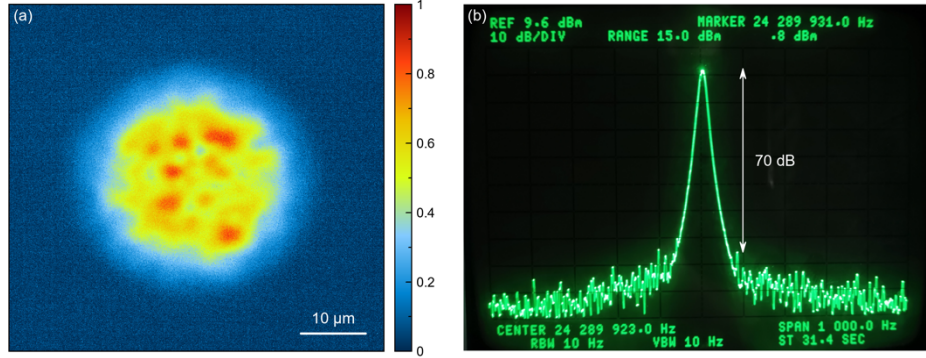


Figure 4.6: (a) Measured near-field beam profile from 50 cm GRIN MMF of output coupler. (b) Measured radio frequency spectrum with 1 kHz span and 10 Hz resolution bandwidth.

4.4 Conclusion

In conclusion, we numerically and experimentally demonstrate an all-fiber spatiotemporally mode-locked laser with multimode fiber interference-based filtering. The Ytterbium-based all-normal dispersion multimode oscillator generates 6.24 ps pulses with 0.5 nJ pulse energy, 12 mW average power and 24.3 MHz repetition rate. Compared to Ytterbium-based single-mode mode-locked lasers with multimode interference-based filtering, the reported spatiotemporally mode-locked laser produces ~4 times more powerful pulses. The all-fiber cavity design provides high stability due to the inherent alignment-free construction. We believe the proposed cavity presents an alternative approach to achieve spatiotemporal mode-locking with a simple, all-fiber design that can be used when a clean Gaussian beam is not required such as speckle interferometry and structured illumination applications.

Chapter 5 Controlling spatiotemporal nonlinearities in multimode fibers with deep neural networks

This chapter is the postprint version of the following article published in *APL Photonics*.

Controlling spatiotemporal nonlinearities in multimode fibers with deep neural networks

Uğur Teğın^{1,2}, Babak Rahmani¹, Eirini Kakkava², Navid Borhani², Christophe Moser¹, Demetri Psaltis²

¹Laboratory of Applied Photonics Devices, École Polytechnique Fédérale de Lausanne, Lausanne, 1015, Switzerland

²Optics Laboratory, École Polytechnique Fédérale de Lausanne, Lausanne, 1015, Switzerland

APL Photonics 5, 030804 (2020)

<https://doi.org/10.1063/1.5138131>

Spatiotemporal nonlinear interactions in multimode fibers are of interest for beam shaping and frequency conversion by exploiting the nonlinear interaction of different pump modes from quasi-continuous wave to ultrashort pulses centered around visible to infrared pump wavelengths. The nonlinear effects in multi-mode fibers depend strongly on the excitation condition, however relatively little work has been reported on this subject. Here, we present a machine learning approach to learn and control nonlinear frequency conversion inside multimode fibers. We experimentally show that the spectrum of the light at the output of the fiber can be tailored by a trained deep neural network. The network was trained with experimental data to learn the relation between the input spatial beam profile of the pump pulse and the spectrum of the light at the output of the multimode fiber. For a user-defined target spectrum, the network computes the spatial beam profile to be applied at the input of the fiber. The physical processes involved in the creation of new optical frequencies are cascaded stimulated Raman scattering as well as supercontinuum generation. We show experimentally that these processes are very sensitive to the spatial shape of the excitation and that a deep neural network is able to learn the relation between the spatial excitation at the input and the spectrum at its output. The method is limited to spectral shapes within the achievable nonlinear effects supported by the test setup but the demonstrated method can be implemented to learn and control other spatiotemporal nonlinear effects.

5.1 Introduction

MMFs have found applications in several fields in the last decades mainly in telecommunication and imaging [97], [98]. In recent years, spatiotemporal nonlinearities in MMFs, have also become the subject of strong interest in various fundamental and applied areas, from single-pass

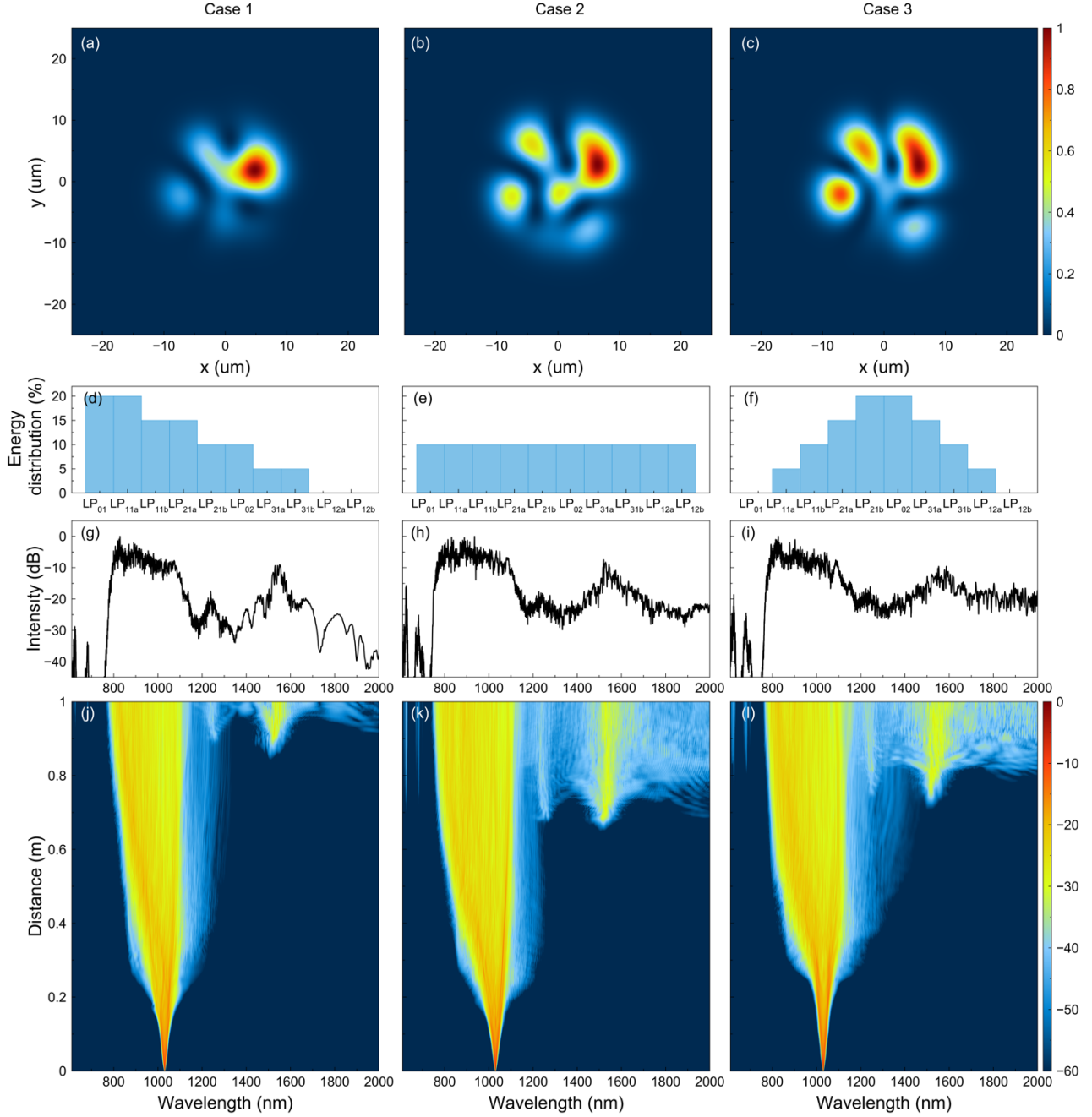


Figure 5.1: Simulation results. (a-c) Numerically obtained spectra with different excitation conditions. (d-f) Spectral evolutions through 1 m GRIN MMF.

propagation to spatiotemporally mode-locked laser cavities [42], [43], [84]. In single-pass nonlinear propagation studies, numerous interesting phenomenon [27]–[30], [32], [33], [35], [36], [38], [78] including spatiotemporal instability, self-beam cleaning and supercontinuum generation were

reported with GRIN MMFs. Although the importance of the excitation condition is mentioned, these studies were reported with only a Gaussian beam profile.

In the linear regime, the spatial control of light propagation in MMFs via wavefront shaping with a spatial light modulator is now well understood. Over the last few years, several methods including, iterative, phase conjugation and transmission matrix were successfully applied to demonstrate fluorescence confocal, two photon, Raman, CARS imaging and material processing through a MMF [99]–[101]. Recently, machine learning tools have been proposed to simplify the calibration and improve the robustness of the system in the absence of optical nonlinearities [102]. DNNs proved useful for classification/ reconstruction of the information sent to km-long MMFs solely from the intensity measurement at the output of the fibers [53], [54]. For the nonlinear propagation regime, adaptive algorithms have been brought forth and been shown to be successful in harnessing the entangled spatiotemporal nonlinearities such as Kerr beam self-cleaning of low-order modes [103] and optimization of the intensity of targeted spectral peaks generated by Raman scattering or four-wave mixing [104].

In this article, we report the results of our studies on the effect of the initial spatial excitation condition of a GRIN MMF on the output spectrum by employing machine learning. Specifically, we achieved control over multimodal nonlinear frequency conversion dynamics and demonstrated that spatiotemporal nonlinear pulse propagation can be learned by DNNs. Once trained, the DNNs can predict the spatial beam shape for the input pump pulses to produce a desired spectral shape within the limitations of the triggered nonlinear effects at the end of the GRIN MMF. In particular, we showed that cascaded stimulated Raman scattering (SRS) based broadening of the spectrum as well as supercontinuum generation, two highly nonlinear phenomena, can be experimentally controlled for the first time in the literature with machine learning tools.

5.2 Numerical Studies

Numerical calculations are performed to determine the suitable approach to define the preliminary excitation patterns applied on the GRIN MMF in the experimental studies. We numerically investigate the effect of excitation to nonlinear pulse propagation by changing the initial energy splitting ratio between the simulated modes (LP01, LP11a, LP11b, LP21a, LP21b, LP02, LP31a, LP31b, LP12a and LP12b). To investigate the nonlinear effects in 1 m GRIN MMF, pump pulses with 2 ps duration and 500 kW peak power were used in the numerical studies. The multimode nonlinear Schrödinger equation with a Raman scattering term (Equation 5.1) is numerically solved [6]. For numerical integration with high accuracy, we used a fourth-order Runge-Kutta in the Interaction Picture method [85]. We used an integration step of 5 μm and time resolution of 2.4 fs with 20 ps time window width. Although the GRIN MMF with 62.5 μm core diameter supports more than 250 modes, to reduce the computational time, we considered the 10 linearly polarized modes in our numerical studies which required 14 days of computation.

Pump pulses centered at 1030 nm with 2 ps duration and 500 kW peak power are numerically propagated for 1 m distance. In the experiment, the GRIN fiber length was 20 meters. We performed a rescaling of the propagation length from 20 m to 1 m in order to reduce the computa

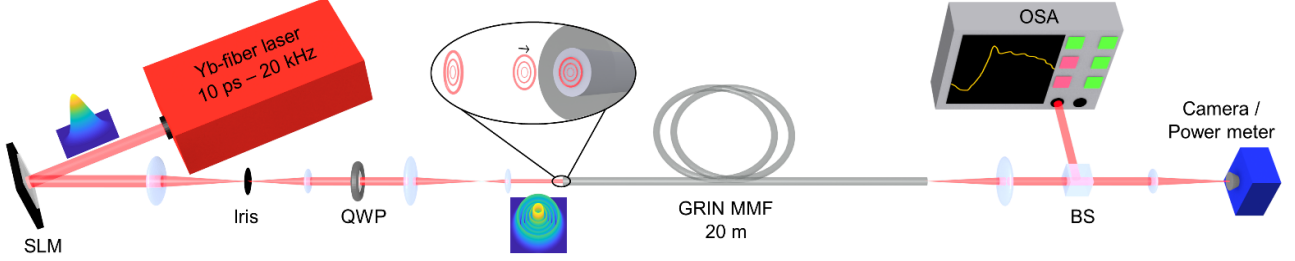


Figure 5.2: Experimental setup. SLM spatial light modulator, QWP quarter-wave plate, BS beam splitter, OSA optical spectrum analyzer.

tional time. In our simulations, we included Raman process and third-order dispersion.

$$\begin{aligned} \frac{\partial A_p}{\partial z}(z, t) = & i\delta\beta_0^{(p)}A_p - i\delta\beta_1^{(p)}\frac{\partial A_p}{\partial t} - i\frac{\beta_2}{2}\frac{\partial^2 A_p}{\partial t^2} + \frac{\beta_3}{6}\frac{\partial^3 A_p}{\partial t^3} \\ & + i\gamma \sum_{l,m,n} \eta_{plmn} \left[(1 - f_R)A_l A_m A_n^* + f_R A_l \int h_R A_m(z, t - \tau) A_n^*(z, t - \tau) d\tau \right] \end{aligned} \quad (5.1)$$

Here η_{plmn} is the nonlinear coupling coefficient, f_R is the fractional contribution of the Raman effect, h_R is the delayed Raman response function and $\delta\beta_0^{(p)}$ ($\delta\beta_1^{(p)}$) is the difference between first (second) Taylor expansion coefficient of the propagation constant for corresponding and the fundamental mode. Relative index difference between to fiber core and clad is assumed to be 0.01. Figure 5.1 demonstrates the variations in the nonlinear pulse propagation with the different initial excitation condition. As it is shown in Figure 5.1 (a), spectral broadening can be achieved by favoring the lower order modes (LP01, LP11a and LP11b). For the same pump pulse parameters, equal excitation of all the modes interestingly resulted in broader spectra (see Figure 5.1 (b)). Since more energy couples to higher order modes spectral formations around 1.5 μm occurs in a shorter propagation distance. When most of the energy was coupled to higher-order modes, the optical spectrum evolved to a smoother supercontinuum formation as presented in Figure 5.1 (c).

Our simulations revealed significant spectral differences entirely due to the initial power distribution between the fiber modes. Similar behavior was numerically reported in the literature for multimode holey fibers [105]. The propagation differences observed in Figure 5.1 can be understood by studying the nonlinear coupling term used in the numerical calculations. According to the nonlinear coupling between the modes determined by the overlap integrals, some of the intermodal processes are favored by different modal symmetry classes and particular modes act as a pump for these nonlinear effects. In our calculations, we found that by initially favoring high order modes in spatiotemporal nonlinear propagation, a medium to generate broad output spectrum can be achieved since excitation of the higher-order modes creates an environment which encourages the nonlinear intermodal interactions. In the literature, the importance of the beam size

on the fiber facet to initiate multimode propagation is emphasized in experimental studies related with self-beam cleaning and spatiotemporal instability [30], [33].

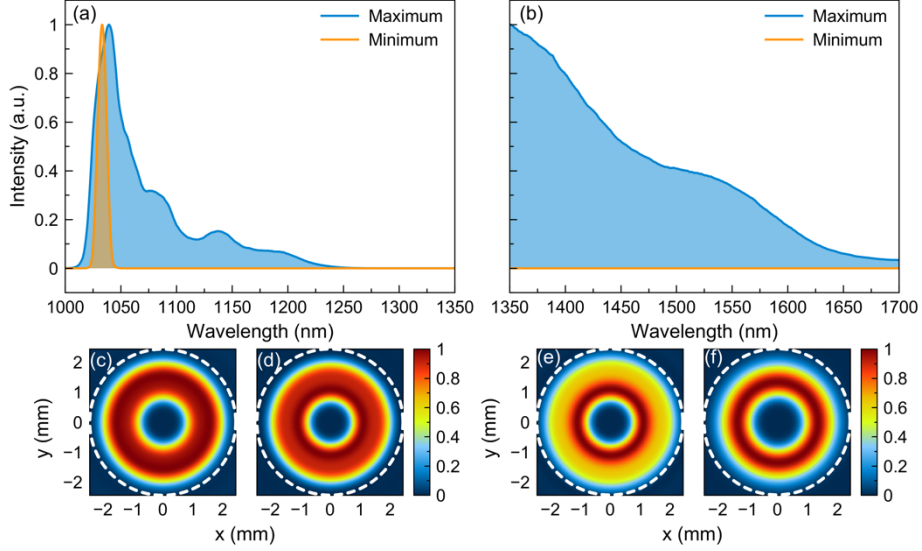


Figure 5.3: Difference in output spectra measured in the datasets. Maximum and minimum frequency conversion measured for 3000 different excitation conditions for 85 kW peak power (a) and for 150 kW peak power (b). Beam shapes applied to generate minimum and maximum frequency conversion for 85 kW (c-d) and 150 kW (e-f) peak powers. Dashed circles indicate the fiber core size on SLM.

5.3 Results

5.3.1 Experimental setup and dataset collection

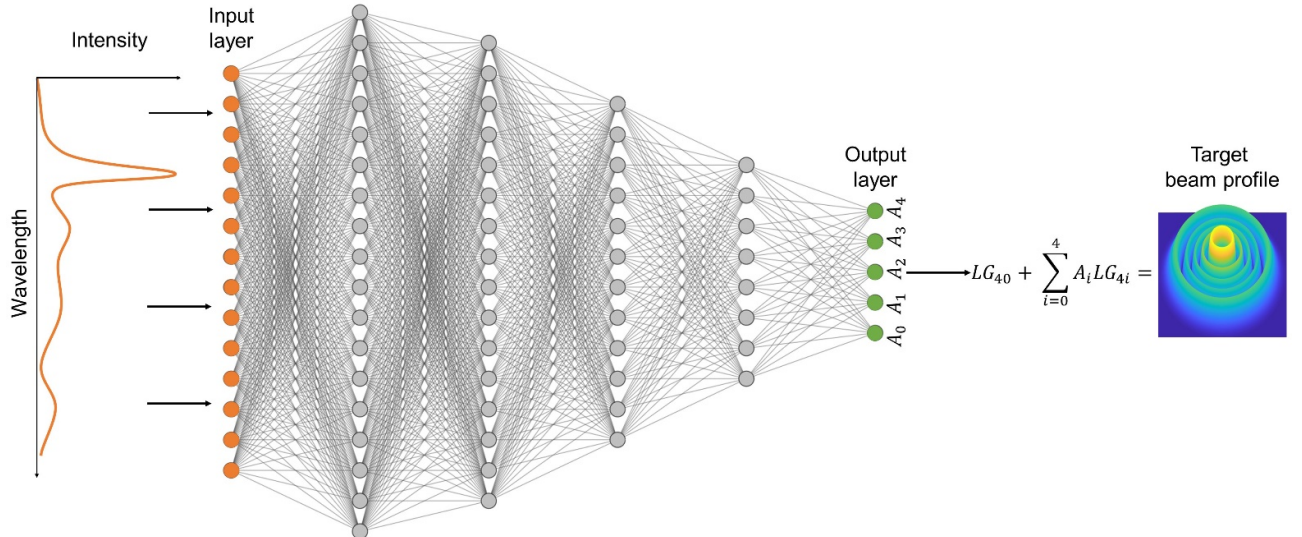


Figure 5.4: Schematic of the learning spatiotemporal nonlinear pulse propagation. Each input spectrum is linked via the proposed neural network to its corresponding coefficients at the output of the network which in turn is used to generate the required beam profile corresponding to the input spectrum.

The experimental setup is shown in Figure 5.2. We launched 10 ps pulses centered around 1030 nm with adjustable peak power into a 20 m GRIN MMF with 62.5 μm core diameter and 0.275 NA

(Thorlabs – GIF625). The fiber is coiled with 25 cm diameter and rests on the optical table without additional cooling. A phase-only spatial light modulator (SLM), 8f imaging system and a quarter-wave plate is placed before the GRIN MMF. Here, we study two particular phenomena by adjusting the peak power of the pump pulses to either 85 kW or 150 kW. In the first case, spectral broadening induced by cascaded SRS is observed while in the second case supercontinuum generation was recorded at the output of the GRIN. Cascaded SRS based spectral broadening in GRIN MMFs has been extensively studied in the past and spatiotemporal pulse propagation is the leading mechanism for the cascaded Raman Stokes generation. In GRIN MMFs, Raman Stokes peaks are reported with different beam shapes which lead to different propagation paths for each Raman peak. By compensating the chromatic dispersion difference, the multimode propagation enhances the cross-phase modulation between the Raman peaks, hence triggering the generation of a supercontinuum formation for higher peak powers after reaching to the zero-dispersion wavelength (ZDW) [27], [38].

To experimentally study the effect of the spatial profile of the excitation condition on the nonlinear pulse propagation, a set of beam profiles containing 3000 samples are calculated by superposing pre-defined base patterns with random non-repeating amplitudes from 0 to 1 and fixed sum for each candidate beam shape. Guided by simulations, a mixture of the 5 lowest order LG4X modes are selected as the base patterns to create beam profiles of the pump pulses. To minimize the power level changes due to beam shaping, the number of coefficients is intentionally limited as 5 and the LG40 mode is added to each calculated beam shape as a background. Here we would like to emphasize that the selected LG modes are calculated for the free-space propagation and the energy distribution of these patterns cannot be directly related to the energy distribution of the modes supported by the fibers. The complex amplitude modulation method described in [106] is applied to calculate the required phase patterns to generate the designed beam profiles with the phase-only SLM. The achieved beam profiles are $\sim 80X$ demagnified with the imaging system to excite GRIN MMF.

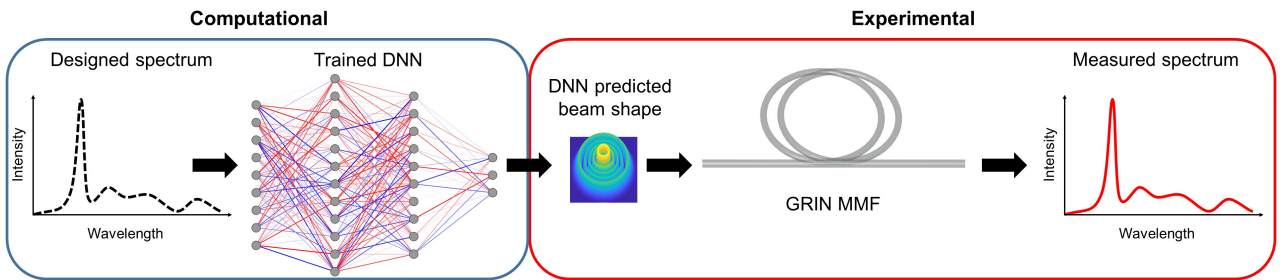


Figure 5.5: Schematic of the control experiments. To experimentally generate the computationally designed spectra, trained DNNs are used to estimate the required beam shape of the pump pulses.

Pulses with 85 kW and 150 kW peak powers and different beam shapes impinge on the GRIN MMF facet while the output spectra are being recorded for each applied pattern. For both cases of interest, strong variations at the output spectra are observed. For 150 kW pump peak power, as the spectrum approaches ZDW, the driving nonlinear effect changes and instead of cascaded SRS,

modulation instability based spectral broadening occurs. Therefore, we focused on wavelength range above the ZDW (1350 nm to 1700 nm) [27], [38]. The extreme cases recorded in the datasets are presented in Figure 5.3.

5.3.2 Machine learning and controlling nonlinearities

For both peak power levels, the machine learning approach is employed to analyze the experimentally collected data. In both cases, the same network architecture employed is comprised of four hidden layers as demonstrated in Figure 5.4. Measured spectra are fed to the network as inputs and for each spectrum, the coefficients to generate the corresponding beam profiles are the output variables of the network. DNNs can learn the spatiotemporal nonlinear pulse propagation inside the tested GRIN MMF by adjusting their weights to learn the relation between the generated spectra and the excitation condition as described by the coefficients used to determine the input beam shape.

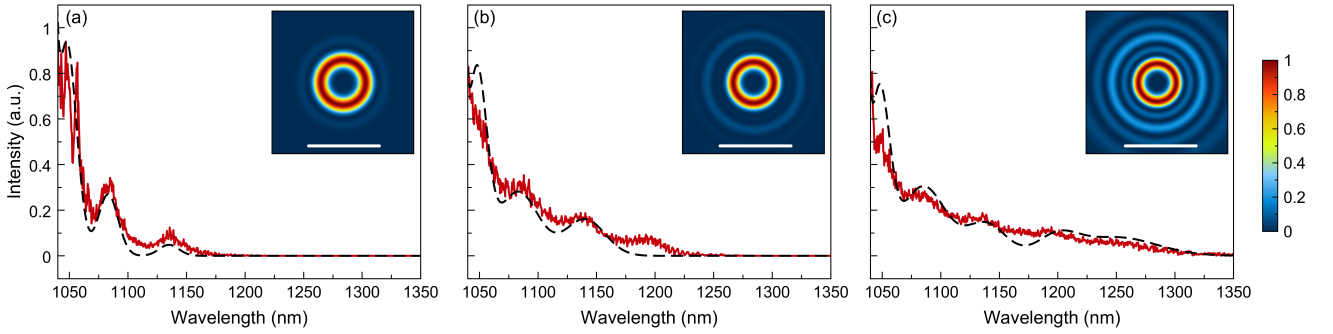


Figure 5.6: Controlling cascaded SRS generation with DNN. a-c Designed (dashed) and measured output spectra for 85 kW peak powers. The insets show DNN suggested beam shapes for pump pulses to generate designed spectra. Scale bars indicated for DNN suggested beam shapes are 3 mm.

To experimentally investigate the performance of the trained DNN, the control on the output spectra is tested with the schematic presented in Figure 5.5. For this, a collection of synthetic spectral shapes is generated via summations of Gaussian distributions with different amplitudes and widths. It should be noted that the synthetic spectra must still lie within the limits of the recorded spectral dataset. These target spectra are then fed to the DNN to predict the required beam shapes of the target pump pulses. For each designed target spectra, the DNN predicts the coefficients of the LG4x patterns and from these coefficients, the required input beam shapes are synthesized. Here, we rely on the ability of the neural network to generalize since the user-defined spectra is not from the test nor the training data set. For 85 kW pump peak power level, summations of different Gaussian functions centered around the Raman Stokes peaks of the silica medium are used to design the targeted distributions with different amplitudes and widths. These target spectra are then fed to the DNN to predict the required beam shapes of the target pump pulses. For each designed target spectra, the DNN predicts the coefficients of the LG4x patterns and from these coefficients, the required input beam shapes are synthesized. Here, we rely on the ability of the neural network to generalize since the user-defined spectra is not from the test nor the training data set. For 85 kW pump peak power level, summations of different Gaussian functions

centered around the Raman Stokes peaks of the silica medium are used to design the targeted spectra. Results of the tests for controlling cascaded SRS generation are presented in Figure 5.6. The measured spectra corresponding to the DNN-predicted beam shapes are well matched with the target spectra (Figure 5.6 a-c). For 150 kW pump peak power level, spectral shapes are designed based on the trailing edge of a Gaussian function centered around 1350 nm since the targeted wavelength range corresponds to the trailing edge of the supercontinuum spectra. The same procedure explained for 85 kW pump peak power level is applied to control the supercontinuum generation. Targeted and experimentally measured spectra are presented in Figure 5.7a-c and the experimentally measured spectra which are in good agreement with the targeted spectra. DNN predicted beam profiles of the pump pulses are shown in insets of Figure 5.7d-f.

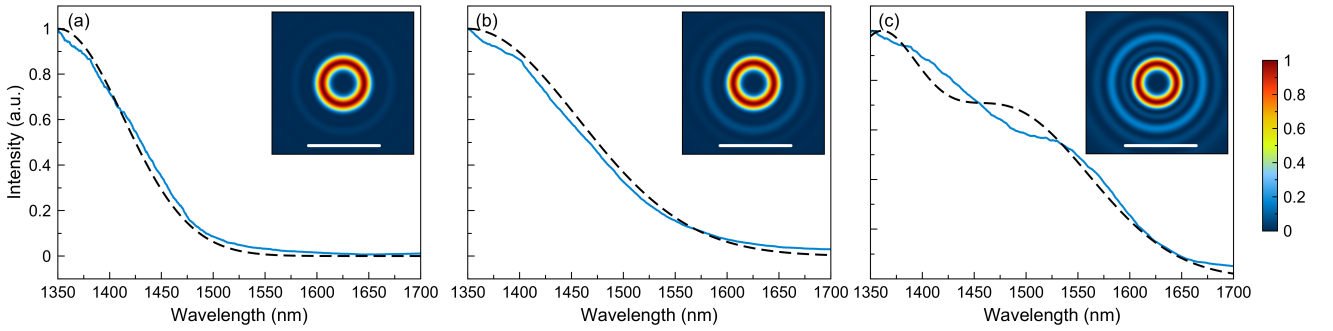


Figure 5.7: Controlling supercontinuum generation with DNN. a-c Designed (dashed) and measured output spectra for 150 kW peak powers. The insets show DNN suggested beam shapes for pump pulses to generate designed spectra. Scale bars indicated for DNN suggested beam shapes are 3 mm.

5.4 Discussion

The main result of this article is that machine learning tools can master the underlying basis of the spatiotemporal nonlinear propagation in MMFs which have been considered chaotic and complex over the years. Here DNNs are employed to learn the relation between the initial modal energy distribution of the fiber and nonlinear frequency conversion. Trained with experimental data, our DNNs are shown to be a powerful tool to harness the nonlinear dynamics of the MMF within the nonlinear dynamics defined by the system.

Due to non-one-to-one relation between the initial modal energy distribution of the fiber and nonlinear frequency conversion dynamics, the experimental controlling efficiency of the DNNs is a significant topic. For both peak power levels (85 kW and 150 kW), more than 50% efficiency is achieved in the control experiments. By introducing artificial noise to the designed spectra, the experimental estimation efficiencies of DNNs are improved and reached to 80%. We believe this improvement is due to the noisy nature of the experimentally collected dataset but it needs to be further investigated in future work. We observed that DNNs learned the behavior of initially favoring high order modes to achieve broader output spectrum, which is also presented in our numerical simulations. For both of the peak power levels, to generate targeted spectra which requires more nonlinear conversions, DNNs are increased the coefficients of the high order base patterns (Figure 5.6-inset and Figure 5.7-inset).

In conclusion, we showed that spatiotemporal nonlinear pulse propagation can be learned and controlled by machine learning tools. We demonstrated that spectral broadening based on the cascaded SRS and supercontinuum generation can be both altered by tuning the initial modal energy distribution of the fiber through shaping the beam profile of the pump pulse by implementing experimentally trained DNNs. The machine learning approach reported here can be employed to understand and tune other nonlinear effects and relations. Our results present a novel path toward automated tunable fiber-based broadband sources.

Chapter 6 Predicting spatiotemporal nonlinear dynamics in multimode fibre optics with a recurrent neural network

This chapter is the postprint version of the following invited reusability report published in *Nature Machine Intelligence*.

Predicting spatiotemporal nonlinear dynamics in multimode fibre optics with a recurrent neural network

Uğur Teğın^{1,2}, Niyazi Ulaş Dinç^{1,2}, Christophe Moser², Demetri Psaltis¹

¹*Optics Laboratory, École Polytechnique Fédérale de Lausanne, Lausanne, 1015, Switzerland*

²*Laboratory of Applied Photonics Devices, École Polytechnique Fédérale de Lausanne, Lausanne, 1015, Switzerland*

Nature Machine Intelligence (2021)

<https://doi.org/10.1038/s42256-021-00347-6>

With their internal memory, recurrent neural networks can be utilized to learn and predict time-dependent behaviours. In their recent work, Salmela et al. [55] present a recurrent neural network architecture to learn and predict complex nonlinear propagation in an optical fibre based on the input pulse intensity profile in the time domain. Here, we use their model by extending it to the case of spatiotemporal nonlinear propagation for an arbitrary number of modes in graded-index multimode fibres. In addition to the original work's focus on predicting the temporal evolution of pulses, we show that the method is applicable for modelling and predicting spatial beam propagation incorporating nonlinear mode coupling.

The demonstrated method of Salmela et al. [55] can be an alternative solution to time consuming and computationally heavy nonlinear pulse propagation simulations. In essence, the method can accurately reproduce the complex nonlinear evolution governed by NLSE via employing long short-term memory (LSTM) nodes in an artificial neural network. Such a network architecture is capable of modelling sequential dependencies. Salmela et al. [55] tested their model for pulse compression and ultra-broadband supercontinuum generation. They were able to accurately predict tem-

poral and spectral evolutions of ultrashort pulses in a highly nonlinear fibre. Using the same neural network architecture, we trained the network to predict the spatiotemporal evolution of ultrashort pulses. In this study, we hypothesized that their recurrent neural network might be suitable to predict the spatiotemporal field evolution given that it successfully predicted the temporal physical dynamics that is governed by the same NLSE equation that describes the spatial domain as well. Since the NLSE is also applicable to other physical systems, it may be possible that a generic, normalized form could be utilized for example in Bose-Einstein condensation, hydrodynamics and plasma physics [107].

6.1 Spatiotemporal nonlinearities and simulations

The study in [55] focuses on single mode fibre with spectral or temporal nonlinear evolution of pulses in propagation axis by computing (1 spatial coordinate +1 time coordinate)D simulations. Further, the authors show promising results by applying their method to a step-index multimode fibre by computing the propagation of 5 modes of the investigated fibre by following a similar (1+1)D simulation and incorporating mode coupling by a matrix product calculated as the overlap integrals of the modes of interest. In this study, we change the media from step-index to graded-index multimode fibre and compute (3 spatial coordinates +1 time coordinate)D simulations where the interaction of all the available modes of the fibre fuses naturally since all the contributing spatiotemporal degrees of freedom in the NLSE are included.

With relatively low modal dispersion and periodic self-imaging, graded-index multimode fibres have become the subject of significant interest for nonlinear optics, imaging and telecommunications studies. In recent years, various interesting nonlinear dynamics such as spatiotemporal instability [28], [30], dispersive wave generation [31], graded-index solitons [78], [79], self-beam cleaning [33], nonlinear pulse compression [80], and supercontinuum generation [36], [38] are reported. In addition to aforementioned single-pass dynamics, spatiotemporal mode-locked lasers [42], [84], [95] have been realized thanks to the low modal dispersion pulse propagation in graded-index multimode fibres. With an SLM, learning and controlling nonlinear optical dynamics in graded-index multimode fibres was demonstrated by modifying the spatial properties of the intense pump pulse [104], [108]. Recently, spatiotemporal nonlinear interactions in a graded-index multimode fibre were introduced as an optical computing engine which performed well on a range of machine learning tasks from classifying COVID-19 X-ray lung images and speech recognition to predicting age from face images [109].

Numerical analysis is required to understand the underlying complex spatiotemporal dynamics of pulse propagation in a multimode fibre. The most significant challenge in multimode fibre simulations is the addition of spatial degrees of freedom. In a single-mode fibre simulation, there is only the time domain grid to establish and then propagation can be implemented, for instance, using split-step Fourier simulations, which has a low computational cost since 1D Fourier transforms are computed in every step. In multimode fibre, there are multiple propagating modes that have different spatial distributions. Hence, transverse dimensions must be included to describe a pulse

which requires a sampling grid in two dimensions X and Y in addition to time. Hence, 3D Fourier transforms (two spatial dimensions in transverse plane and one dimension in time) must be computed at every step taken along the propagation direction Z to provide a (3+1)D simulation. This is computationally costly and time-consuming. To overcome the computational load of (3+1)D beam propagation simulations, mode-resolved simulation methods based on pre-calculated nonlinear mode coupling were proposed in the literature [6], [105]. However, mode-resolved simulations are time efficient for <10 modes and a low number of modes may not give an accurate picture of the spatiotemporal nonlinear propagation in a >200 mode fibre. In this regard, the work by Salmela et al. [55] enables a faster computation scheme when the neural network is trained [56].

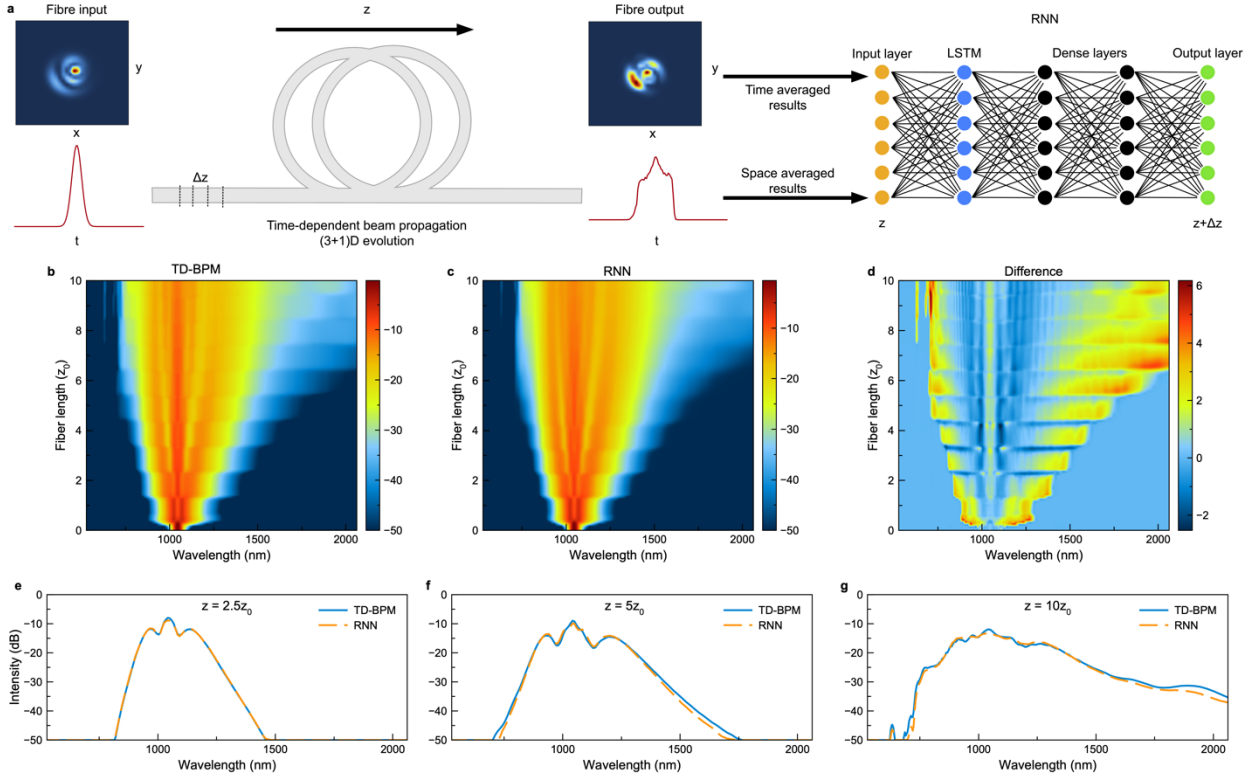


Figure 6.1: An example of the spectral intensity evolution of a high-power femtosecond pulse in a graded-index multimode fibre. a Schematic of data generation and training pipeline. b Time-dependent beam propagation (ground truth). c Recurrent neural network predicted pulse propagation. d Difference between the ground truth and the prediction. e-g Time-dependent beam propagation simulation results and the recurrent neural network predicted results at different propagation lengths. The recurrent neural network predictions use only the injected pulse intensity profile as input. The colour bars show intensity in decibels [dB] and z_0 is the self-imaging period of the fibre.

In our study, we first tested the neural network presented in [55] by generating a data set using a numerically computed fibre output using the (3+1)D split-step Fourier method that considers the interaction of all available fibre modes. We call this method Time Dependent-Beam Propagation Method (TD-BPM). We implemented a GPU parallelized TD-BPM in Python to generate the dataset. To remain loyal to the original approach, we integrated the intensity of the TD-BPM outputs in the spatial domain to obtain the time-domain evolution only. The performance of the network in the time domain (but with spatial integrated modes) is illustrated in the “Temporal results” sec-

tion. The “Spatial results” section shows the performance of the network to predict the intensity profile along the propagation from the time integrated data. Due to the network architecture, the data is fed after a dimension reduction by time-averaging or space-averaging. Never-the-less, the spatiotemporal effects are still inherited in the reduced data where each RNN model is capable to capture it.

6.2 Results

6.2.1 Temporal results

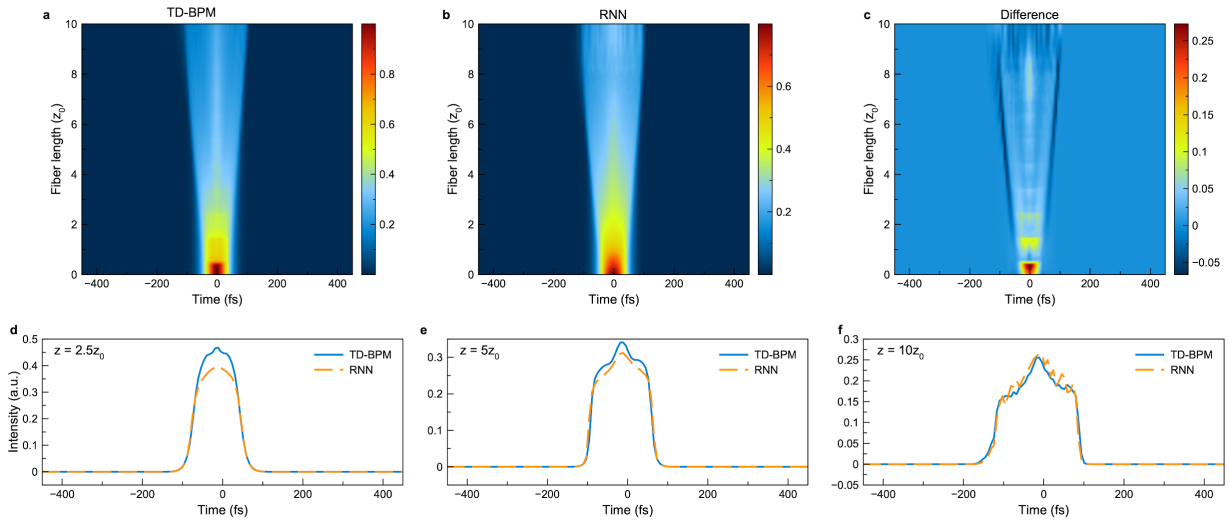


Figure 6.2: An example of temporal intensity evolution of a high-power fs pulse in a graded-index multimode fibre. a Time-dependent beam propagation (ground truth). b Recurrent neural network predicted pulse propagation. c Difference between the ground truth and the prediction. d-f Time-dependent beam propagation simulation results and the recurrent neural network predicted results at different propagation lengths. The recurrent neural network predictions use only the injected pulse intensity profile as input. The colour bars show intensity in linear scale, which is normalized over the whole dataset. z_0 is the self-imaging period of the fibre.

The datasets generated by the aforementioned TD-BPM contain 1000 examples of spatiotemporal nonlinear propagation of femtosecond pulses (see Supplementary Discussion 1 for details <https://dx.doi.org/10.1038/s42256-021-00347-6>). Following the original work and using the sample code, with a small modification to increase the number of nodes in each layer from 250 to 500, we trained and tested spectral and temporal nonlinear propagation in a graded-index multimode fibre. Each dataset is split into 950 propagation samples for training and 50 propagation samples for testing. During the training, at each epoch, training data is split randomly with 9 to 1 ratio to generate the validation set, which is repeated for every training process in this study. The TD-BPM generated data is first converted to logarithmic scale and normalized. The evolutions of the mean absolute error metric for training the networks are presented in Supplementary Discussion 4 <https://dx.doi.org/10.1038/s42256-021-00347-6>.

Similar to the work by Salmela, et.al [55], we tested the recurrent neural network for stepwise (only predicting selected next steps) and complete propagation (feeding the predicted steps to calculate the next step) predictions in the frequency and time domain but in a multimode fibre. The best performance of the neural network is observed for stepwise predictions. The stepwise performances of the network for spectral and temporal data are presented in Supplementary Figure 1 and Figure 2 <https://dx.doi.org/10.1038/s42256-021-00347-6>. For the complete propagation predictions by only using the injected pulse profile leads to accumulated errors but as it is presented in Figure 6.1 and Figure 6.2, the difference between the TD-BPM (ground truth) and the predictions are small and in an acceptable range.

6.2.2 Spatial results

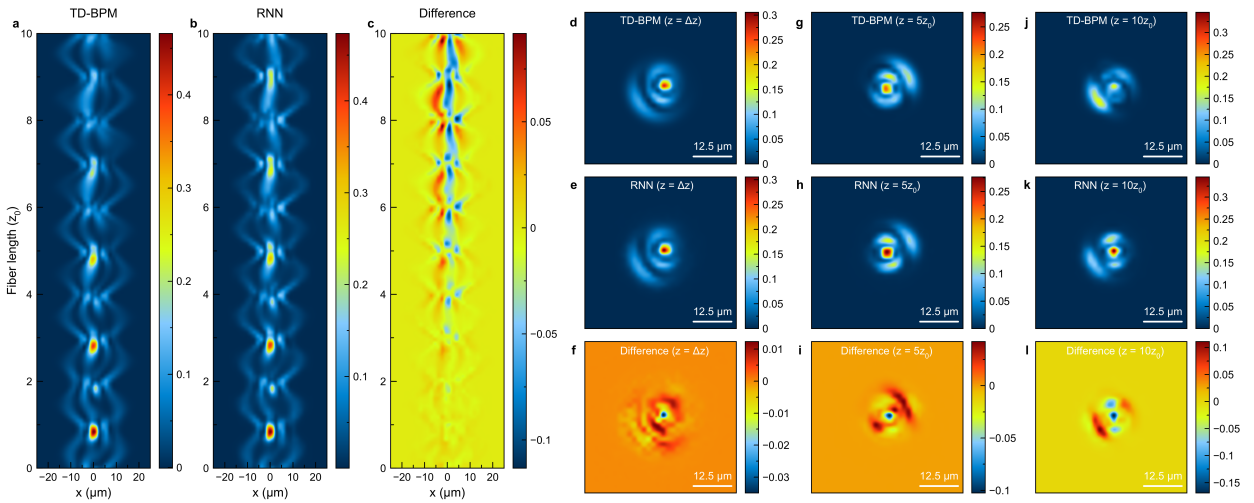


Figure 6.3: An example spatial intensity evolution of a 1GW fs pulse in a graded-index multimode fibre. a Time-dependent beam propagation (ground truth) in XZ mid-plane. b Recurrent neural network prediction of pulse propagation in XZ mid-plane. c Difference between the ground truth and the prediction of the propagation profiles. d-f The time-dependent beam propagation simulation result and the recurrent neural network prediction result after the first z-step in the transverse plane (XY) and the relative difference respectively. g-i Similar plots given in d-f at the half fibre length. j-l Similar plots given in d-f at the output plane (last propagation step). The recurrent neural network predictions use only the injected pulse intensity profile from the test data as input. The colour bars show intensity in linear scale, which is normalized over the whole dataset. All the fields are up sampled for better visualization and z_0 is the self-imaging period of the fibre.

The dataset is generated by integrating the outputs of TD-BPM in the time-domain to generate spatial-domain only intensity distributions. A graded-index fibre with 50 μm core diameter, which supports 240 modes at 1030 nm wavelength is digitally created. 1000 different propagation cases are generated by having different spatial excitations at the fibre input. LP01, LP02, LP03, LP11, LP12, and LP21 modes are superposed with random coefficients while keeping the peak power fixed at 1 GW to encourage nonlinear inter-modal coupling within a short fibre length that is chosen as 10 times the self-imaging period of the graded-index multimode fibre. Note that the field launched is limited to 6 modes however the modes can couple into the higher order modes of the

GRIN fibre (240 available modes) upon propagation due to mode coupling. The dataset is divided into training data (950 samples) and testing data (50 samples). The data is down sampled to 32 by 32 pixels in transverse x and y axis and 120 steps in the z axis. The 2D spatial information is converted to a 1D array of 1024 elements to employ the original network architecture that accepts 1D intensity profiles. The LSTM and dense layer node number is set to 1000 and window size, which is the number of previous steps introduced in LSTM, is set to 15. In Figure 6.3, the prediction of the trained network on a test data is shown with the XZ propagation profile and XY transverse profiles of the first, the middle and the last steps along with corresponding TD-BPM results that serve as the ground-truth.

6.3 Discussion

During our study, we compared the simulation runtimes between the TD-BPM and that of the recurrent neural network architecture for training and inference. The required training time for the recurrent neural network is comparable to the data generation time of the TD-BPM which is around 50 minutes for 1000 samples. On the other hand, as anticipated, the inference time of the recurrent neural network is more than 40 times faster than TD-BPM for single-pass pulse propagation with a graphics card based parallel processing on Nvidia Tesla V100 GPU.

Temporal results show that the network successfully infers the time evolution of a pulse. Since a different simulation method (TD-BPM instead of mode-resolved as used in the original work) and media (graded-index multimode fibre instead of single mode and step-index multimode fibre, used in the original work) are chosen in this study, we can state that the proposed architecture is capable of grasping the NLSE governed dynamics without relying on a certain method to generate training data. Due to the selected pulse parameters (duration and central wavelength), the dataset contains supercontinuum generation from self-phase modulation and spatiotemporal instability [28], [30]. As it is presented in the results section, the neural network can remarkably predict the separate and combined spatiotemporal instability peaks around 632 nm 768 nm.

The proposed architecture is able to predict spatial propagation decently as demonstrated in Figure 6.3. However, a significant amount of error is also present, which is higher than the obtained error in temporal-only predictions. In Supplementary Discussion 3 (<https://dx.doi.org/10.1038/s42256-021-00347-6>), we investigated a simpler spatial scenario where the input distribution is fixed as a donut shape and pulse power is varied in the order of MW to have relatively mild nonlinear interactions. This scenario yielded less mean absolute error compared to the results provided in Figure 6.3 where the spatial distribution of the input field is varied and pulse power is set to GW to have more nonlinear interactions. This comparison hints that a degradation in the performance of predictions occurs as the variations within the dataset and strength of nonlinear interaction increases. The main cause of this performance issue may arise from the intensity-only nature of the implemented neural network architecture. Physically, the field evolution is a product of the intensity and phase changes in time and space. However, in this architecture, the network is forced to learn the nonlinear propagation of a complex field with-

out the phase information. Even so, the network mimics the overall propagation trend, which is quite an achievement given the fact that half of the information required is not provided. The reason of this promising achievement lies in the dataset where the complex field evolution is generated by including the effects of all the dimensional degrees of freedom. The dimension reduction by time-averaging and applying absolute square to convert the complex field into intensity does not completely erase the trace of the complex higher dimensional field evolution as these traces manifest their self in the intensity evolution. The verification of this point can be found in the Supplementary Discussion 5 (<https://dx.doi.org/10.1038/s42256-021-00347-6>) where the RNN is trained by phase-only varying input fields.

Another important factor is the resilience to under sampling. Considering the low resolution discretization in the inference, it is straight-forward to say that the recurrent neural network is more flexible in terms of sampling constraints. However, this advantage is a result of the training phase where the data is generated with appropriately sampled simulation frames. Then the accurate data is down sampled and provided to the network. In the case of under sampled training data that contains sudden pixel to pixel jumps, then the trained network fails to model NLSE and yields unrelated predictions for the propagation.

6.4 Future directions

There are two main directions to expand the scope of the proposed recurrent neural network architecture: introducing spatiotemporal characteristics together in the network instead of decoupling space and time information of the pulse as well as a network capable of handling complex fields. Neural network architectures that deal with complex fields are already presented such as for example the NN that decomposes the output field into LP modes [110], [111]. With a similar scheme, the network could accept transverse complex fields and the time domain information in (2+1)D fashion to perform the nonlinear evolution step by step in the propagation direction. With the augmented dimensionality, 2D and/or 3D convolutional layers could replace the fully connected layers before and after the LSTM as light propagation is governed by convolution with a diffraction kernel.

Chapter 7 Scalable Optical Learning Operator

This chapter is the edited version of the following article available in *arXiv* (accepted by Nature Computational Science).

Scalable optical learning operator

Uğur Teğın^{1,2}, Mustafa Yıldırım², İlker Oğuz^{1,2}, Christophe Moser², Demetri Psaltis¹

¹*Optics Laboratory, École Polytechnique Fédérale de Lausanne, Lausanne, 1015, Switzerland*

²*Laboratory of Applied Photonics Devices, École Polytechnique Fédérale de Lausanne, Lausanne, 1015, Switzerland*

arXiv preprint (2020)

arXiv:2012.12404

Today's heavy machine learning tasks are fueled by large datasets. Computing is performed with power hungry processors whose performance is ultimately limited by the data transfer to and from memory. Optics is one of the powerful means of communicating and processing information and there is intense current interest in optical information processing for realizing high-speed computations. Here we present and experimentally demonstrate an optical computing framework (Scalable Optical Learning Operator) based on spatiotemporal effects in multimode fibers for a range of learning tasks from classifying COVID-19 X-ray lung images and speech recognition to predicting age from face images. The presented framework overcomes the energy scaling problem of existing systems without compromising speed. We leveraged simultaneous, linear, and nonlinear interaction of spatial modes as a computation engine. We numerically and experimentally showed the ability of the method to execute several different tasks with accuracy comparable to a digital implementation. Our results indicate that a powerful supercomputer would be required to duplicate the performance of the multimode fiber-based computer.

7.1 Introduction

Early optical computers were used to calculate linear operations such as the Fourier transform and correlations. They found applications in pattern recognition and synthetic aperture radar [112],

[113]. However, with the advent of modern VLSI technology and efficient algorithms (e.g Fast Fourier Transform), digital signal processing based on silicon circuits became so fast and parallel that the analog optical computation that included the input and output electronic overhead became obsolete. Digital optical computing, that combined nonlinear optical switches [114] with linear optical interconnections [115] replacing wires, was then intensely pursued in the 1980's. Optical interconnections can be advantageous in terms of power consumption [116], however in an all-optical implementation this advantage is counter-balanced by the power inefficiency and large size of optical switches compared to the electronic ones. Therefore, all-optical digital computers are not yet competitive. Optics has also been used for the implementation of nonlinear computations that are not based on Boolean logic, such as the optical implementation of neural networks [60], [117]. In principle, the dense connectivity of neural networks and their relative robustness against noise and device imperfections, renders neural networks a promising area for optical computing.

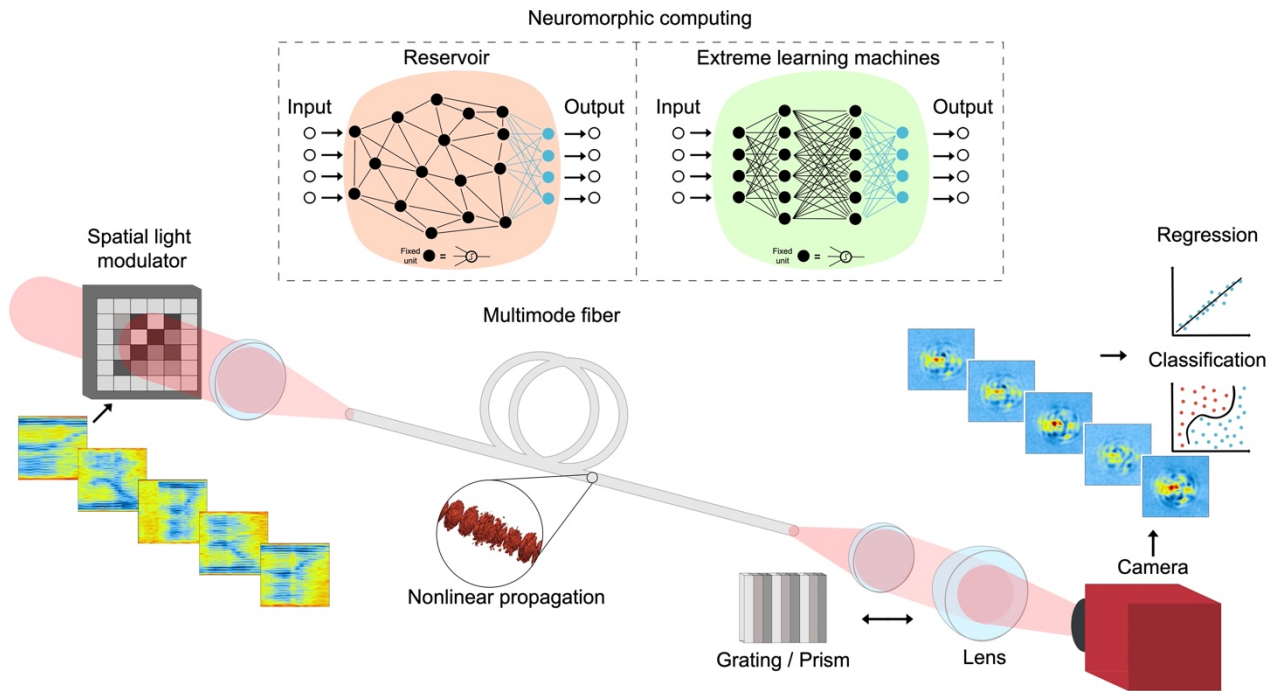


Figure 7.1: Illustration of the fixed-parameter neural network architectures and the experimental setup for nonlinear projection with spatiotemporal multimode fiber nonlinearities. The inset depicts neural network architectures with similar attributes as the MMF processor with black and blue connections indicating fixed and adaptable weights, respectively.

Interest in optically implemented neural networks has intensified in recent years partially because the large size of databases that need to be managed stresses the capabilities of existing digital, electronic computers. Several promising approaches are being investigated and they are summarized in a recent review article [71]. The key challenge in designing a viable optical computer (including a neural one) is to combine the linear part of the system from where the competitive edge of optics derives, with nonlinear elements and input-output interfaces while maintaining the speed and power efficiency of the optical interconnections. The prospect of an optical engine for

computation is as a computational accelerator working alongside CPUs and GPUs, which may be placed physically close to the edge of the communication network in order to minimize data transfer and perform the computation which would otherwise be carried out in a server farm.

The solution we propose and demonstrate in this paper is the combination of the linear and non-linear parts of the optical system in a shared volume confined in a MMF. The principal advantage of this approach is the combination of the 3D connectivity of optics with the long interaction length and lateral confinement afforded by the fiber which makes it possible to realize optical nonlinearities at relatively low power. At the same time, the large number of spatial modes that can be densely supported in a MMF maintains the traditional high parallelism feature of optics, while maintaining a compact form factor. Finally, with the availability of megapixel SLMs and cameras, the 2D input and output interfaces to the MMF can sustain a large information processing throughput. We refer to the proposed method as SOLO (Scalable Optical Learning Operator) in the remainder of this paper.

A schematic diagram of the MMF processing element is shown in Figure 7.1. The data to be processed is entered through the 2D spatial light modulator on the left. At sufficiently high illumination peak power, the light from a pulsed light source is nonlinearly transformed as it propagates through the fiber and the result of the computation is projected on the 2D camera. Given the properties of the fiber and the laser source, the input-output operation performed by the MMF is fixed and highly nonlinear. We implement a reconfigurable processor by combining the fixed nonlinear MMF mapping in the optical domain with a single layer digital neural network (decision layer) trained to recognize the output recorded on the camera using a large data set of input-output pairs. For instance, we used this system to diagnose with high accuracy (83.2%) COVID-19 from X-ray images of lungs compared to other studies. We used a large database of X-ray images of lungs with COVID-19 to train the single layer network that classifies the representation of the lungs that is produced at the output camera. The notion of combining a complex, fixed mapping with a simpler programmable processor to realize a powerful overall system, including the optical implementation of such machines, has been used in support vector machines [118], [119] reservoir computing [62], [63], [120], [121], random mappings [66], [68], [69], [122], and extreme learning machines [64], [123]. The nonlinear mapping performed by the MMF is not the same as in any of the earlier approaches. As we will show, it proves to be very effective in transforming the input data space on the SLM to a nearly linearly separable output data space (camera at end of the MM fiber) at very high speed and power efficiency.

In the remainder of the paper, we present numerical and experimental results from our optical computing framework for single variable linear regression, multivariable linear regression, age prediction from face images, audio speech classification and COVID-19 diagnosis from X-ray images tasks. We then discuss how the system scales to large data size and estimate the power consumption per operation. These studies show that the analog optical computer based on the MMF is power efficient, versatile and obtains accuracy performance comparable to that obtained with digital computers when solving the tasks we investigated.

7.2 Results

7.2.1 Experimental results

MMFs exhibit waveguide properties while allowing a large number of spatial degrees of freedom. GRIN MMFs in particular, have become the subject of significant interest for telecommunications, imaging and nonlinear optics studies due to their unique properties such as relatively low modal dispersion and periodic self-imaging. In recent years, with spatiotemporal pulse propagation in GRIN MMFs, various nonlinear frequency generation dynamics [28], [30], [31], [36], [38], nonlinear beam cleaning [33] and spatiotemporal mode-locking [42], [84], [95] have been realized. Moreover, learning and controlling nonlinear optical dynamics in GRIN MMFs was demonstrated by modifying the spatial properties of the intense pump pulse with a SLM or deformable mirror device [104], [108].

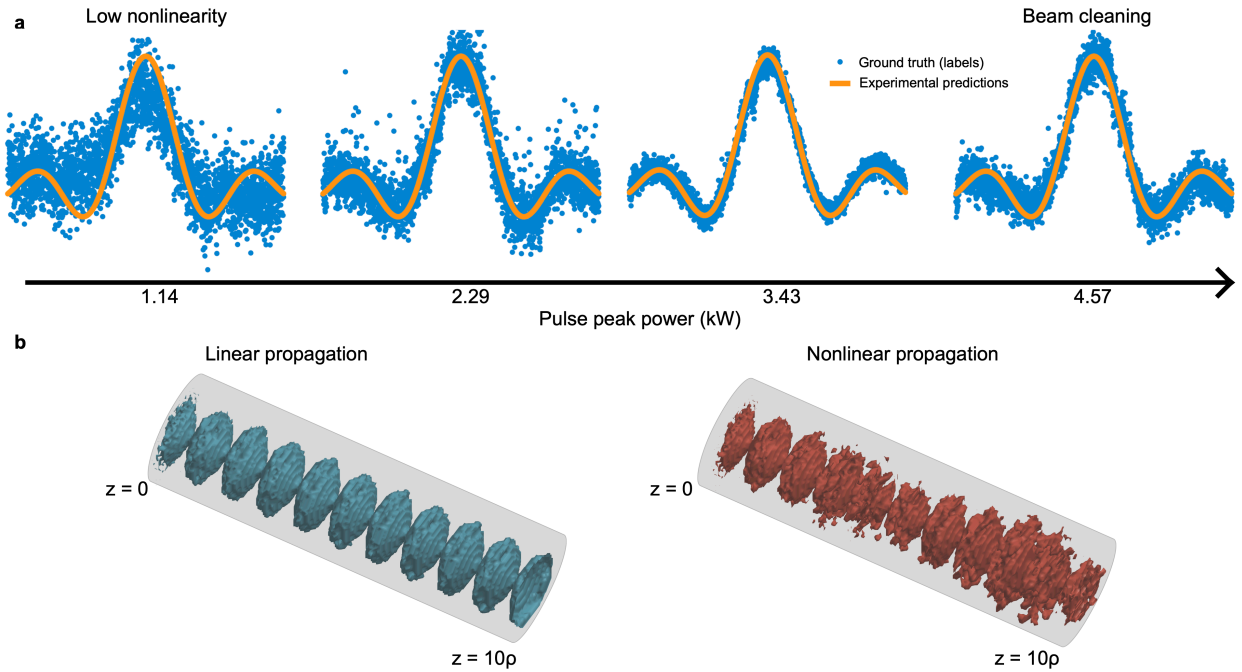


Figure 7.2: Learning a nonlinear function (sinc): dependence on the pulse propagation regimes in a graded-index multimode fiber caused by increasing the input optical peak power. (a) Experimental measurements: increasing the input peak power increases the nonlinear coupling between modes which translates in better learning. Beyond an optimal peak power, the learning performance degrades due to the Raman beam cleaning effect (see text). (b) Illustration of the propagation difference for linear (low peak power) and nonlinear (high peak power) cases in a GRIN MMF with 10 self-imaging period length.

In machine learning studies, a variety of nonlinear transformations of the input data have been investigated in order to enable learning of complex relations hidden in the data [124]. In our case, we make use of the nonlinear mapping that takes place at high light intensities when an input pattern propagates in a multimode fiber as a physical realization of machine learning. The experimental setup in Figure 7.1 is explained in detail in the Methods section. In this setup, information spatially modulated an intense laser pulse with the input data and the Fourier transform of the

spatially modulated beam was focused on the input facet of the optical fiber through a lens. The amount of light coupled to each of the modes of the fiber is given by the inner product between the incident light amplitude and the mode profile. Upon propagation, the initial complex modal coefficients evolve according to spatiotemporal linear and nonlinear effects. The nonlinear transformation of information is achieved by nonlinear energy exchange between the fiber modes. The transformed information at the end of the fiber is imaged onto a camera, and the image was downsampled such that the spatial sampling period is approximately equal to the resolution limit, which can be approximated by $\lambda/2(\text{NA})$, the Abbe diffraction limit. Each pixel of the downsampled image served as an input feature to a linear regression or equivalently, to a single layer neural classification algorithm to estimate the identity of the input on the SLM.

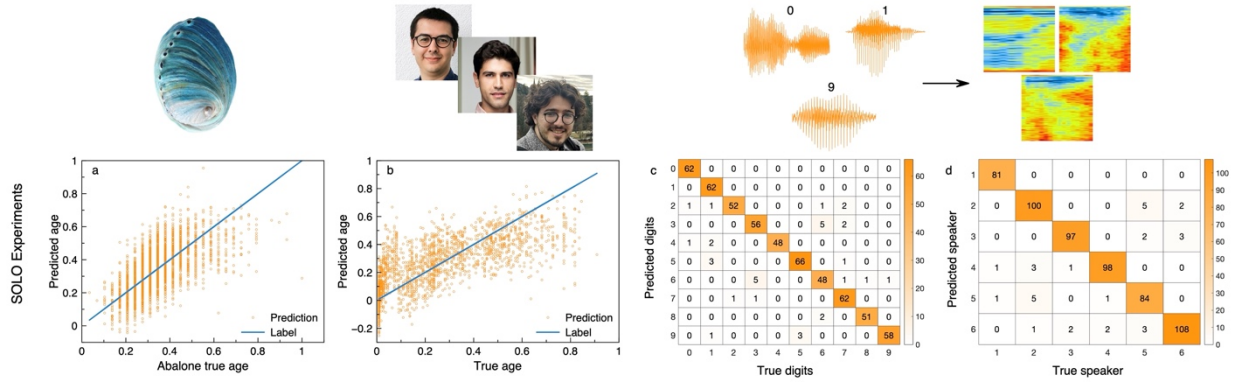


Figure 7.3: Experimental (a-d) learning results for regression and classification tasks. (a) Learning of abalone (multivariable) dataset. (b) Age prediction from face image dataset. (c) Confusion matrix for audio dataset digit classification. (d) Confusion matrix for audio dataset speaker classification.

Learning a nonlinear function

To test this, we selected a simple regression problem on a dataset generated with a nonlinear (Sinc function) relation. The input information (x) were randomly generated numbers between $-\pi$ to π and the corresponding output labels (y) were generated according to the $y = \text{Sin}(\pi x)/(\pi x)$ relation. This simple dataset is often used as a benchmark in machine learning studies since linear regression of a nonlinear function is impossible without a nonlinear transformation [64], [123]. Each input value (x) was uniquely coded as a 2D pattern which was recorded on the SLM (see Appendix A.3 for details). By recording the nonlinearly propagated beam profile of many such input values, a linear regression method was performed on the output data (see Figure 7.2 a). To measure the effectiveness of the spatiotemporal nonlinear propagation and assess the importance of the nonlinearity, we experimented with different pulse peak powers to control the level of nonlinearity. For low peak power (~ 1.14 kW), the nonlinearity is relatively weak, and the transmission through the fiber is very nearly a linear transformation (except for the square-law at the detector) and as a result, the performance is poor since the mapping is not linearly separable. Increasing the laser peak power results in nonlinear propagation, and we reached the best performance at around 3.43 kW laser peak power. For this optimum power level, correct outputs were estimated from unseen test inputs with a root-mean-squared error (RMSE) of 0.0671. Further power escalation

gradually deteriorated the performance because it drives nonlinear pulse propagation to the Raman beam clean-up regime [125]. In this regime the projected beam profiles become virtually unaffected by the input data. In the other experiments reported below, the optical peak power used was 3.43 kW corresponding to the optimal peak power of the Sinc and COVID-19 diagnosis experiments.

Abalone dataset

The Sinc dataset demonstrates the interpolation capability of our optical computing framework; however, interpolation is not an adequate property for complex inference problems. Therefore, we moved to multivariable inference problems and we tested our computing method on the abalone dataset [126]. The abalone dataset consists of various physical features of sea snails in the dataset that are related to age (e.g., number of rings) that can be used for the prediction of the age of sea snails from eight different parameters. We recorded these 8 parameters on the SLM as a 4x2 matrix with proper pixel scaling. Similar to the Sinc function experiments, the recorded spatial distribution at the distal fiber facet was recorded, flattened (written as a long 1D vector) and fed to the decision layer to perform linear regression. (see Methods). Figure 7.3 presents the true ages (Label) and the corresponding predictions; the figure indicates that the framework learns the ages of the abalone from spatially distributed independent variables with remarkable accuracy (RMSE of 0.126) compared with the output that takes normalized values between 0 and 1.

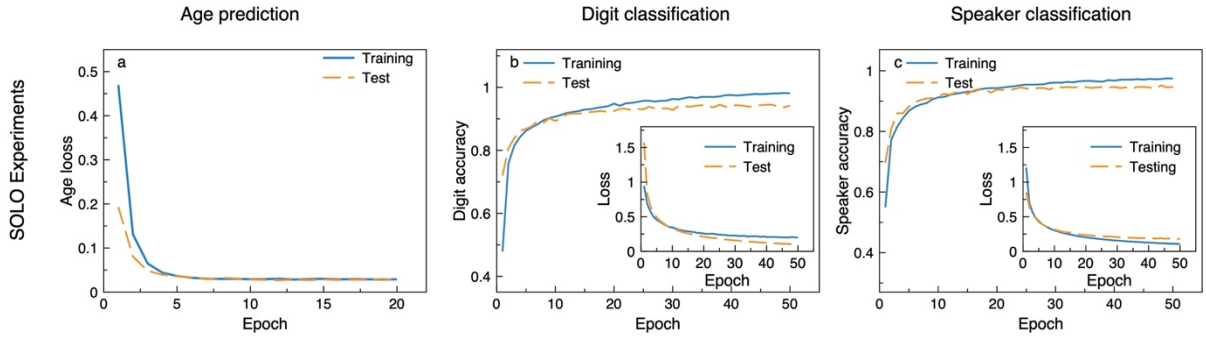


Figure 7.4: Training of the experimental (a-c) results. (a) Evolution of loss function (mean squared error) for age prediction dataset. (b) Evolution of accuracy and loss function (categorical cross entropy) for digit classification with audio dataset. (c) Evolution of accuracy and loss function (categorical cross entropy) for speaker classification with audio dataset.

Face image dataset

Next, we tackled the problem of estimating the age of a person from an image of the person's face. A dataset containing 9780 images of faces of people from different gender and ethnicity with a long age span (0-116) is used [127]. The age is first normalized from 0 to 1. The number 1 represents the oldest person (116 years old). Here again, a single neuron is employed as the decision layer using the recorded fiber output intensity profiles. The achieved RMSE for age prediction is 0.167 normalized years. For the first 1000 samples the true ages (Labels) and predictions are shown in Figure 7.3 b. Some predictions have negative values, which is impossible; however, this

error is due to the final regression layer. This task is promising since image problems are massive and power-hungry in digital machine learning tools and gave birth to the convolutional neural network (CNN) architectures.

Audio digit dataset

Classification of isolated audio records is one of the popular implementations of machine learning, which has a wide range of applications. We employed spoken digit classification to challenge the SOLO system. The audio digit classification dataset incorporates recordings of English digits by six distinct people [128]. Audio recordings are inherently time-varying signals. Following the standard approach, one-dimensional audio signals were converted to two-dimensional representation by generating so-called Mel spectrograms. These spectrograms of audio recordings were provided as inputs to the SLM. Similar to the previous dataset, the spectrograms are encoded on the pulses with high peak power. Instead of 4f imaging, we employed a dispersive element (diffraction grating) after collimating the fiber output (see Figure 7.1). The dispersive element introduces frequency domain changes to spatial distribution of the nonlinearly processed information. In our experiments we noticed that this frequency resolved measurement increases the accuracy of the output decision layer for classification tasks (audio digit and Covid-19) but decreases the performance for the regression datasets (sinc, abalone and face image). The output decision layer classifies the recorded respective fiber output intensity images and 94.5% accuracy over test data is obtained (see Figure 7.3 c) for digit categorization task with frequency resolved beam profile measurement technique (see Methods).

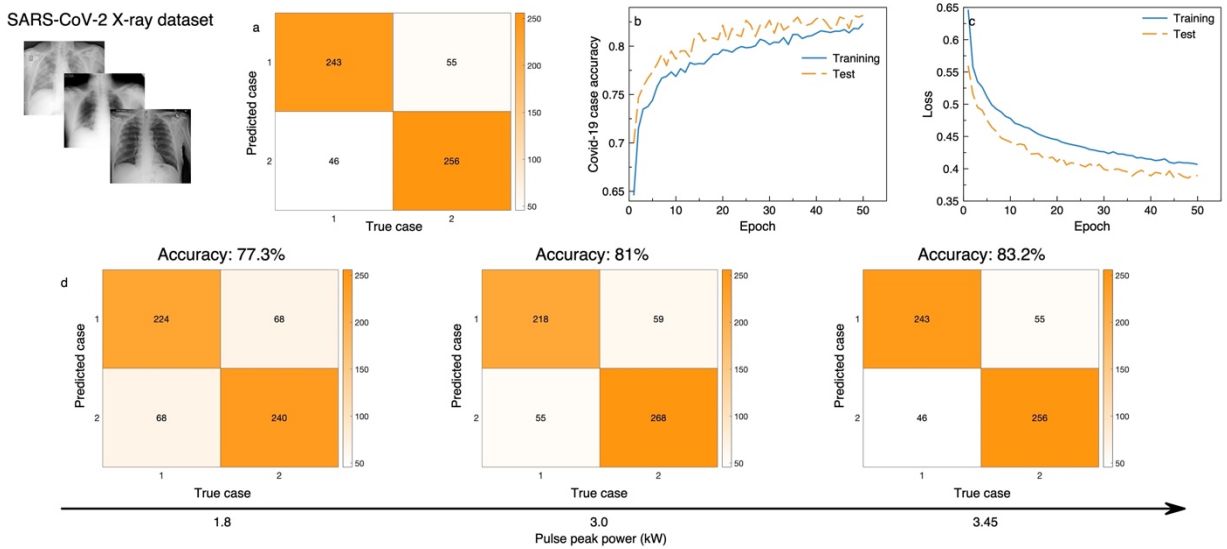


Figure 7.5: Experimentally tested COVID-19 X-ray dataset. (a) Confusion matrix for condition classification. Evolution of accuracy (b) and loss (c) functions (binary cross entropy) for COVID-19 X-ray dataset. (d) Measured effect of nonlinear pulse propagation on categorization accuracy.

To demonstrate the versatility of SOLO, we changed the task for the same dataset and aimed to differentiate the speaker from the audio record. Since the nonlinear transformation is independent of the task, we only updated the decision layer in SOLO and achieved 95.2% accuracy on test data as presented in Figure 7.3 d with frequency resolved beam profile measurement technique (see Methods). The evolution of loss and accuracy (if applicable) functions for our digital decision layer with fiber simulation results are presented in Figure 7.4 a-c.

COVID-19 dataset

Encouraged by the performance we obtained with the relatively simple tasks described so far, we tested SOLO with a difficult challenge of current interest by studying COVID-19 diagnosis with a dataset consisting of 3000 X-ray samples [129]. Similar to the audio dataset, X-ray samples are applied to pulses as phase modulation and the corresponding fiber output intensity patterns were recorded after a dispersive element. By performing classification in the decision layer, 83.2% accuracy over the unseen test set is achieved (see Figure 7.5).

7.2.2 Physical model

The nonlinear mapping performed by the MMF can be investigated by the beam propagation method involving the fiber mode amplitudes (Equation 7.1) [6]. In an ideal fiber without imperfections and bending, with low power pulse or continuous-wave light, only the phases of the mode coefficients change at different rates, due to modal and chromatic dispersion, without any inter-modal power exchange. This behavior is captured by the first term in Equation 7.1. This results in a linear transformation of the field as it propagates through the fiber.

Mode-coupling caused by perturbations due to fiber bending or by impurities, shown by matrix C , also acts as linear mixing (the second term in the following equation) [6], [130].

$$\frac{\partial A_p}{\partial z} = \underbrace{i\delta\beta_0^p A_p - \delta\beta_1^p \frac{\partial A_p}{\partial t} - i\frac{\beta_2}{2} \frac{\partial^2 A_p}{\partial t^2}}_{\text{Propagation and Dispersion}} + \underbrace{i \sum_n C_{p,n} A_n}_{\text{Linear Mode Coupling}} + \underbrace{i\gamma \sum_{l,m,n} \eta_{p,l,m,n} A_l A_m A_n^*}_{\text{Nonlinear Mode Coupling}} \quad (7.1)$$

If the peak power of the pulse is high enough to induce nonlinear behavior in the material, nonlinear mode coupling takes place, and it results in a nonlinear operation on the information spatially encoded in the intense pulse throughout the fiber (the third term in Equation 7.1). For each propagation step, the fiber modes couple to each other according to the linear coupling coefficients and the nonlinear coupling tensor, indicated by η . This nonlinear operator can be modeled at each propagation step by multiplying each three-element combination of mode coefficients with the related entry of the nonlinear mode coupling tensor (for details see Appendix A.1). In Equation 7.1, β_2 is the group velocity dispersion for the central frequency of the pulse and $\delta\beta_0^{(p)}$ ($\delta\beta_1^{(p)}$) is the difference between first (second) Taylor expansion coefficient of the propagation constant for corresponding and the fundamental mode.

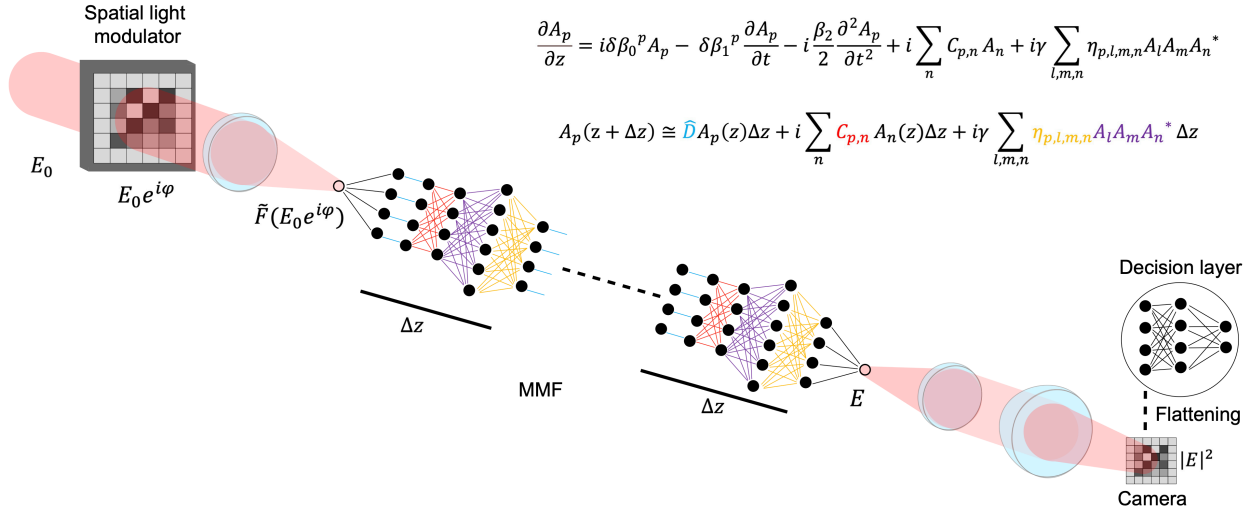


Figure 7.6: Illustration of the spatiotemporal nonlinear pulse propagation as deep neural network architecture in the experimental setup. Each elementary step Δz in the MMF is modeled as a cascade of linear and nonlinear network-like operators capturing the phase delay (in blue), the linear mode coupling due to bending and imperfections (in red), and the nonlinear mode coupling (in magenta and yellow).

7.2.3 Numerical studies

Our experiments demonstrated that the proposed optical computing framework can process information and has potential to learn with adequate performance. To understand the nonlinearity in the MMF, and analyze its effect on learning, we performed time-dependent beam propagation method (TBPM) simulations (see Method section and Appendix A.2). Numerically studying pulse propagation in the 5m GRIN MMF for a dataset with 3000 samples requires approximately 2 years with our GPU parallelized simulation as explained in the Methods section. To reduce the computation time but maintain the required optical nonlinearity, we performed a rescaling of the propagation length and pulse peak power, also explained in the Methods section. We numerically studied the learning sinc function (see Appendix A.3), abalone dataset, face image dataset and audio dataset (see Appendix A.4). Note that the numerical simulation is only partial due to computational limitation and scalar. Due to the scalar nature of the simulation, the simulated fiber supports 120 spatial modes as oppose to the experiments where the test fiber supports 240 spatial modes. This difference causes information loss for the nonlinear mapping takes place in the numerical studies. As a result, the data is not fully linearly separable after the numerically simulated operation whereas experimentally the data becomes linearly separable as evidenced by the flattening of the learning curves in Figure 7.4.

Last but not least, we simulated nonlinear beam propagation in GRIN MMF by encoding the COVID-19 dataset onto the optical pulses. 3000 X-ray samples are propagated numerically and by performing classification to the resulting spatial distribution of the pulses, 70.8% accuracy is achieved (see Figure 7.7 a-c), which is significantly lower than the experimentally obtained classification accuracy (83.2%). For categorization tasks, our numerical results offered lower performances than our experimental studies. These tasks require optically processing 2D information and the

simulations were performed with a shorter fiber lengths and higher peak power due to the previously mentioned computational complexities. This simplification may not have captured the complex nonlinear mapping occurring in a longer fiber and lower peak power.

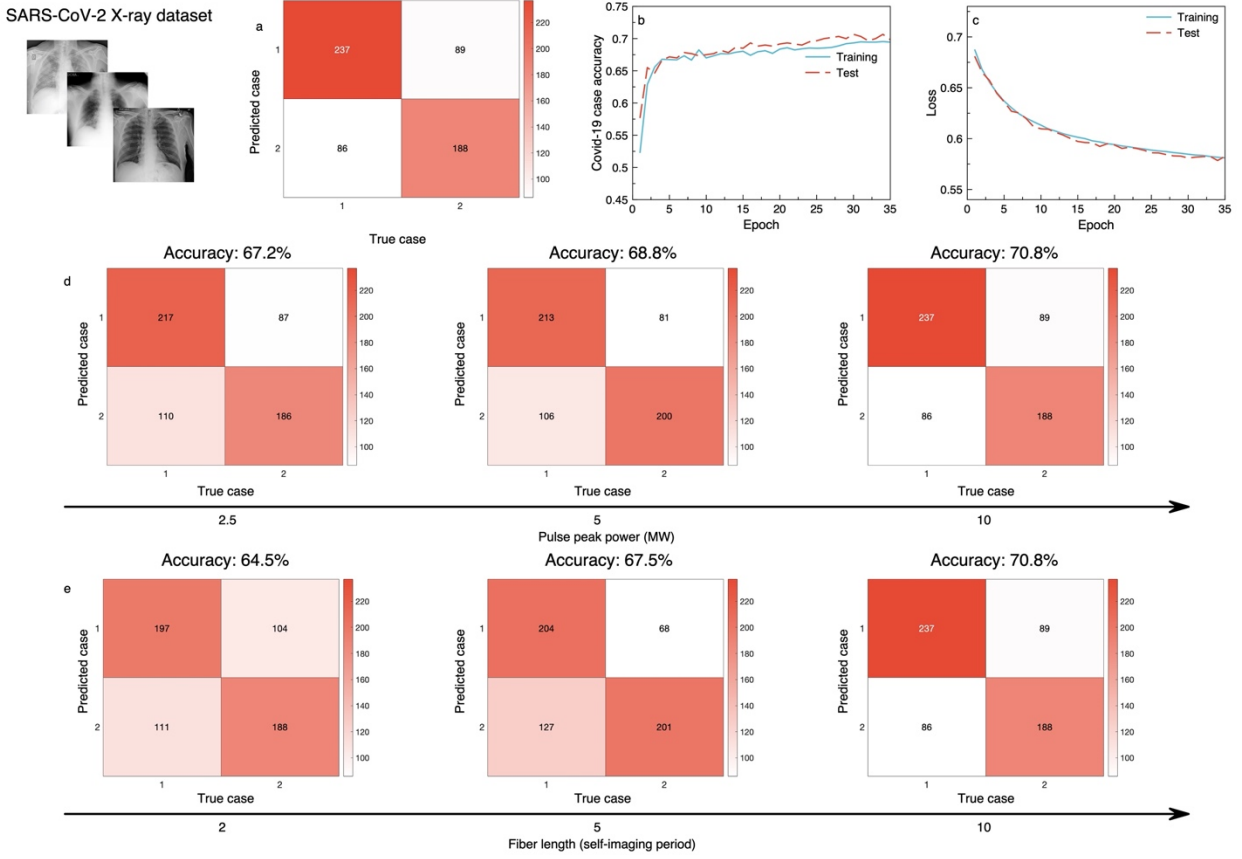


Figure 7.7: Numerically tested COVID-19 X-ray dataset. (a) Confusion matrix for condition classification. Evolution of accuracy (b) and loss (c) functions for COVID-19 X-ray dataset. Simulated effect of pulse peak power (d) and fiber length (e) on categorization accuracy.

To understand the impact of peak power and fiber length, we simulated the COVID-19 dataset with lower peak power levels and shorter fiber lengths. The numerically obtained 70.8% COVID-19 diagnosis accuracy decreased to 68.8 % and 67.2 % when the peak power respectively decreased to half and quarter of the initial power. Similar results were also obtained for shorter propagation lengths such as by decreasing the fiber length from 10 to 5 self-imaging period, we could achieve 67.5% diagnosis accuracy. A further decrease of fiber length by 2 self-imaging periods resulted in 64.5% diagnosis accuracy in our simulations. The numerically achieved confusion matrices for these studies are shown in Figure 7.7. This simulation confirms the role of high intensity light in learning ability.

7.3 Discussion

The present study reveals that the nonlinear interactions in spatiotemporal pulse propagation in MMFs is a key element for learning. It is also important to understand how the performance of SOLO scales with the input data size. We first analyze how the power scales with the input size for

SOLO. The number of modes N in a MMF scales proportionally to the fiber core area, hence the optical power necessary to maintain the same intensity per mode scales linearly with the number of modes. Since a fiber having N modes can accommodate N -dimensional input (law of etendue), the optical power scales with the size of the dimensional input N . The GRIN MMF used in the present study supports 240 modes (counting the polarization degeneracy) and experimentally, learning reached an optimum for a pulse peak power of 3.4 kW for nonlinear optical effects which corresponds to 4.4 mW average optical power for 125 kHz repetition rate and 10 ps pulse duration. Thus, to perform the computation in our experiments, the required average optical power is 18 μ W per fiber mode (4.4 mW/240).

In terms of optical computing operations, we can assume that the number of operations is at least of the order of N^2 , since the input of size N is first multiplied with the number of modes (mode decomposition) and then each of the N modes is operated upon. This can be seen from the propagation Equation 7.1 or its implementation as a network in Figure 7.6. The nonlinear coupling tensor η has the largest terms for self-phase and cross phase modulation [6]. Even keeping only these terms, the number of multiplications reduces to N^2 . As Figure 7.6 suggest, this latter computation is performed many times in the fiber.

With current SLM technology, the number of inputs N can reach up to 107 pixels with a 60 Hz refresh rate [131]. Increasing the number of fiber modes to 107 can be done by employing large core MMFs and/or multicore MMFs. The number of Operations per seconds would then be $N^2 \times$ SLM refresh rate, or more than 6 PetaOps/s. The digital single layer network $N \times 1$ following the optical computation would require only 6×10^7 FLOPs.

At this hypothetical optical computation rate of 6 PetaOps/s, an optimal pulsed laser having 10 ps long pulses with a 60 Hz repetition rate synchronized to the 60 Hz SLM, would require less than 1 W of average optical power. By comparison, the world's fastest supercomputer, Fugaku at the Riken Center in Japan consumes 30 MW, which is 15 gigaFLOPS/W [132]. The SOLO system has 6 orders of magnitude less power consumption per computation.

The digital counterparts of the SOLO can be categorized into three categories. The first approach can be the simulations with exact experimental parameters such as 5 m GRIN MMF. As we already saw such an approach will require more than 2 years of GPU computation for a dataset with 3000 samples when the simulation grid sizes are set to the parameters explained in the Methods section of this paper. The second approach can be to compare SOLO to a deep neural network that is trained to learn the spatiotemporal pulse propagation in MMFs. This approach has been achieved for linear propagation in MMFs with particular datasets [53], [54] with networks having at least >14 layers and >50 million parameters (weights). Nonlinear propagation studies are yet to be investigated but it is reasonable to expect that more complex networks would be required to learn nonlinear propagation in MMF. The last approach can be the standard deep neural networks whose structure is unrelated to SOLO for each specific task. This approach requires designing specific network architectures for each dataset type.

SOLO is a computing framework on which different problems were embedded and were experimentally implemented. Our study demonstrated calculations that yield performance comparable to convolutional neural networks and higher than fully connected ELM architectures (see Appendix A.11). With digital or optical feedback, the present optical paradigm could act as a reservoir network structure [133]. Our tests targeted supervised learning examples, yet unsupervised learning is possible with the proposed technique due to the label-free nonlinear projection behavior of the spatiotemporal pulse propagation. To increase the performance of SOLO or to adapt it for more challenging tasks, the decision layer used in the present studies can be modified with additional layers. Thus, SOLO can compute information as a fast and efficient front-end module.

To evaluate the robustness of the present optical computing method, we repeated the experiments for the COVID-19 dataset a weeks after the prior measurements presented in Figure 7.5. Without requiring a calibration, we obtained the same learning performance level for diagnosing COVID-19 from X-ray images (see Appendix A.8). Furthermore, we performed detailed analysis to determine the stability of the setup. As an analog system, equipment (laser source, SLM) used in the SOLO experiments inherit noise-like behaviors such as laser pointing stability, SLM stability. In our tests (see Appendix A.9), we obtained high stability with 12.63 signal to noise ratio. These demonstrations shows that the proposed SOLO method is remarkably robust, and reproducible.

7.4 Outlook and Conclusion

The presented optical computing framework can be further improved with an active MMF scheme where the fiber is mechanically perturbed [134] or the pump light is also shaped to control spatiotemporal nonlinear propagation. Different cases of adaptive pumping in fiber amplifiers are already demonstrated in the literature [135], [136]. Such an implementation may lead to optically controllable computing with nonlinear fiber optics.

We envision that another implementation of SOLO can be realized with silicon-on-Insulator technology. This technology enables optical functions on integrated circuits, which already resulted in many useful applications [137]. Nonlinear silicon photonics already demonstrated supercontinuum generation through self-phase modulation, light amplification using the Raman effect and matrix convolution operations [138], [139]. By leveraging the existing integrated silicon photonic manufacturing platform, it is possible to implement the machine learning that we demonstrated in optical fibers.

In conclusion, we have shown how spatiotemporal nonlinear pulse propagation in MMFs can optically process information to compute complex machine learning tasks that only sophisticated deep neural networks can tackle. In our benchmarks, the proposed optical computing platform performs as powerful as its digital counterparts for different tasks. With better energy efficiency than previous proposals and a path to PetaOPs scalability, SOLO provides a novel path toward supercomputer-level optical computation.

7.5 Method

7.5.1 Experimental setup

As the light source, an Yb fiber laser (Amplitude Laser-Satsuma) that produces 10ps pulses with a 125 kHz repetition rate is selected. The pulse is centered around 1033 nm with a width of 10 nm. The linearly polarized Gaussian laser output beam is shaped via a phase-only SLM (Holoeye Pluto-NIRII), an 8μm pixel pitch and 60 Hz speed. The SLM prints the desired input pattern on top of a grating phase pattern that expels unmodulated light. We used 5m of a commercial GRIN 50/125 multimode fiber with NA of 0.2; this fiber allows 120 modes per polarization for the given excitation. The phase-modulated light from SLM is imaged onto the MMF with a 15mm lens focal length. The information beam covers the whole MMF core area. The beam-core overlap is checked by imaging the back reflection of the proximal fiber side (not shown in Fig 1). The distal fiber side is magnified 12.5 times through a 4f imaging system and recorded by a camera with a 5.2μm pixel pitch. As an alternative method, instead of 4f imaging, frequency-resolved spatial measurement with a dispersive optical element (grating with a 600line/mm period) is used as presented in Fig 1. Images are 2D arrays, therefore the image datasets are directly mapped to SLM pixels. We illuminated the 600-by-600 pixels central region of the SLM and all images are scaled to that size to cover the entire beam. A blazed grating is added to the pattern to prevent unmodulated DC light to enter the fiber. Encoding 2D arrays are relatively easy than a scalar or 1D input. To handle a scalar input (such as for Sinc experiment), we mapped the scalar value to a 2D array by multiplying the value through a fixed random 2D matrix. This provides unique 2D matrixes for every distinct input value. For a 1D input, we simply converted them to 2D and upscaled to the illumination pixel range. For categorization tasks (audio digit and Covid-19 datasets) significant performance increases are observed and reported here. We monitored fiber output power after and before the MMF continuously. Various neutral density filters are embedded to avoid camera saturation. The pulse power and width are optimized so that the pulse conserves its temporal unity (no temporal splitting) and maximizes spatial interactions.

7.5.2 Numerical Simulations

We implemented a GPU parallelized time-dependent beam propagation method (TBPM) in Python to simulate sufficiently fast nonlinear pulse propagation in the fiber. TBPM simulations often require long computational times due to heavy multidimensional fast Fourier transform calculations. The launched pulses centered at 1030 nm with one ps duration were numerically propagated for 10 self-imaging periods distance. In the experiment, the fiber length is 5 m. To reach a manageable computing time for the datasets with 3000 samples, we performed a rescaling of the propagation length from 5 m to ~5.5 mm. To generate significantly nonlinear spatiotemporal evolution in such a short propagation, we increased the pulse peak power to 10 MW. The time window of simulation is 20ps with 9.8 fs resolution and the spatial window is set as a 64x64 spatial grid. To properly simulate the graded-index MMF's spatial self-imaging, the numerical integration step is set to sample each self-imaging period 16 times. To create an absorptive boundary condition around the core we truncated the parabolic fiber index profile with the super-Gaussian filter. We matched the

launched Gaussian beam diameter ($1/e^2$) to fiber core size ($50\text{ }\mu\text{m}$). For our studies, we encoded data into the beam as a multiplied phase information. After propagation, the obtained pulse is time-averaged and converted into normalized intensity images. There are several ways of converting images into one-dimensional representations. For simplicity, we used a flattened version of downsampled images as an output vector. Finally, flattened output vectors are linearly fitted using the standard Linear Regression method.

Chapter 8 Conclusion

This thesis presents novel approaches and methods to explore spatiotemporal nonlinear dynamics in multimode optical fibers for machine learning, computing and fiber laser applications.

8.1 Summary of the results

Mode-locked fiber lasers with multimode fibers are recently demonstrated alternative paths to achieve ultrashort pulses with high pulse energies and peak powers. The main disadvantage of the method was low output beam quality. We tackled this problem by studying complex spatiotemporal dynamics in an oscillator architecture to improve the beam quality to make these lasers compatible with other high power laser structures such as solid-state lasers. By altering the laser cavity dynamics and achieving self-similar pulse propagation in a multimode fiber laser for the first time, we demonstrated a method to improve output beam quality. While preserving relatively high pulse energy and sub-200 fs pulse durations we reported near-Gaussian beam quality with $M^2 < 1.4$.

In a follow-up study, encouraged by the achieved improvements in the output beam quality, we demonstrated a method to generate a perfect Gaussian (single-mode) beam profile with high pulse energy (> 20 nJ) and sub-100 fs pulse duration. We utilized the dispersion-managed cavity design for tailoring intracavity spatiotemporal dynamics to reach Kerr-induced nonlinear beam cleaning threshold with the mode-locked pulses. The nonlinear beam cleaning dynamics are verified with numerical and experimental studies. With this novel approach, we reported sub-100 fs compressed pulses with single-mode ($M^2 < 1.13$) output beam profile and > 20 nJ pulse energy.

Later, an all-fiber spatiotemporally mode-locked laser architecture is demonstrated. All-fiber laser structures are required to realize compact and stable fiber laser solutions. With Yb-gain, multi-mode interference-based bandpass filtering is implemented in a multimode oscillator to generate mode-locking in a cost-efficient and alignment-free design. With the demonstrated method, we reported spatiotemporal mode-locking with 12 mW average power, 6 ps pulse duration with 24.3 MHz repetition frequency.

To learn and control nonlinear frequency generation in GRIN MMFs, a DNN architecture is utilized for the first time. The relation between shaped beam patterns to excite the GRIN MMF and the generated nonlinearly broadened spectra is learned with the machine learning tool for different nonlinear regimes. Later, the trained neural networks are tested in an experimental setting to generate tailored spectral broadening and achieve tunable frequency generation.

The nonlinear spatiotemporal propagating of ultrashort pulses in GRIN MMFs are learned and utilized to replace time-consuming, heavy simulations with a machine learning architecture capable of acquiring sequential changes in the data, an RNN. We showed that temporal and spatial nonlinear evolution can be grasped by a simple RNN design. With the high accuracy and short inference times, the trained RNN operates 40 times faster than conventional numerical simulations. With sufficient generalization and modifications, this method can be used to replace computationally challenging numerical studies in various research fields.

Finally, a novel optical computing framework based on optical spatiotemporal nonlinear interactions in a GRIN MMF is demonstrated to perform machine learning tasks. Similar to neuromorphic computing methods, nonlinear information processing is achieved with the optical setup and complemented with a simple regression or classification digital layer. We observed that the strength of nonlinear information processing is linked with the strength of optical nonlinear dynamics in the test fiber. The presented energy-efficient optical computing is easily scalable and capable to perform PetaOps with the existing beam shaping and imaging tools.

8.2 Outlook and conclusion

Optical fibers offer a tabletop platform to study complex and nonlinear dynamics rapidly and cost-efficiently. In numerous orientations, nonlinear field propagation in single or multimode optical fiber can mimic various phenomena occurring in physical world settings such as ocean waves with soliton and rogue wave dynamics.

Spatiotemporal mode-locked lasers can be controlled actively by implementing active spatial (SLM) and temporal (acousto/electro-optic modulators) control elements to the cavity. Although these active controlling units introduce bulkiness, they allow more precise tuning in the light propagation thus can open a smart path for the ultrashort pulse generation with high peak power and pulse energy. Furthermore, machine learning algorithms can be implemented to optimize cavity dynamics with active controlling units to multimode lasers similar to our studies for single-pass nonlinear dynamics presented in Chapter 5 and Chapter 6.

Optical computing with MMF nonlinearity is a brand-new concept and offers different approaches to tackle various tasks. The presented information encoding and decoding algorithms in Chapter 7 can be optimized with advanced image processing techniques. Advanced real-time measurement methods can be introduced to replace the conventional 4f imaging technique and may bring more inside. Multiple sources with different parameters (wavelength, pulse duration, etc) can be used instead of a single source with fixed pulse parameters. Different approaches to control the nonlinear information processing in the GRIN MMF to increase the performance of the system in particular datasets can be introduced.

In conclusion, in this thesis, we focused on lasers, machine learning applications and optical computing by exploring nonlinear dynamics in multimode fibers. Yet, these applications are just a sub-

set of the broad capabilities which optical fibers can offer for fundamental science and engineering studies.

Appendix A

A.1 Physical Model of the Computation Framework

The optical beam at any position of the optical fiber can be decomposed into spatial modes of the fiber. In Equation A.1, $E(\rho, \varphi, \omega)$ is the electric field of the light, A_l is the envelope of the corresponding mode along the propagation direction z and F_l is the mode shape. Equation A.2 shows the solution of the mode shape F_l for graded index fibers having relative index difference of Δ and radius of R , L_p is the generalized Laguerre polynomial. The modes propagation constant $\beta_{p,m}$ are calculated using Equation A.3.

$$E(\rho, \varphi, \omega) = \sum_l F_l(\rho, \varphi, \omega) e^{i\beta_l(\omega)z} \tilde{A}_l(z, \omega) \quad (\text{A.1})$$

$$F_{p,m}(\rho, \varphi, \omega) = \sqrt{\frac{p!}{\pi(p+|m|)!}} \frac{\rho^{|m|}}{(w_0/\sqrt{2})^{|m|+1}} e^{-\rho/w_0^2} L_p^{|m|}\left(2\frac{\rho^2}{w_0^2}\right) e^{im\varphi} \quad (\text{A.2})$$

$$\beta_{p,m}(\omega) = k \sqrt{1 - \frac{2\sqrt{\Delta}}{kR} (2p + |m| + 1)} \quad (\text{A.3})$$

Propagation of an intense pulse inside an optical fiber can be analyzed following this representation. Equation A.4 represents the nonlinear spatiotemporal evolution of each mode. Each mode is coupled to the others through the nonlinearity tensor coefficient $\eta_{p,l,m,n}$ which models nonlinear intermodal and intramodal effects, and through a linear coupling coefficient ($C_{p,n}$) which expresses mode coupling due to perturbations to the ideal fiber shape and refractive index distribution, such as bending and impurities. The linear coupling coefficient ($C_{p,n}$) relates perturbation in permittivity (or refractive index) to intermodal model coupling by calculating the overlap integral with the corresponding mode shapes. Similarly, the nonlinearity tensor coefficient ($\eta_{p,l,m,n}$) is computed with the normalized overlap integral of modes. We computed the nonlinear coupling tensor between the modes for our GRIN-50/125 fiber. The tensor has a 1204 size and computing all nonlinear terms took two and a half months on a server computer with 2x Intel Xeon CPU E5-2670 and 384 GB of RAM. The cross-phase modulation coefficients ($\eta_{p,p,q,q}$, inter modal nonlinearities) are

shown in Figure A.1, where the diagonal terms correspond to self-phase modulation ($\eta_{p,p,p,p}$, intramodal nonlinearities). This demonstrates the richness of the nonlinear interaction that SOLO relies upon. Note that four-wave mixing could not be shown on the graph due to its dimensionality.

$$\frac{\partial A_p}{\partial z} = \underbrace{i\delta\beta_0^p A_p - \delta\beta_1^p \frac{\partial A_p}{\partial t} - i\frac{\beta_2}{2} \frac{\partial^2 A_p}{\partial t^2}}_{\text{Propagation and Dispersion}} + \underbrace{i \sum_n C_{p,n} A_n}_{\text{Linear Mode Coupling}} + \underbrace{i\gamma \sum_{l,m,n} \eta_{p,l,m,n} A_l A_m A_n^*}_{\text{Nonlinear Mode Coupling}} \quad (\text{A.4})$$

$$\eta_{p,l,m,n} = \frac{\iint dx dy F_p F_l F_m F_n}{[\iint dx dy F_p \iint dx dy F_l \iint dx dy F_m \iint dx dy F_n]^2} \quad (\text{A.5})$$

$$C_{p,n} = \frac{\omega}{2} \iint dx dy (\tilde{\epsilon}^* - \epsilon) F_p F_n^* \quad (\text{A.6})$$

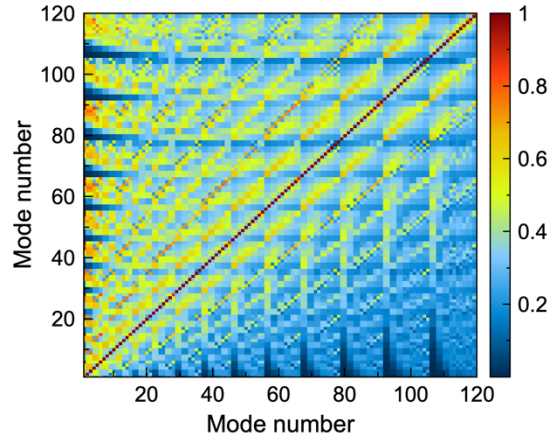


Figure A.1: Intra- and Intermodal nonlinear coupling coefficients ($\eta_{p,p,q,q}, \eta_{p,p,p,p}$)

A.2 Time Dependent Beam Propagation

Instead of considering individual mode field propagation, we use Equation A.7 to describe the total field propagation in a GRIN fiber without perturbations. We numerically implemented Equation A.7 using symmetrized split-step Fourier Method. The codes are implemented in Python + Cupy library which made it possible to utilize powerful GPUs. The time steps are selected at the Nyquist rate defined by the wavelengths range given in Equation A.8-A.9. We used the self-

imaging period as one of our control knobs in simulations using the equations in Equation A.10. A in the Equation A.8 is the slowly varying envelope at the center frequency.

The datasets are divided with a ratio of 0.2 for training (2400 samples) and validation (600 samples). The regression is implemented using Scikit-learn or Tensorflow on Google Colab cloud service which provides an Intel Xeon CPU and Nvidia Tesla V100 GPU. We also used single dense layer without nonlinear activations for linear regression.

$$\frac{\partial A}{\partial z} = \frac{i}{2k_0} \left(\frac{\partial^2 A}{\partial x^2} + \frac{\partial^2 A}{\partial y^2} \right) - i \frac{\beta_2}{2} \frac{\partial^2 A}{\partial t^2} + \frac{\beta_3}{6} \frac{\partial^3 A}{\partial t^3} - \frac{ik_0 \Delta (x^2 + y^2) A}{R^2} + i\gamma |A|^2 A \quad (\text{A.7})$$

$$\lambda_{min} = \frac{1}{\frac{1}{2c\Delta t} + \frac{1}{\lambda_0}} \quad (\text{A.8})$$

$$\lambda_{max} = \frac{1}{-\frac{1}{2c\Delta t} + \frac{1}{\lambda_0}} \quad (\text{A.9})$$

$$\text{Self imaging period} = \frac{\pi R}{\sqrt{2\Delta}} \quad (\text{A.10})$$

A.3 Single value regression of Sinc function

First, we tested the nonlinear information transformation ability of spatiotemporal propagation of high peak power pulses numerically by performing time-dependent beam propagation method (TBPM) simulations. Our first numerical simulation was learning the Sinc function input-output relation numerically duplicating the experiment we described above. The Sinc is a simple nonlinear function that cannot be learned with a single-layer network and it has been used as a standard benchmark to validate learning methods. We used 3000 randomly generated samples, which lie in $[-\pi, \pi]$ to cover the Sinc function's characteristic behavior. We fed the generated samples to TBPM by expanding scalar values to two-dimensional form using a random mask and calculated the nonlinear pulse propagation in the GRIN MMF. The projected intensity distribution at the distal end of the fiber is considered as the nonlinearly transformed information. The linear regression param-

ters are retrieved from the training data, and the overall performance is assessed by the test data. A remarkable learning performance with 0.0039 root-mean-squared error (RMSE) for the test data is obtained. The achieved performance shows that spatiotemporal fiber nonlinearity provides a significant contribution to learning ability. The result proves that our computational device transformed the input space to a higher dimensional space efficiently such that the proposed framework interpolates a function for the unseen data.

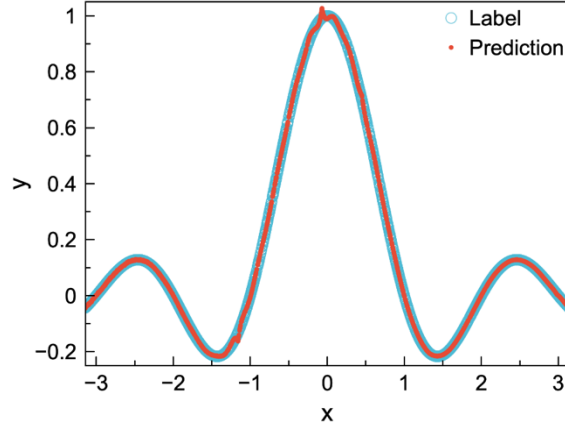


Figure A.2: Learning the Sinc function from simulated data

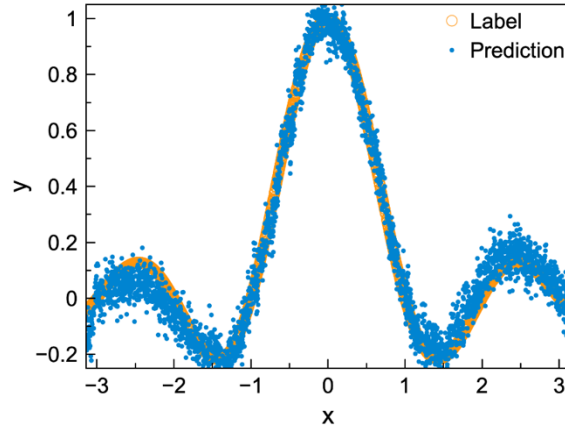


Figure A.3: Learning the Sinc function from experimental data

A.4 Results of numerical studies

We simulated the nonlinear pulse propagation with the abalone dataset information to perform multivariable regression. We encoded the abalone features as the spatial phase distribution of a pulse in our numerical implementation onto the input beam. Similar to the Sinc function, a decision layer to perform linear regression is employed and we obtained an age prediction with remarkable accuracy (RMSE of 0.0831). Figure A.4a presents normalized correct ages and predictions. We continued our numerical studies with the face image dataset. By encoding different human face images into the simulated pulse, each person's age on the images was estimated, and an

RMSE of 0. 2175 on normalized output values indicated again close correspondence with the experimental studies (see Figure A.4b).

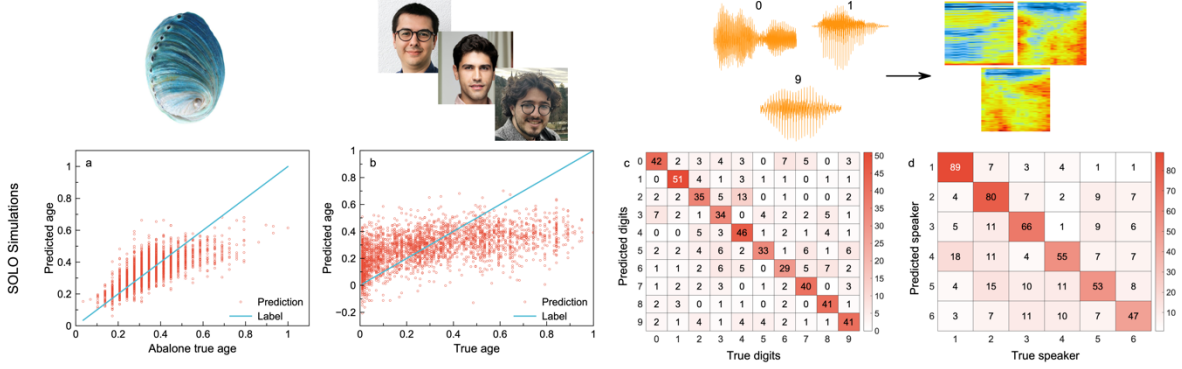


Figure A.4: Experimental (a-d) learning results for regression and classification tasks. (a) Learning of abalone (multivariable) dataset. (b) Age prediction from face image dataset. (c) Confusion matrix for audio dataset digit classification. (d) Confusion matrix for audio dataset speaker classification.

As indicated in our experimental studies, the audio data can also be converted to a two-dimensional format and regarded as an image analysis task by calculating the related spectrogram. This way, we simulated the nonlinear propagation of pulses for audio digit for categorization purposes. By taking the fiber output beam shapes as inputs to a single layer classifier gave approximately 68% accuracy as shown in Figure A.4c. Similar to our experimental investigations, we updated the decision layer and tried to differentiate the speaker from the audio record. In our numerical studies, we obtained 61% accuracy over the unseen test set (see Figure A.4d). The evolution of loss and accuracy (if applicable) functions for our digital decision layer with experimental results are presented in Figure A.5a-c.

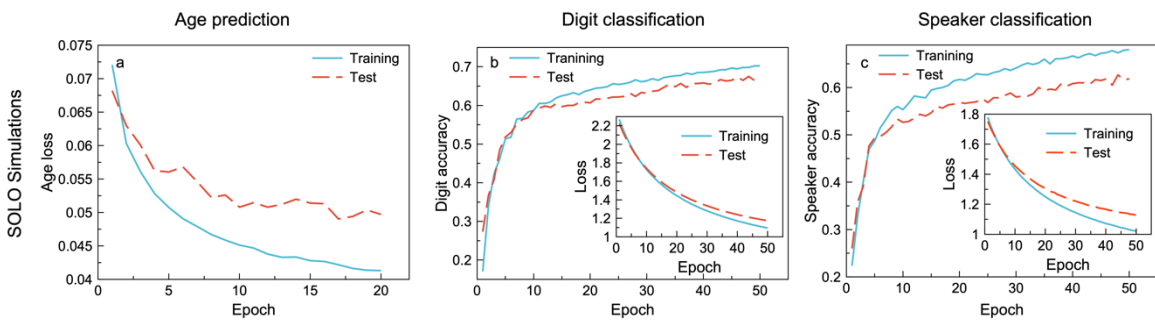


Figure A.5: Training of the numerical (a-c) results. (a) Evolution of loss function for age prediction dataset. (b) Evolution of accuracy and loss function for digit classification with audio dataset. (c) Evolution of accuracy and loss function for speaker classification with audio dataset.

A.5 Power Oscillations during experiment

Learning is related to the amount of nonlinearity (or power). Therefore, stable power is required during experiments. Figure A.6 shows power fluctuations recorded at the fiber end. There is a

small variation due to the modulated diffraction efficiency of grating that depends on the encoded patterns. During this measurement, the mean output average power is 1.58 mW and standard deviation is 0.0292 which results in 1.84% power oscillation for the dataset.

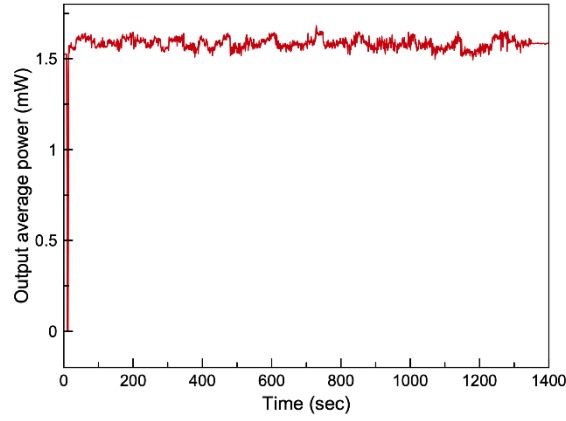


Figure A.6: Output power fluctuations of Face dataset

A.6 Peak power vs Beam and Spectrum Analysis

The effect of the nonlinearity on the output beam shape and spectrum are shown in Figure A.7. In these experiments, a symmetric Gaussian beam with flat phase is injected without any encoding. The power of the beam at the output of the fiber is concentrated in the center. In Figure A.7, we observe that an increase of peak power spreads the spectrum and the spatial distribution of the output beam initially spread from center (Figure A.7a-b). Raman beam cleaning then becomes dominant when the power further increase, which creates again a beam with power concentrated in the center.

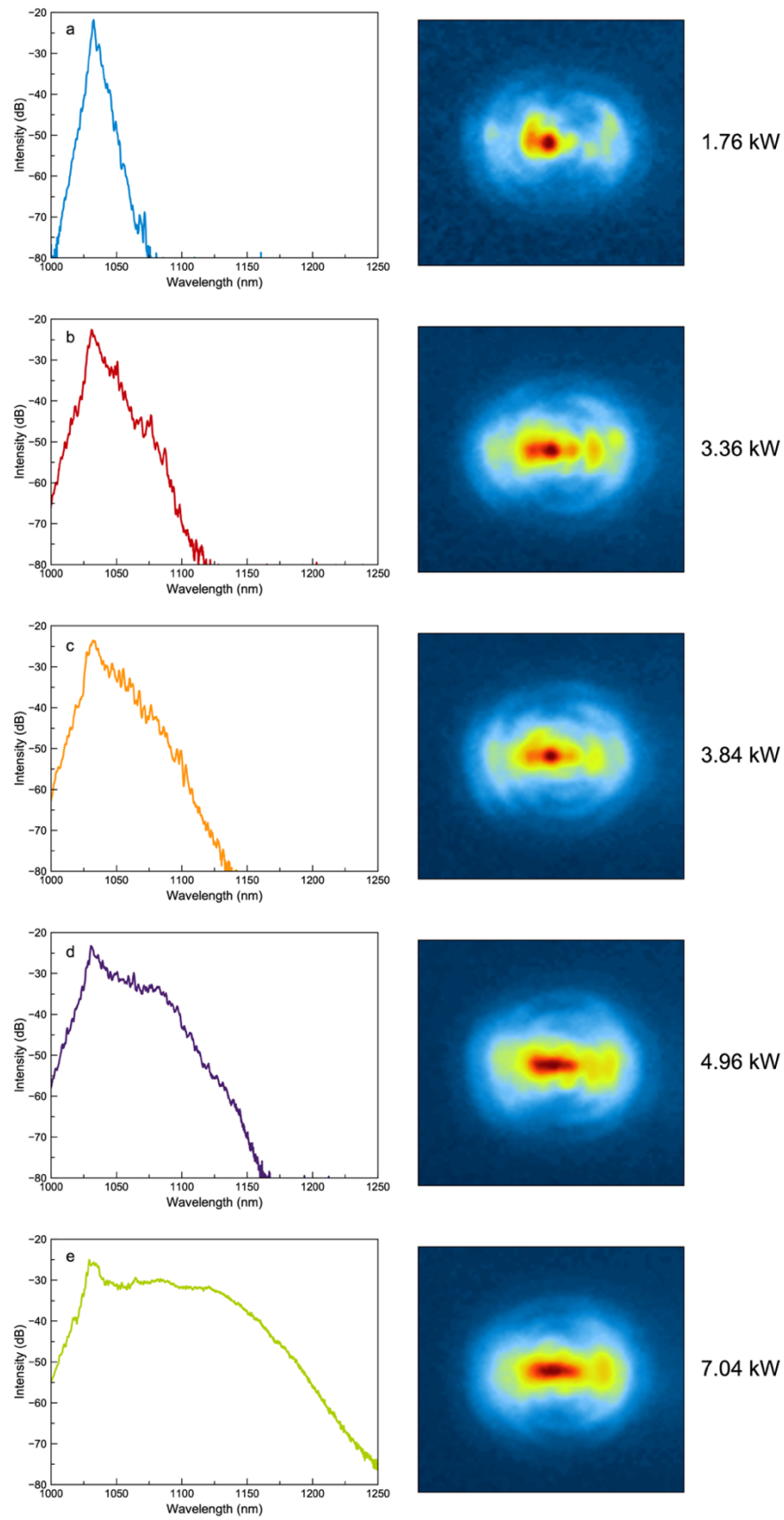


Figure A.7: Spectrum and output beam evolution at the end of the test fiber with increasing pulse peak power.

A.7 Robustness of experiments

The robustness test results of the experimentally demonstrated optical computing method are presented in this section. The exact same experiments with the COVID 19 X-ray images were performed again at a week interval. Around 82% accuracy over test data is achieved like the results obtained in Figure 7.5 in the main text. These results (Figure A.8) validate the robustness of the present optical computing framework.

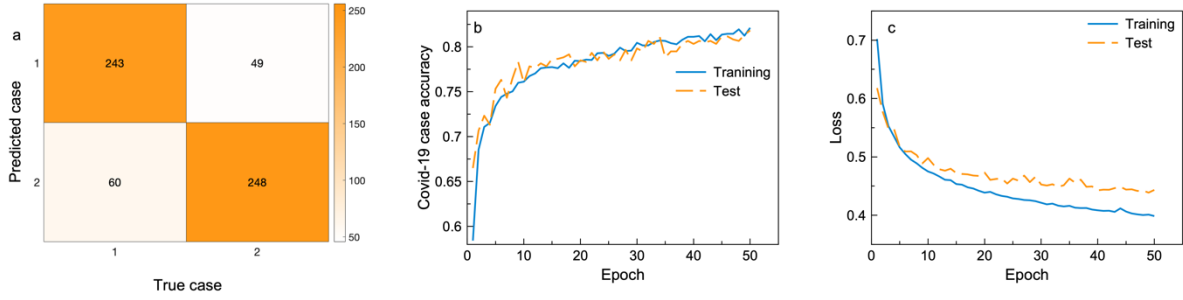


Figure A.8: Experimentally tested COVID-19 X-ray dataset. (a) Confusion matrix for condition classification. Evolution of accuracy (b) and loss (c) functions for COVID-19 X-ray dataset.

A.8 Covid-19 X-ray dataset outputs

An example of input and output relation in SOLO is presented in Figure A.9. Here the input images are loaded on the SLM. After propagation through the fiber, the beam profile is recorded corresponding to each respective input. These beam profiles contain the nonlinearly processed input information for the decision layer, as explained in detail in the Methods section in Chapter 7.

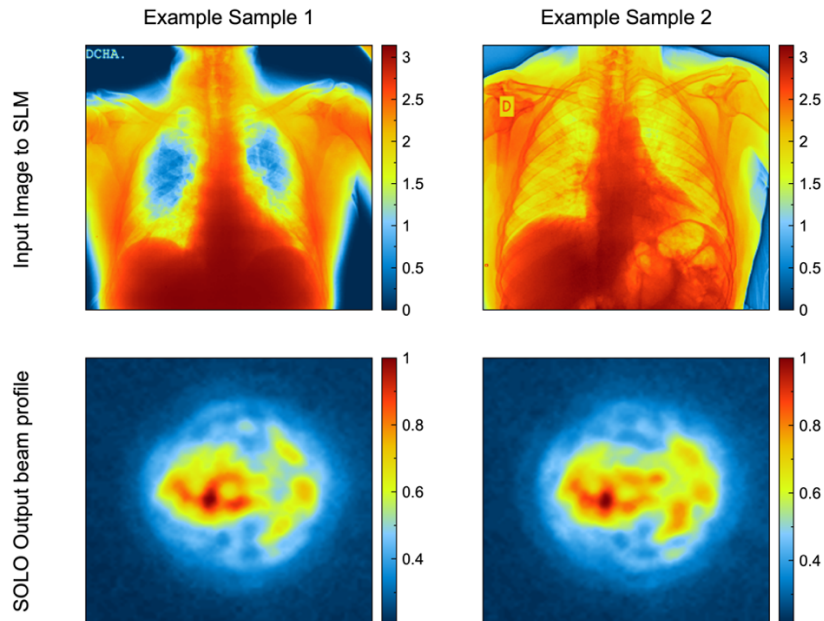


Figure A.9: Experimentally used input images and SOLO output beam profiles for COVID-19 X-ray dataset.

A.9 Stability and noise of experiments

To measure the stability and the noise of the experiments, we send the same data (1st image in Covid-19 X-ray dataset) for an hour in the SOLO experiment. In every step, the image is encoded to SLM from scratch and the fiber output measurements are performed. The Figure A.10 and Figure A.11 shows the changes in the obtained fiber output images. The measurement time for the dataset of a 3000 sample in our experiments is 30 minutes. For this time interval, the average RMSE in the presented measurement in Figure A.11 is 0.079 which corresponds to a 12.63 signal to noise ratio (SNR). With the $\log_2(\text{SNR})$ relation, the bit accuracy of the experiment is around 3.65.

The obtained SNR and RMSE values include all the possible noise and drift sources that can take place in our experimental configuration. These possible noise and drift sources include laser pointing stability, SLM's electronic and temperature noise and optical alignment changes.

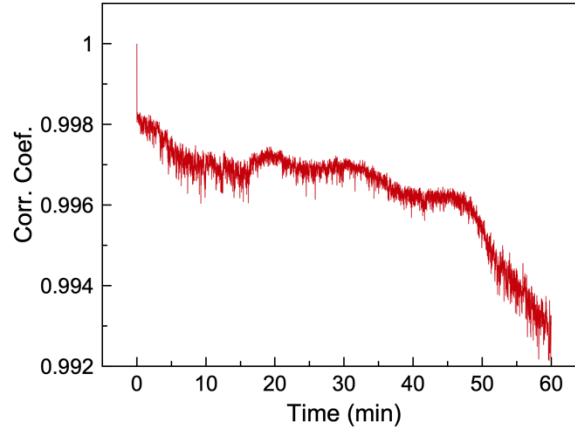


Figure A.10: Pearson correlation coefficient between the first fiber output beam profile and the following measurements over an hour.

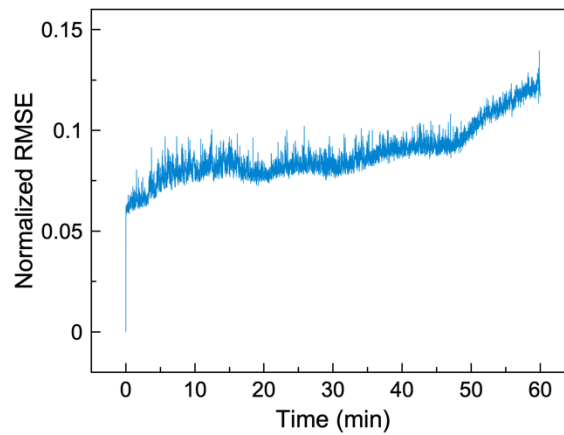


Figure A.11: Normalized root mean squared error between the first fiber output beam profile and the following measurements over an hour.

A.10 Effect of peak power for other datasets

Similar to the sinc function dataset presented in Figure 7.2, peak power is the only controlling factor for adjusting the accumulated nonlinear interactions inside the fiber for the reported configuration. As an example, impact of the peak power on the accuracy is demonstrated in Appendix Table A.1 for the audio digit and Covid-19 X-ray datasets.

Peak power (kW)	Covid-19 dataset acc.	Audio digit dataset acc.
1.76	77%	91%
3.11	78%	92%
3.47	83%	95%
3.77	78%	93%
7.09	77%	91%

Appendix Table A.1

A.11 Comparison of SOLO with digital neural networks

To make a comparison of the performance of SOLO with its digital counterparts, we performed the classification tasks with Covid-19 and Audio dataset by using an ELM and convolutional neural network (CNN), similar to LeNet. The ELM is consisting of 1 layer with fixed weights and nonlinear (sigmoid) activation function and a following trainable layer. The CNN is consisting of 3 convolutional layers (with maxpool and dropout features) and 2 dense layers. The accuracy comparison between the computation architectures is presented in Appendix Table A.2.

Architecture	Acc. for Covid-19	Acc. for Audio Digit	Acc. for Audio Speaker
SOLO	83%	95%	95%
ELM	75%	82%	88%
CNN (3C+2D)	91%	98%	99%

Appendix Table A.2

References

- [1] K. C. Kao and G. A. Hockham, "Dielectric-fibre surface waveguides for optical frequencies," *Proc. Inst. Electr. Eng.*, vol. 14, no. 5, pp. 11–12, 1997, doi: 10.1049/piee.1966.0189.
- [2] J. Hecht, *City of light: the story of fiber optics*. Oxford University Press on Demand, 2004.
- [3] R. J. Mears, L. Reekie, I. M. Jauncey, and D. N. Payne, "Low-noise erbium-doped fibre amplifier operating at 1.54 μm ," *Electron. Lett.*, vol. 23, no. 19, pp. 1026–1028, 1987.
- [4] G. P. Agrawal, "Nonlinear fiber optics 5th ed." Academic Press, New York, 2012.
- [5] J. B. MacChesney, P. B. O'Connor, and H. M. Presby, "A new technique for the preparation of low-loss and graded-index optical fibers," *Proc. IEEE*, vol. 62, no. 9, pp. 1280–1281, 1974.
- [6] A. Mafi, "Pulse Propagation in a Short Nonlinear Graded-Index Multimode Optical Fiber," *J. Light. Technol.*, vol. 30, no. 17, pp. 2803–2811, 2012, doi: 10.1109/JLT.2012.2208215.
- [7] R. H. Stolen and E. P. Ippen, "Raman gain in glass optical waveguides," *Appl. Phys. Lett.*, vol. 22, no. 6, pp. 276–278, 1973, doi: 10.1063/1.1654637.
- [8] R. H. Stolen, W. J. Tomlinson, H. A. Haus, and J. P. Gordon, "Raman response function of silica-core fibers," *J. Opt. Soc. Am. B*, vol. 6, no. 6, p. 1159, 1989, doi: 10.1364/josab.6.001159.
- [9] G. P. Agrawal, "Nonlinear fiber optics: its history and recent progress," *J. Opt. Soc. Am. B*, vol. 28, no. 12, p. A1, 2011, doi: 10.1364/josab.28.0000a1.
- [10] J. M. Dudley, G. Genty, and S. Coen, "Supercontinuum generation in photonic crystal fiber," *Rev. Mod. Phys.*, vol. 78, no. 4, pp. 1135–1184, 2006, doi: 10.1103/RevModPhys.78.1135.
- [11] J. M. Dudley and J. R. Taylor, *Supercontinuum generation in optical fibers*. Cambridge University Press, 2010.
- [12] T. Udem, R. Holzwarth, and T. W. Hänsch, "Optical frequency metrology," *Nature*, vol. 416, no. 6877, pp. 233–237, 2002, doi: 10.1038/416233a.
- [13] T. W. Hänsch, "Nobel lecture: Passion for precision," *Rev. Mod. Phys.*, vol. 78, no. 4, pp. 1297–1309, 2006, doi: 10.1103/RevModPhys.78.1297.
- [14] I. P. Alcock, A. I. Ferguson, D. C. Hanna, and A. C. Tropper, "Mode-locking of a neodymium-doped monomode fibre laser," *Electron. Lett.*, vol. 22, no. 5, pp. 268–269, 1986.
- [15] J. D. Kafka, D. W. Hall, and T. Baer, "Mode-locked erbium-doped fiber laser with soliton pulse shaping," *Opt. Lett.*, vol. 14, no. 22, p. 1269, 1989, doi: 10.1364/ol.14.001269.
- [16] M. E. Fermann, V. I. Kruglov, B. C. Thomsen, J. M. Dudley, and J. D. Harvey, "Self-Similar Propagation and Amplification of Parabolic Pulses in Optical Fibers," *Phys. Rev. Lett.*, vol. 84, no. 26, pp. 6010–6013, Jun. 2000, doi: 10.1103/PhysRevLett.84.6010.
- [17] W. H. Renninger, A. Chong, and F. W. Wise, "Self-similar pulse evolution in an all-normal-dispersion laser," *Phys. Rev. A - At. Mol. Opt. Phys.*, vol. 82, no. 2, pp. 3–6, 2010, doi: 10.1103/PhysRevA.82.021805.
- [18] B. Ortaç, A. Hideur, T. Chartier, M. Brunel, C. Özkul, and F. Sanchez, "90-fs stretched-pulse ytterbium-doped double-clad fiber laser," *Opt. Lett.*, vol. 28, no. 15, p. 1305, Aug. 2003, doi: 10.1364/OL.28.001305.
- [19] A. Chong, J. Buckley, W. Renninger, and F. Wise, "All-normal-dispersion femtosecond fiber laser," *Opt. Express*, vol. 14, no. 21, p. 10095, 2006, doi: 10.1364/OE.14.010095.
- [20] M. E. Fermann and I. Hartl, "Ultrafast fibre lasers," *Nat. Photonics*, vol. 7, no. 11, pp. 868–874, 2013, doi: 10.1038/nphoton.2013.280.
- [21] B. Ortaç, J. Limpert, and A. Tünnermann, "High-energy femtosecond Yb-doped fiber laser operating in the anomalous

- dispersion regime," *Opt. Lett.*, vol. 32, no. 15, p. 2149, Aug. 2007, doi: 10.1364/OL.32.002149.
- [22] B. Ortaç, O. Schmidt, T. Schreiber, J. Limpert, A. Tünnermann, and A. Hideur, "High-energy femtosecond Yb-doped dispersion compensation free fiber laser," *Opt. Express*, vol. 15, no. 17, p. 10725, 2007, doi: 10.1364/oe.15.010725.
- [23] B. Ortaç, M. Baumgartl, J. Limpert, and A. Tünnermann, "Approaching microjoule-level pulse energy with mode-locked femtosecond fiber lasers," *Opt. Lett.*, vol. 34, no. 10, p. 1585, 2009, doi: 10.1364/ol.34.001585.
- [24] M. Baumgartl, C. Lecaplain, A. Hideur, J. Limpert, and A. Tünnermann, "66 W average power from a microjoule-class sub-100 fs fiber oscillator," *Opt. Lett.*, vol. 37, no. 10, p. 1640, 2012, doi: 10.1364/ol.37.001640.
- [25] F. Poletti and P. Horak, "Description of ultrashort pulse propagation in multimode optical fibers," *J. Opt. Soc. Am. B*, vol. 25, no. 10, p. 1645, 2008, doi: 10.1364/josab.25.001645.
- [26] P. Horak and F. Poletti, "Multimode nonlinear fibre optics: Theory and applications," *Recent Prog. Opt. Fiber Res.*, pp. 3–25, 2012.
- [27] H. Pourbeyram, G. P. Agrawal, and A. Mafi, "Stimulated Raman scattering cascade spanning the wavelength range of 523 to 1750 nm using a graded-index multimode optical fiber," *Appl. Phys. Lett.*, vol. 102, no. 20, pp. 1–5, 2013, doi: 10.1063/1.4807620.
- [28] K. Krupa *et al.*, "Observation of Geometric Parametric Instability Induced by the Periodic Spatial Self-Imaging of Multimode Waves," *Phys. Rev. Lett.*, vol. 116, no. 18, pp. 1–5, 2016, doi: 10.1103/PhysRevLett.116.183901.
- [29] L. G. Wright, Z. Liu, D. A. Nolan, M. J. Li, D. N. Christodoulides, and F. W. Wise, "Self-organized instability in graded-index multimode fibres," *Nat. Photonics*, vol. 10, no. 12, pp. 771–776, 2016, doi: 10.1038/nphoton.2016.227.
- [30] U. Teğın and B. Ortaç, "Spatiotemporal Instability of Femtosecond Pulses in Graded-Index Multimode Fibers," *IEEE Photonics Technol. Lett.*, vol. 29, no. 24, pp. 2195–2198, 2017, doi: 10.1109/LPT.2017.2769343.
- [31] L. G. Wright, D. N. Christodoulides, and F. W. Wise, "Controllable spatiotemporal nonlinear effects in multimode fibres," *Nat. Photonics*, vol. 9, no. 5, pp. 306–310, 2015, doi: 10.1038/nphoton.2015.61.
- [32] L. G. Wright, S. Wabnitz, D. N. Christodoulides, and F. W. Wise, "Ultrabroadband Dispersive Radiation by Spatiotemporal Oscillation of Multimode Waves," *Phys. Rev. Lett.*, vol. 115, no. 22, pp. 1–5, 2015, doi: 10.1103/PhysRevLett.115.223902.
- [33] K. Krupa *et al.*, "Spatial beam self-cleaning in multimode fibres," *Nat. Photonics*, vol. 11, no. 4, pp. 237–241, 2017, doi: 10.1038/nphoton.2017.32.
- [34] R. Guenard *et al.*, "Kerr self-cleaning of pulsed beam in an ytterbium doped multimode fiber," *Opt. Express*, vol. 25, no. 5, p. 4783, 2017, doi: 10.1364/oe.25.004783.
- [35] Z. Liu, L. G. Wright, D. N. Christodoulides, and F. W. Wise, "Self-cleaning of femtosecond-pulsed beams in graded-index multimode fiber," *Opt. InfoBase Conf. Pap.*, vol. 41, no. 16, pp. 3675–3678, 2014, doi: 10.1364/FIO.2016.FTu2I.2.
- [36] G. Lopez-Galmiche *et al.*, "Visible supercontinuum generation in a graded index multimode fiber pumped at 1064 nm," *Opt. Lett.*, vol. 41, no. 11, p. 2553, Jun. 2016, doi: 10.1364/OL.41.002553.
- [37] K. Krupa *et al.*, "Spatiotemporal characterization of supercontinuum extending from the visible to the mid-infrared in a multimode graded-index optical fiber," *Opt. Lett.*, vol. 41, no. 24, p. 5785, 2016, doi: 10.1364/ol.41.005785.
- [38] U. Teğın and B. Ortaç, "Cascaded Raman scattering based high power octave-spanning supercontinuum generation in graded-index multimode fibers," *Sci. Rep.*, vol. 8, no. 1, p. 12470, Dec. 2018, doi: 10.1038/s41598-018-30252-9.
- [39] A. Mafi, P. Hofmann, C. J. Salvin, and A. Schülzgen, "Low-loss coupling between two single-mode optical fibers with different mode-field diameters using a graded-index multimode optical fiber," *Opt. Lett.*, vol. 36, no. 18, p. 3596, 2011, doi: 10.1364/ol.36.003596.
- [40] T. Walbaum and C. Fallnich, "Multimode interference filter for tuning of a mode-locked all-fiber erbium laser," *Opt. Lett.*, vol. 36, no. 13, p. 2459, 2011, doi: 10.1364/ol.36.002459.
- [41] U. Teğın and B. Ortaç, "All-fiber all-normal-dispersion femtosecond laser with a nonlinear multimodal interference-based saturable absorber," *Opt. Lett.*, vol. 43, no. 7, p. 1611, Apr. 2018, doi: 10.1364/OL.43.001611.
- [42] L. G. Wright, D. N. Christodoulides, and F. W. Wise, "Spatiotemporal mode-locking in multimode fiber lasers," *Science* (80-

-), vol. 97, no. October, pp. 94–97, 2017, doi: 10.1126/science.aao0831.
- [43] H. Qin, X. Xiao, P. Wang, and C. Yang, “Observation of soliton molecules in a spatiotemporal mode-locked multimode fiber laser,” *Opt. Lett.*, vol. 43, no. 9, p. 1982, 2018, doi: 10.1364/ol.43.001982.
 - [44] Y. Ding, X. Xiao, P. Wang, and C. Yang, “Multiple-soliton in spatiotemporal mode-locked multimode fiber lasers,” *Opt. Express*, vol. 27, no. 8, p. 11435, 2019, doi: 10.1364/oe.27.011435.
 - [45] J. Schmidhuber, “Deep Learning in neural networks: An overview,” *Neural Networks*, vol. 61, pp. 85–117, 2015, doi: 10.1016/j.neunet.2014.09.003.
 - [46] K. O’Shea and R. Nash, “An introduction to convolutional neural networks,” *arXiv Prepr. arXiv1511.08458*, 2015.
 - [47] A. Sherstinsky, “Fundamentals of recurrent neural network (RNN) and long short-term memory (LSTM) network,” *Phys. D Nonlinear Phenom.*, vol. 404, p. 132306, 2020.
 - [48] M. A. Krumbügel, C. L. Ladera, K. W. DeLong, D. N. Fittinghoff, J. N. Sweetser, and R. Trebino, “Direct ultrashort-pulse intensity and phase retrieval by frequency-resolved optical gating and a computational neural network,” *Opt. Lett.*, vol. 21, no. 2, pp. 143–145, 1996.
 - [49] A. Kokhanovskiy *et al.*, “Machine learning-based pulse characterization in figure-eight mode-locked lasers,” *Opt. Lett.*, vol. 44, no. 13, pp. 3410–3413, 2019.
 - [50] C. A. Farfan, J. Epstein, and D. B. Turner, “Femtosecond pulse compression using a neural-network algorithm,” *Opt. Lett.*, vol. 43, no. 20, pp. 5166–5169, 2018.
 - [51] T. Zahavy *et al.*, “Deep learning reconstruction of ultrashort pulses,” *Optica*, vol. 5, no. 5, pp. 666–673, 2018.
 - [52] T. Baumeister, S. L. Brunton, and J. N. Kutz, “Deep learning and model predictive control for self-tuning mode-locked lasers,” *JOSA B*, vol. 35, no. 3, pp. 617–626, 2018.
 - [53] N. Borhani, E. Kakkava, C. Moser, and D. Psaltis, “Learning to see through multimode fibers,” *Optica*, vol. 5, no. 8, pp. 960–966, 2018.
 - [54] B. Rahmani, D. Loterie, G. Konstantinou, D. Psaltis, and C. Moser, “Multimode optical fiber transmission with a deep learning network,” *Light Sci. Appl.*, vol. 7, no. 1, pp. 1–11, 2018.
 - [55] L. Salmela, N. Tzipinakis, A. Foi, C. Billet, J. M. Dudley, and G. Genty, “Predicting ultrafast nonlinear dynamics in fibre optics with a recurrent neural network,” *Nat. Mach. Intell.*, vol. 3, no. 4, pp. 344–354, 2021.
 - [56] G. Genty *et al.*, “Machine learning and applications in ultrafast photonics,” *Nat. Photonics*, vol. 15, no. 2, pp. 91–101, 2021, doi: 10.1038/s41566-020-00716-4.
 - [57] J. W. Goodman, *Introduction to Fourier optics*. Roberts and Company Publishers, 2005.
 - [58] D. A. B. Miller, “Waves, modes, communications and optics,” *arXiv*, vol. 11, no. 3, pp. 679–825, 2019, doi: 10.1364/AOP.11.000679.
 - [59] A. Vander Lugt, “Signal detection by complex spatial filtering,” *IEEE Trans. Inf. theory*, vol. 10, no. 2, pp. 139–145, 1964.
 - [60] N. H. Farhat, D. Psaltis, A. Prata, and E. Paek, “Optical implementation of the Hopfield model,” *Appl. Opt.*, vol. 24, no. 10, p. 1469, 1985, doi: 10.1364/ao.24.001469.
 - [61] D. Psaltis and N. Farhat, “Optical information processing based on an associative-memory model of neural nets with thresholding and feedback,” *Opt. Lett.*, vol. 10, no. 2, p. 98, 1985, doi: 10.1364/ol.10.000098.
 - [62] C. Gallicchio and A. Micheli, “Tree echo state networks,” *Neurocomputing*, vol. 101, pp. 319–337, 2013.
 - [63] W. Maass, “Liquid state machines: motivation, theory, and applications,” *Comput. Context Comput. Log. real world*, pp. 275–296, 2011.
 - [64] G. Bin Huang, Q. Y. Zhu, and C. K. Siew, “Extreme learning machine: Theory and applications,” *Neurocomputing*, vol. 70, no. 1–3, pp. 489–501, 2006, doi: 10.1016/j.neucom.2005.12.126.
 - [65] G. Tanaka *et al.*, “Recent advances in physical reservoir computing: A review,” *Neural Networks*, vol. 115, pp. 100–123,

2019, doi: 10.1016/j.neunet.2019.03.005.

- [66] A. Saade *et al.*, “Random projections through multiple optical scattering: Approximating Kernels at the speed of light,” *2016 IEEE Int. Conf. Acoust. Speech Signal Process.*, pp. 6215–6219, 2016, doi: 10.1109/ICASSP.2016.7472872.
- [67] J. Dong, M. Rafayelyan, F. Krzakala, and S. Gigan, “Large-Scale Optical Reservoir Computing for Spatiotemporal Chaotic Systems Prediction,” *IEEE J. Sel. Top. Quantum Electron.*, vol. 26, no. 1, 2020, doi: 10.1109/JSTQE.2019.2936281.
- [68] U. Paudel, M. Luengo-Kovac, J. Pilawa, T. J. Shaw, and G. C. Valley, “Classification of time-domain waveforms using a speckle-based optical reservoir computer,” *Opt. Express*, vol. 28, no. 2, pp. 1225–1237, 2019, doi: 10.1364/oe.379264.
- [69] S. Sunada, K. Kanno, and A. Uchida, “Using multidimensional speckle dynamics for high-speed, large-scale, parallel photonic computing,” *Opt. Express*, vol. 28, no. 21, p. 30349, 2020, doi: 10.1364/oe.399495.
- [70] D. Brunner, M. C. Soriano, C. R. Mirasso, and I. Fischer, “Parallel photonic information processing at gigabyte per second data rates using transient states,” *Nat. Commun.*, vol. 4, 2013, doi: 10.1038/ncomms2368.
- [71] G. Wetzstein *et al.*, “Inference in artificial intelligence with deep optics and photonics,” *Nature*, vol. 588, no. 7836, pp. 39–47, 2020, doi: 10.1038/s41586-020-2973-6.
- [72] A. Isomäki and O. G. Okhotnikov, “Femtosecond soliton mode-locked laser based on ytterbium-doped photonic bandgap fiber,” *Opt. Express*, vol. 14, no. 20, pp. 9238–9243, 2006.
- [73] F. Ö. Ilday, J. R. Buckley, W. G. Clark, and F. W. Wise, “Self-similar evolution of parabolic pulses in a laser,” *Phys. Rev. Lett.*, vol. 92, no. 21, p. 213902, 2004.
- [74] K. Özgören and F. Ö. Ilday, “All-fiber all-normal dispersion laser with a fiber-based Lyot filter,” *Opt. Lett.*, vol. 35, no. 8, pp. 1296–1298, 2010.
- [75] V. I. Kruglov, A. C. Peacock, J. M. Dudley, and J. D. Harvey, “Self-similar propagation of high-power parabolic pulses in optical fiber amplifiers,” *Opt. Lett.*, vol. 25, no. 24, p. 1753, 2000, doi: 10.1364/ol.25.001753.
- [76] D. Strickland and G. Mourou, “Compression of amplified chirped optical pulses,” *Opt. Commun.*, vol. 55, no. 6, pp. 447–449, 1985.
- [77] C. Ma, A. Khanolkar, and A. Chong, “High-performance tunable, self-similar fiber laser,” *Opt. Lett.*, vol. 44, no. 5, pp. 1234–1236, 2019.
- [78] W. H. Renninger and F. W. Wise, “Optical solitons in graded-index multimode fibres,” *Nat. Commun.*, vol. 4, 2013, doi: 10.1038/ncomms2739.
- [79] A. S. Ahsan and G. P. Agrawal, “Graded-index solitons in multimode fibers,” *Opt. Lett.*, vol. 43, no. 14, pp. 3345–3348, 2018.
- [80] K. Krupa *et al.*, “Spatiotemporal light-beam compression from nonlinear mode coupling,” *Phys. Rev. A*, vol. 97, no. 4, p. 43836, 2018.
- [81] M. Hofer, M. H. Ober, F. Haberl, and M. E. Fermann, “Characterization of ultrashort pulse formation in passively mode-locked fiber lasers,” *IEEE J. Quantum Electron.*, vol. 28, no. 3, pp. 720–728, 1992.
- [82] J. W. Nicholson, J. Jasapara, W. Rudolph, F. G. Omenetto, and A. J. Taylor, “Full-field characterization of femtosecond pulses by spectrum and cross-correlation measurements,” *Opt. Lett.*, vol. 24, no. 23, pp. 1774–1776, 1999.
- [83] P. Grelu and N. Akhmediev, “Dissipative solitons for mode-locked lasers,” *Nat. Photonics*, vol. 6, no. 2, pp. 84–92, 2012.
- [84] U. Teğin, E. Kakkava, B. Rahmani, D. Psaltis, and C. Moser, “Spatiotemporal self-similar fiber laser,” *Optica*, vol. 6, no. 11, p. 1412, Nov. 2019, doi: 10.1364/OPTICA.6.001412.
- [85] J. Hult, “A fourth-order Runge–Kutta in the interaction picture method for simulating supercontinuum generation in optical fibers,” *J. Light. Technol.*, vol. 25, no. 12, pp. 3770–3775, 2007.
- [86] Y. Chen *et al.*, “Dispersion-managed mode locking,” *JOSA B*, vol. 16, no. 11, 1999.
- [87] K. Tamura, E. P. Ippen, H. A. Haus, and L. E. Nelson, “77-fs pulse generation from a stretched-pulse mode-locked all-fiber ring laser,” *Opt. Lett.*, vol. 18, no. 13, pp. 1080–1082, 1993.

-
- [88] Ç. Şenel, R. Hamid, C. Erdoğan, M. Çelik, and F. Ö. Ilday, "Tailored Design of Mode-Locking Dynamics for Low-Noise Frequency-Comb Generation," *Phys. Rev. Appl.*, vol. 10, no. 2, p. 024027, Aug. 2018, doi: 10.1103/PhysRevApplied.10.024027.
- [89] O. S. Sidelnikov, E. V Podivilov, M. P. Fedoruk, and S. Wabnitz, "Random mode coupling assists Kerr beam self-cleaning in a graded-index multimode optical fiber," *Opt. Fiber Technol.*, vol. 53, p. 101994, 2019.
- [90] Y. Leventoux *et al.*, "Highly efficient few-mode spatial beam self-cleaning at 1.5 μm ," *Opt. Express*, vol. 28, no. 10, pp. 14333–14344, 2020.
- [91] L. G. Wright *et al.*, "Mechanisms of spatiotemporal mode-locking," *Nat. Phys.*, vol. 16, no. 5, pp. 565–570, 2020.
- [92] M. Schultz, H. Karow, O. Prochnow, D. Wandt, U. Morgner, and D. Kracht, "All-fiber ytterbium femtosecond laser without dispersion compensation," *Opt. Express*, vol. 16, no. 24, pp. 19562–19567, 2008.
- [93] L. Zhang, J. Hu, J. Wang, and Y. Feng, "Tunable all-fiber dissipative-soliton laser with a multimode interference filter," *Opt. Lett.*, vol. 37, no. 18, pp. 3828–3830, 2012.
- [94] H. Wu *et al.*, "Pulses with switchable wavelengths and hysteresis in an all-fiber spatio-temporal mode-locked laser," *Appl. Phys. Express*, vol. 13, no. 2, p. 22008, 2020.
- [95] U. Teğin, B. Rahmani, E. Kakkava, D. Psaltis, and C. Moser, "Single-mode output by controlling the spatiotemporal nonlinearities in mode-locked femtosecond multimode fiber lasers," *Adv. Photonics*, vol. 2, no. 05, pp. 1–8, Oct. 2020, doi: 10.1117/1.AP.2.5.056005.
- [96] W. H. Renninger, A. Chong, and F. W. Wise, "Dissipative solitons in normal-dispersion fiber lasers," *Phys. Rev. A*, vol. 77, no. 2, p. 23814, 2008.
- [97] D. J. Richardson, J. M. Fini, and L. E. Nelson, "Space-division multiplexing in optical fibres," *Nat. Photonics*, vol. 7, no. 5, pp. 354–362, 2013.
- [98] B. A. Flusberg, E. D. Cocker, W. Piyawattanametha, J. C. Jung, E. L. M. Cheung, and M. J. Schnitzer, "Fiber-optic fluorescence imaging," *Nat. Methods*, vol. 2, no. 12, pp. 941–950, 2005.
- [99] D. Loterie, S. Farahi, I. Papadopoulos, A. Goy, D. Psaltis, and C. Moser, "Digital confocal microscopy through a multimode fiber," *Opt. Express*, vol. 23, no. 18, pp. 23845–23858, 2015.
- [100] E. Kakkava *et al.*, "Selective femtosecond laser ablation via two-photon fluorescence imaging through a multimode fiber," *Biomed. Opt. Express*, vol. 10, no. 2, pp. 423–433, 2019.
- [101] J. Trägårdh, T. Pikálek, M. Šerý, T. Meyer, J. Popp, and T. Čižmár, "Label-free CARS microscopy through a multimode fiber endoscope," *Opt. Express*, vol. 27, no. 21, pp. 30055–30066, 2019, doi: 10.1364/OE.27.030055.
- [102] E. Kakkava *et al.*, "Imaging through multimode fibers using deep learning: The effects of intensity versus holographic recording of the speckle pattern," *Opt. Fiber Technol.*, vol. 52, p. 101985, 2019.
- [103] E. Deliancourt *et al.*, "Wavefront shaping for optimized many-mode Kerr beam self-cleaning in graded-index multimode fiber," *Opt. Express*, vol. 27, no. 12, pp. 17311–17321, 2019.
- [104] O. Tzang, A. M. Caravaca-Aguirre, K. Wagner, and R. Piestun, "Adaptive wavefront shaping for controlling nonlinear multimode interactions in optical fibres," *Nat. Photonics*, vol. 12, no. 6, pp. 368–374, 2018.
- [105] F. Poletti and P. Horak, "Dynamics of femtosecond supercontinuum generation in multimode fibers," *Opt. Express*, vol. 17, no. 8, pp. 6134–6147, 2009.
- [106] C. Rosales-Guzmán and A. Forbes, *How to shape light with spatial light modulators*. SPIE Press, 2017.
- [107] J. Rogel-Salazar, "The gross-pitaevskii equation and bose-einstein condensates," *Eur. J. Phys.*, vol. 34, no. 2, p. 247, 2013.
- [108] U. Teğin, B. Rahmani, E. Kakkava, N. Borhani, C. Moser, and D. Psaltis, "Controlling spatiotemporal nonlinearities in multimode fibers with deep neural networks," *APL Photonics*, vol. 5, no. 3, 2020, doi: 10.1063/1.5138131.
- [109] U. Teğin, M. Yıldırım, İ. Oğuz, C. Moser, and D. Psaltis, "Scalable Optical Learning Operator," *arXiv*, Dec. 2020, [Online]. Available: <http://arxiv.org/abs/2012.12404>.

-
- [110] Y. An, L. Huang, J. Li, J. Leng, L. Yang, and P. Zhou, "Learning to decompose the modes in few-mode fibers with deep convolutional neural network," *Opt. Express*, vol. 27, no. 7, pp. 10127–10137, 2019.
 - [111] S. Rothe, Q. Zhang, N. Koukourakis, and J. W. Czarnecki, "Deep learning for computational mode decomposition in optical fibers," *Appl. Sci.*, vol. 10, no. 4, p. 1367, 2020.
 - [112] L. Cutrona, E. N. Leith, C. Palermo, and L. Porcello, "Optical data processing and filtering systems," *IRE Trans. Inf. Theory*, vol. 6, no. 3, pp. 386–400, 1960.
 - [113] L. J. Cutrona, E. N. Leith, L. J. Porcello, and W. E. Vivian, "On the application of coherent optical processing techniques to synthetic-aperture radar," *Proc. IEEE*, vol. 54, no. 8, pp. 1026–1032, 1966.
 - [114] D. A. B. Miller *et al.*, "Novel hybrid optically bistable switch: The quantum well self-electro-optic effect device," *Appl. Phys. Lett.*, vol. 45, no. 1, pp. 13–15, 1984.
 - [115] J. W. Goodman, F. J. Leonberger, S.-Y. Kung, and R. A. Athale, "Optical interconnections for VLSI systems," *Proc. IEEE*, vol. 72, no. 7, pp. 850–866, 1984.
 - [116] M. R. Feldman, S. C. Esener, C. C. Guest, and S. H. Lee, "Comparison between optical and electrical interconnects based on power and speed considerations," *Appl. Opt.*, vol. 27, no. 9, pp. 1742–1751, 1988.
 - [117] D. Psaltis, D. Brady, X.-G. Gu, and S. Lin, "Holography in artificial neural networks," *Nature*, vol. 343, no. 6256, pp. 325–330, 1990, doi: 10.1038/343325a0.
 - [118] C. Cortes and V. Vapnik, "Support-vector networks," *Mach. Learn.*, vol. 20, no. 3, pp. 273–297, 1995.
 - [119] W. S. Noble, "What is a support vector machine?," *Nat. Biotechnol.*, vol. 24, no. 12, pp. 1565–1567, 2006.
 - [120] L. Larger *et al.*, "Photonic information processing beyond Turing: an optoelectronic implementation of reservoir computing," *Opt. Express*, vol. 20, no. 3, pp. 3241–3249, 2012.
 - [121] K. Vandoorne *et al.*, "Experimental demonstration of reservoir computing on a silicon photonics chip," *Nat. Commun.*, vol. 5, no. 1, pp. 1–6, 2014.
 - [122] M. Rafayelyan, J. Dong, Y. Tan, F. Krzakala, and S. Gigan, "Large-scale optical reservoir computing for spatiotemporal chaotic systems prediction," *Phys. Rev. X*, vol. 10, no. 4, p. 41037, 2020.
 - [123] G. Marcucci, D. Pierangeli, and C. Conti, "Theory of neuromorphic computing by waves: machine learning by rogue waves, dispersive shocks, and solitons," *Phys. Rev. Lett.*, vol. 125, no. 9, p. 93901, 2020.
 - [124] G. Barbastathis, A. Ozcan, and G. Situ, "On the use of deep learning for computational imaging," *Optica*, vol. 6, no. 8, pp. 921–943, 2019.
 - [125] N. B. Terry, T. G. Alley, and T. H. Russell, "An explanation of SRS beam cleanup in graded-index fibers and the absence of SRS beam cleanup in step-index fibers," *Opt. Express*, vol. 15, no. 26, pp. 17509–17519, 2007.
 - [126] "Abalone Dataset." <https://archive.ics.uci.edu/ml/datasets/Abalone>.
 - [127] Z. Zhang, Y. Song, and H. Qi, "Age progression/regression by conditional adversarial autoencoder," in *Proceedings of the IEEE conference on computer vision and pattern recognition*, 2017, pp. 5810–5818.
 - [128] "Free Spoken Digit Dataset." <https://github.com/Jakobovski/free-spoken-digit-dataset>.
 - [129] "COVID-19 Radiography Database." <https://www.kaggle.com/tawsifurrahman/covid19-radiography-database>.
 - [130] A. W. Snyder, "Coupled-mode theory for optical fibers," *JOSA*, vol. 62, no. 11, pp. 1267–1277, 1972.
 - [131] "Holoeye 4K Spatial light modulator." <https://holoeye.com/gaea-4k-phase-only-spatial-light-modulator/>.
 - [132] "Fujitsu Fugaku." <https://www.fujitsu.com/global/about/innovation/fugaku/>.
 - [133] S. Ortin *et al.*, "A unified framework for reservoir computing and extreme learning machines based on a single time-delayed neuron," *Sci. Rep.*, vol. 5, no. 1, pp. 1–11, 2015.
 - [134] S. Resisi, Y. Viernik, S. M. Popoff, and Y. Bromberg, "Wavefront shaping in multimode fibers by transmission matrix

engineering,” *APL Photonics*, vol. 5, no. 3, p. 36103, 2020.

- [135] T. Sperber, V. Billault, B. Dussardier, S. Gigan, and P. Sebbah, “Gain As Configurable Disorder-Adaptive Pumping for Control of Multimode Fiber Amplifiers and Lasers,” *arXiv Prepr. arXiv2008.04085*, 2020.
- [136] N. Bachelard, S. Gigan, X. Noblin, and P. Sebbah, “Adaptive pumping for spectral control of random lasers,” *Nat. Phys.*, vol. 10, no. 6, pp. 426–431, 2014.
- [137] W. Bogaerts *et al.*, “Programmable photonic circuits,” *Nature*, vol. 586, no. 7828, pp. 207–216, 2020, doi: 10.1038/s41586-020-2764-0.
- [138] J. Leuthold, C. Koos, and W. Freude, “Nonlinear silicon photonics,” *Nat. Photonics*, vol. 4, no. 8, pp. 535–544, 2010, doi: 10.1038/nphoton.2010.185.
- [139] J. Feldmann *et al.*, “Parallel convolutional processing using an integrated photonic tensor core,” *Nature*, vol. 589, no. 7840, pp. 52–58, Jan. 2021, doi: 10.1038/s41586-020-03070-1.

Curriculum Vitae

Uğur Teğın

E-mail: ugur.tegin@epfl.ch

Adress: EPFL STI IMT LAPD, BM 4109

CH-1015 Lausanne Switzerland

Education:

2018-2021 **Swiss Federal Institute of Technology in Lausanne (EPFL), Lausanne, Switzerland**

PhD Student at Doctoral Program in Photonics

Thesis title: Exploring nonlinearities in multimode optical fibers for lasers and computing

Thesis advisor: Prof. Demetri Psaltis & Prof. Christophe Moser

2016-2018 **Bilkent University, Ankara, Turkey**

MS Student at Material Science and Nanotechnology

Thesis title: Spatiotemporal nonlinear dynamics in graded-index multimode fibers

Thesis advisor: Prof. Bülend Ortaç

2011-2015 **Bilkent University, Ankara, Turkey**

BS Student at Physics

Senior project title: Dissipative Raman soliton laser

Thesis advisor: Prof. Fatih Ömer İlday

Research experience:

July 2018 – Present Research assistant

Laboratory of Optics & Laboratory of Applied Photonics Devices,

École Polytechnique Fédérale de Lausanne, Switzerland

Supervisors: Prof. Demetri Psaltis & Prof. Christophe Moser

Apr 2016 – June 2018 Research assistant

National Nanotechnology Research Center, Bilkent University, Turkey

Supervisor: Prof. Bülend Ortaç

July 2015 – Aug 2015 Intern

Time and Frequency Laboratory, University of Neuchâtel, Switzerland.
Supervisor: Prof. Thomas Südmeyer

June 2013 – July 2013 Intern

Time-Frequency and Wavelength Laboratories, UME, TUBITAK, Turkey.
Supervisor: Dr. Ramiz Hamid and Dr. Çağrı Şenel

April 2012 – Jan 2015 Research assistant

Ultrafast Optics and Lasers Laboratory, Bilkent University, Turkey.
Supervisor: Prof. F. Ömer İlday

Publications:

1. Teğın, U., Yıldırım, M., Oğuz, İ., Moser, C., & Psaltis, D. (2021). Scalable Optical Learning Operator. arXiv preprint arXiv:2012.12404. Accepted by Nature Computational Science.
2. Teğın, U., Dinç, N. U., Moser, C., & Psaltis, D. (2021). Reusability report: Predicting spatiotemporal nonlinear dynamics in multimode fibre optics with a recurrent neural network. Nature Machine Intelligence, 1-5.
3. Teğın, U., Rahmani, B., Kakkava, E., Psaltis, D., & Moser, C. (2020). Single-mode output by controlling the spatiotemporal nonlinearities in mode-locked femtosecond multimode fiber lasers. Advanced Photonics, 2(5), 056005.
4. Teğın, U., Rahmani, B., Kakkava, E., Psaltis, D., & Moser, C. (2020). All-fiber spatiotemporally mode-locked laser with multimode fiber-based filtering. Optics Express, 28(16), 23433-23438.
5. Rahmani, B., Loterie, D., Kakkava, E., Borhani, N., Teğın, U., Psaltis, D., & Moser, C. (2020). Actor neural networks for the robust control of partially measured nonlinear systems showcased for image propagation through diffuse media. Nature Machine Intelligence, 2(7), 403-410.
6. Teğın, U., Rahmani, B., Kakkava, E., Borhani, N., Moser, C., & Psaltis, D. (2020). Controlling spatiotemporal nonlinearities in multimode fibers with deep neural networks. APL Photonics, 5(3), 030804.
7. Kakkava, E., Borhani, N., Rahmani, B., Teğın, U., Moser, C., & Psaltis, D. (2020). Deep learning-based image classification through a multimode fiber in the presence of wavelength drift. Applied Sciences, 10(11), 3816.
8. Teğın, U., Kakkava, E., Rahmani, B., Psaltis, D., & Moser, C. (2019). Spatiotemporal self-similar fiber laser. Optica, 6(11), 1412-1415.

-
9. Kakkava, E., Rahmani, B., Borhani, N., Teğın, U., Loterie, D., Konstantinou, G., ... & Psaltis, D. (2019). Imaging through multimode fibers using deep learning: The effects of intensity versus holographic recording of the speckle pattern. *Optical Fiber Technology*, 52, 101985.
 10. Teğın, U., & Ortaç, B. (2018). Cascaded Raman scattering based high power octave-spanning supercontinuum generation in graded-index multimode fibers. *Scientific Reports*, 8(1), 1-7.
 11. Teğın, U., & Ortaç, B. (2018). All-fiber all-normal-dispersion femtosecond laser with a nonlinear multimodal interference-based saturable absorber. *Optics Letters*, 43(7), 1611-1614.
 12. Teğın, U., & Ortaç, B. (2017). Spatiotemporal instability of femtosecond pulses in graded-index multimode fibers. *IEEE Photonics Technology Letters*, 29(24), 2195-2198.

Conference talks:

1. *Invited talk*, "Optical computing with multimode fiber nonlinearities", IEEE Photonics Society Summer Topicals Meeting, 07/2021.
2. "Optical computing with spatiotemporal fiber nonlinearities", CLEO EU, 06/2021.
3. "Spatial self-beam cleaning in spatiotemporally mode-locked fiber lasers", CLEO EU, 06/2021.
4. "Machine learning with multimode fibers", CLEO US, 05/2021.
5. *Invited talk*, "Spectral and spatial shaping of spatiotemporal nonlinearities in multimode fibers", IEEE Photonics Society Summer Topicals Meeting, 07/2020.
6. *Highlighted talk*, "Dispersion-managed soliton multimode fiber laser", CLEO US, 05/2020.
7. "Self-similar spatiotemporally mode-locked fiber laser", Photonics West SPIE LASE, 02/2020.
8. "Learning spatiotemporal nonlinearities in graded-index multimode fibers with deep neural networks", CLEO EU, 06/2019.
9. "All-fiber all-normal-dispersion femtosecond laser with nonlinear multimodal interference-based saturable absorber", CLEO EU, 06/2019.
10. "High power supercontinuum generation in graded-index multimode fibers", CLEO EU, 06/2019

-
11. "Deep neural networks for controlling spatiotemporal nonlinearities in graded-index multimode fibers", Photorefractive Photonics and beyond, 06/2019
 12. "Generation of dissipative solitons in normal-dispersion Raman fiber laser", CLEO Pacific Rim, 08/2015.
 13. "Dissipative solitons generated from a mode-locked Raman laser", CLEO EU, 06/2015.
 14. "Seeded amplification of Stokes wave in an ultrafast fiber amplifiers", EPS-QEOD EUROPHOTON, 08/2014.

Patents and

patent applications:

Optical computing with spatiotemporal nonlinearities (2020),

Teğin U., Moser C., & Psaltis D.,

Swiss Patent Office

System and method for high beam quality pulse generation in mode-locked multimode fiber lasers (2020),

Teğin U., Moser C., & Psaltis D.,

Swiss Patent Office

Honors and awards:

Maiman Best Paper Award Finalist, CLEO US 2020

Language:

Turkish (*Native*)

English (*Fluent*)

German (*Basic*)

Japanese (*Basic*)

Computing skills:

Python, Matlab, Julia, Mathematica, FORTRAN, C++.